ROYAL INSTITUTE
OF TECHNOLOGY

Performance Quantification of Interarea Oscillation Damping Using HVDC

JOAKIM BJÖRK

Licentiate Thesis
Stockholm, Sweden 2019

KTH Royal Institute of Technology
School of Electrical Engineering and Computer Science
Division of Decision and Control Systems
SE-100 44 Stockholm
SWEDEN

TRITA-EECS-AVL-2019:23
ISBN 978-91-7873-135-0

Akademisk avhandling som med tillstånd av Kungl Tekniska högskolan framlägges till offentlig granskning för avläggande av teknologie licentiatexamen i elektro- och systemteknik fredagen den 5 april 2019 klockan 10.00 i sal E2, Lindstedtsvägen 3, E-huset, huvudbyggnaden, våningsplan 3, KTH Campus, Stockholm.

Tryck: Universitetsservice US AB

Abstract

With the transition towards renewable energy, and the deregulation of the electricity market, generation patterns and grid topology are changing. These changes increase the need for transfer capacity. One limiting factor, which sometimes leads to underutilization of the transmission grid, is interarea oscillations. These system-wide modes involve groups of generators oscillating relative to each other and are sometimes hard to control due to their scale and complexity. In this thesis we investigate how high-voltage direct current (HVDC) transmission can be used to attenuate interarea oscillations. The thesis has two main contributions.

In the first contribution we show how the stability of two asynchronous grids can be improved by modulating the active power of a single interconnecting HVDC link. One concern with modulating HVDC active power is that the interaction between interarea modes of the two grids may have a negative impact on system stability. By studying the controllability Gramian, we show that it is always possible to improve the damping in both grids as long as the frequencies of their interarea modes are not too close. For simplified models, it is explicitly shown how the controllability, and therefore the achievable damping improvements, deteriorates as the frequency difference becomes small.

The second contribution of the thesis is to show how coordinated control of two (or more) links can be used to avoid interaction between troublesome interarea modes. We investigate the performance of some multivariable control designs. In particular we look at input usage as well as robustness to measurement, communication, and actuator failures. Suitable controllers are thereby characterized.

Sammanfattning

Övergången till förnybar energi och avregleringen av elmarknaden leder till förändrade produktions-och överföringsmönster. Dessa förändringar medför behov av en ökad överföringskapacitet. En begränsande faktor, som kan leda till ett underutnyttjande av stamnätet, är interareapendlingar. Dessa systemövergripande pendlingar involverar grupper av generatorer som svänger i förhållande till varandra. Interareapendlingar är ibland svåra att styra på grund av deras skala och komplexitet. I denna avhandling undersöker vi hur förbindelser med högspänd likström, *engleska high-voltage direct current* (HVDC), kan användas för att dämpa interareapendlingar. Avhandlingen har två huvudbidrag.

I det första bidraget visar vi hur stabiliteten hos två olika synkrona nät kan förbättras genom att modulera den aktiva effekten hos en enda HVDC-länk. Ett bekymmer med aktiv effektmodulering är att växelverkan mellan interareapendlingar hos de två näten kan ha en negativ inverkan på systemets stabilitet. Genom att studera styrbarhetsgramianen visar vi att det alltid är möjligt att förbättra dämpningen i båda näten så länge som frekvenserna hos deras interareapendlingar inte ligger för nära varandra. För förenklade modeller visas det uttryckligen hur styrbarheten och därmed de möjliga dämpningsförbättringarna, försämras då frekvensskillnaden blir liten.

Avhandlingens andra bidrag visar hur koordinerad styrning av två (eller fler) länkar kan användas för att undvika växelverkan mellan besvärliga interareapendlingar. Vi undersöker prestandan hos olika typer av flervariabla regulatorer. I synnerhet undersöks styrsignalsanvändning samt robusthet mot mät-, kommunikations- och aktuatorfel. Därigenom karakteriseras lämpliga regulatortyper.

Acknowledgments

First and foremost, I would like to express my deep gratitude to my supervisor Karl Henrik Johansson for all the support, feedback, and guidance. Your enthusiasm and curiosity is a true inspiration. I would also like to thank my co-supervisor Lennart Harnefors for guidance, feedback, and the inspiration given to this interesting research topic.

I would also like to thank Robert Eriksson for the collaboration we have had so far. Your knowledge has been very valuable for my work. Special thanks also to Henrik Sandberg and Alexander Johansson for fruitful discussions and valuable feedback on this thesis. I wish to express my sincere gratitude to all my colleagues (current and former) at the Division of Decision and Control Systems—far too many to name everyone here—thank you for creating such a friendly and active working atmosphere.

The research leading to this thesis has received funding from the Swedish Research Council, the Swedish Foundation for Strategic Research, Knut and Alice Wallenberg Foundation, and the KTH PhD Program in the Digitalization of Electric Power Engineering. I am grateful for their support.

I would like to express my appreciation to my parents Ann-Christine and Johan, and to my brother Pontus for their love and unconditional support throughout my life. Thanks also to all my friends that have brought me much joy throughout my life and career. Without you I would never have gotten to where I am today. Last, but not least, I would like to thank my loving and supportive girlfriend Stina. You brighten up my every day.

Joakim Björk
Stockholm, April 2019

Contents

Chapter 1

Introduction

Since the 1950s, high-voltage direct current (HVDC) transmission has been used in applications infeasible for ac transmission such as, interconnection of asynchronous grids, long submarine cables, or the transmission of high power over extreme distances. As the technology has matured however, HVDC has become increasingly cost efficient, expanding its application area. This has led to a growth in installation making HVDC an increasingly common presence in many of today's power systems. One advantage of the dc control scheme is that the power flow can easily be controlled with high bandwidth. With appropriate control, HVDC transmission can therefore be used to improve the stability of the system in which it is installed. The utilization of controllable power electronics devices, such as HVDC, is considered a key to ensuring stable and secure operation in today's changing power system.

In this thesis, HVDC control for stabilizing interarea oscillations is considered. Of particular interest is the case when HVDC is used to interconnect asynchronous ac grids. An analysis of the fundamental control limitations imposed by the interactions of two synchronous grids over a single controlled HVDC line is performed. Following this we study how coordinated control of two or more links can be used to circumvent these limitations.

The outline of this chapter is as follows. Section 1.1 gives a motivation to why further research in power system stability is necessary. In Section 1.2 practical examples of HVDC damping control along with some simulated examples is shown. In Section 1.3 we formulate the problem that this thesis addresses. Lastly, Section 1.4 lists the remaining structure of the thesis, its contents and contributions.

1.1 Motivation

Motivated by a changing climate and an increased environmental awareness the electric power system are facing considerable changes. A gradual transition is seen from traditional centralized generation using gas, coal, and nuclear to generation from renewable sources such as solar and wind, often in small decentralized facilities.

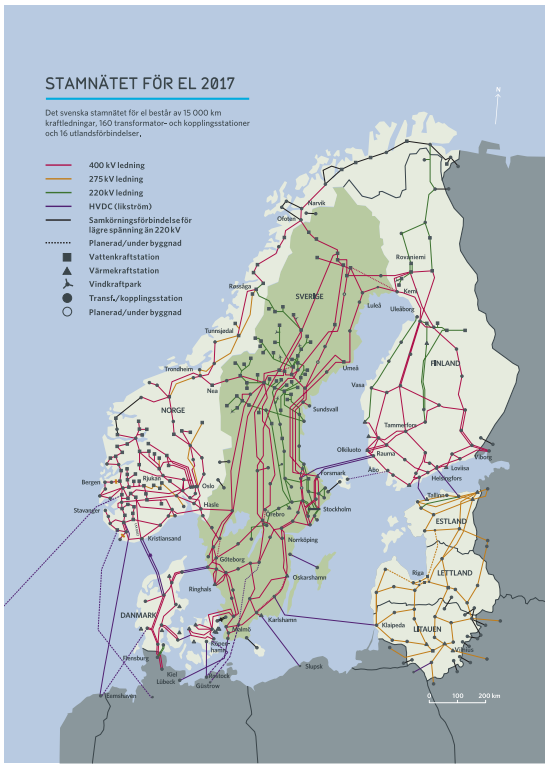

(a) The Nordic power system

(b) Nuclear power

(c) Hydro power

(d) Wind power

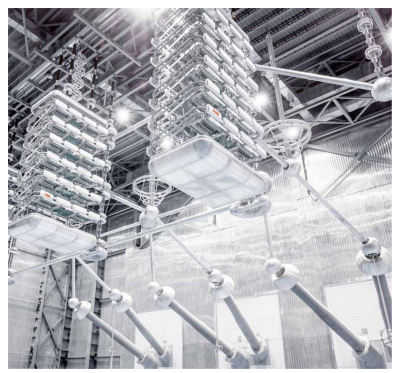

(e) HVDC

Figure 1.1: The Nordic power system (a) is an extensive power system with generation relying mainly on hydro (c) and nuclear (b). The system is experiencing great changes as synchronous production from nuclear plants are being replaced by power electronic based production such as wind power (d). At the same time HVDC transmission (e), purple lines in (a), are increasingly installed in the power system integrating the Nordic electricity market with the Continental European, the Baltic, and the UK grid. Thermal plants (including nuclear power plants) are indicated by triangles in (a). Hydro plants, mostly located in Norway and northern Sweden and Finland, are indicated by squares.
(a) Map courtesy of Svenska kraftnät. (b) Image courtesy of Vattenfall, photo: Elin Bergqvist. (c) Image courtesy of Vattenfall, photo: Hans Blomberg. (d,e) Images courtesy of ABB.

Another alteration to the power system seen during the last couple of decades is the deregulation of the electricity market. The classical vertically integrated system is split up into generator companies, transmission system operators, distribution system operators and retailers. Where system operators used to have full control of the system this is no longer the case. At the same time we see an increase in long distance transmission. An increase enabled by an increased interconnection of countries, e.g., using HVDC (seen as purple lines in Figure 1.1a). Investments, motivated by climate change, and deregulation of the power system has led to an increase in installed generation and transactions. However, due to uncertainties and long lead times, investments in the transmission system has not followed the same rate. As a result, congestion and stability problems are a growing problem in todays power systems. This thesis deals with the latter of these issues.

For power systems with long transmission corridors, such as the Nordic power system (Figure 1.1a), transmission capacity is sometimes limited by dynamical stability [1, 2]. The focus of this work is on the stability of a dynamical phenomena known as interarea oscillations. The dynamics of these involve electromechanical interactions between large generator groups in different regions (or areas) of the system oscillating against each other. Sufficient stabilizing control often require coordinated tuning of multiple components. The strength and controllability of HVDC makes it suitable for stabilization of these system wide oscillatory modes.

With an increasingly intermittent power production and a deregulated electricity market, we see an increase in long distance transmission and international trade. Because of this, operation in highly stressed condition is becoming more common. Instability in the form of interarea oscillations have therefore become an even greater concern than in the past [3]. At the same time, the number of controllable devices in the grid is growing rapidly. The control of power electronic based devices such as HVDC links and flexible ac transmission systems (FACTS) is recognized as a key factor in maintaining a secure and dependable power system. As the interaction between multiple controllable devices and dynamical components are far from trivial, optimization-based control methods are receiving a lot of research focus [4–9]. Although necessary for practical application, resorting to numerical optimization-based methods sacrifices physical intuition of the system. To aid the increasingly complex control problem, this work focus on understanding the limitations imposed by network structure and the interaction between dynamical components and controllers.

The potential of HVDC control for damping of interarea modes have been studied for decades. A prime example of this is the damping of the 0.3 Hz north-south interarea mode in the western North American power system in the 1970s. During heavy loading, the transmission system frequently experienced growing power fluctuations as seen in Figure 1.2. These oscillatory tendencies constrained the amount of surplus hydro power that could be transmitted to the southwest. Active power modulation of the Pacific HVDC Intertie (PDCI) was implemented to counteract these power oscillations, thereby increasing the transfer capacity of the parallel ac transmission system [10–12].

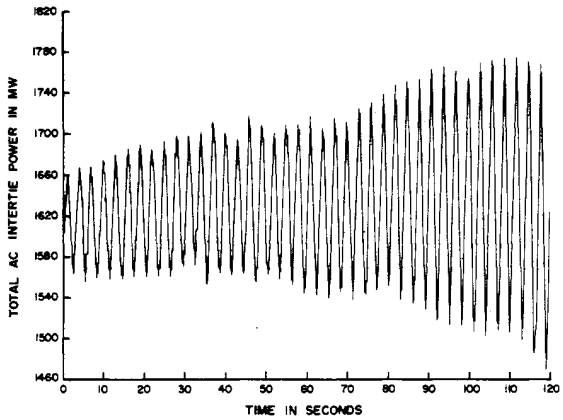

Figure 1.2: Negatively damped power oscillations in the western North American power system recorded August 2, 1974 [10]. © 1976 IEEE

To maintain a high power quality with stable and secure supply, it is important that new devices aid in services previously provided by synchronous machines. The strength and controllability of HVDC makes it a suitable technology to aid in controlling the system wide interarea modes. However, most existing HVDC installations today are not utilized for this purpose. For instance, the PDCI damping control scheme never left prototype status. This is because the feedback signal, based on local ac power flow, had a transfer-function zero which limited the controller gain and caused oscillations at higher frequencies to worsen [12]. Poor damping of the north-south interarea mode has continued to be an issue in the western North American power system where it was one of the mayor factors in the Blackout of August 10, 1996 [13, 14].

The purpose this thesis is to improve the theoretical understanding of the problem and increase confidence in new control solutions. Thus increasing the chances for auxiliary HVDC control schemes, such as damping control, to be adopted by transmission system operators.

As seen in Figure 1.3, troublesome interarea modes may exist in exist in both of the interconnected power systems. The focus of this work is to understand the limitations imposed by system interaction when controlling HVDC interconnections between two asynchronous ac grids.

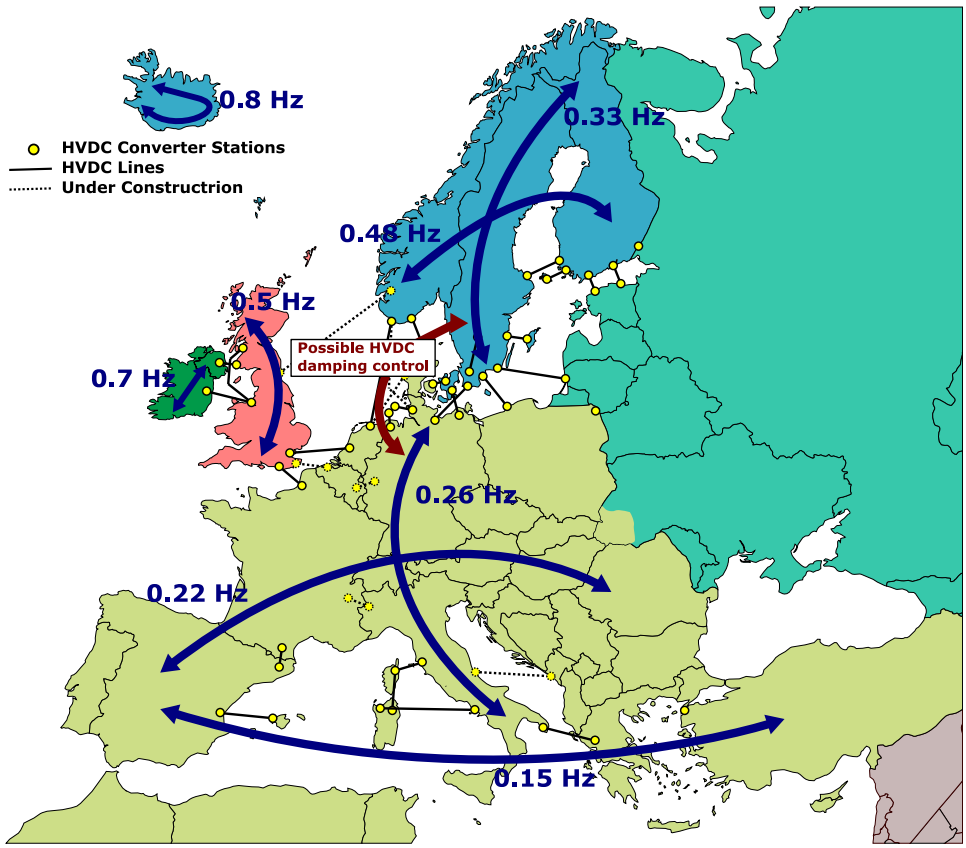

Figure 1.3: Interarea modes in Europe. Credit Florian Dörfler.

1.2 HVDC Power Oscillation Damping

HVDC is often used to strengthen transmission corridors in power systems. Since the HVDC installations often bridge long distances, they have a strong influence on dominant power system modes. Through active power injection, damping of interarea modes, or so called, power oscillation damping (POD) can be improved by reducing local rotor speed deviations between the HVDC terminals. In the following, results from the operating experience of the PDCI damping control [11] is presented as a practical example of how HVDC modulation can improve POD. Following this, simulations on a simplified model are done to further illustrate the concept. The setup is conceptually the same as the practical example where the PDCI is embedded in the western North American power system in parallel with the ac transmission (Figure 1.4a). The example show that dc active power modulation is effective at improving POD in a parallel setting. When using HVDC active power

modulation between asynchronous system however, damping control may excite poorly damped modes in the assisting system.

Control of active power injections to provide damping of interarea modes is a hot research topic today due the increasing amount of power electronics, battery storages, and renewable production. However, most research does not consider the interaction that may occur with the power source, which in this case would be the other ac grid. In the last example it is shown how the interaction between interarea modes of two HVDC interconnected ac system may limit POD performance.

Example 1.1 (Modulation of the PDCI) The western North American power system spans the continent from the western Pacific coast to the foot of the Rocky Mountains in the east, from Canada in the north and partly into Mexico in the south as seen in Figure 1.4a. The system has a history of poorly damped interarea modes (Figure 1.2) limiting the amount of surplus hydro power that could be transmitted

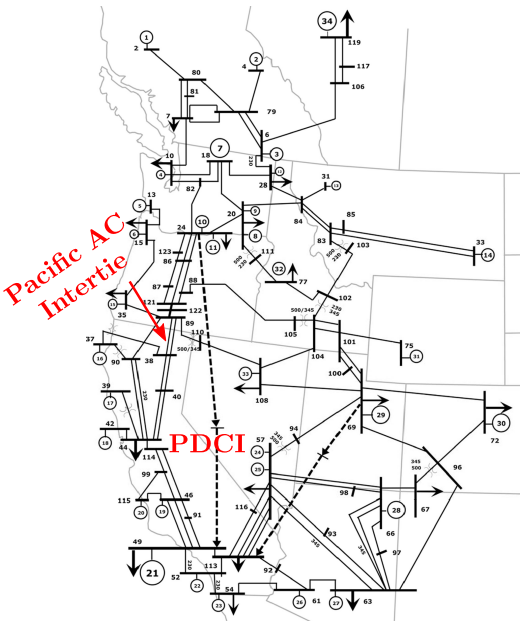

(a) One-line diagram of the western North America power system [12]. © 2013 IEEE

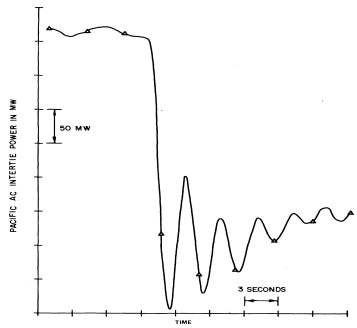

(b) System response to relaying 600 MW generating unit without dc modulation. © 1978 IEEE

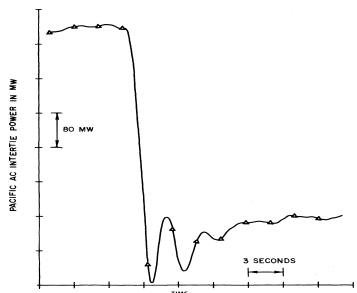

(c) System response to a 1100 MW load rejection test with dc modulation. © 1978 IEEE

Figure 1.4: (Example 1.1) Power oscillations in the PACI following a system disturbance (b and c). Initial ac intertie loading is approximately 2,500 MW in both scenarios [11].

to the southwest. To increase the transfer capacity, the Bonneville Power Administrator began studies which led to the development of a control system to modulate the PDCI running parallel to the ac transmission system in north-south direction as seen in Figure 1.4a. In Figures 1.4b and 1.4c large disturbances effect on the parallel Pacific AC Intertie is shown. In Figure 1.4b a 600 MW generating unit is relayed off line. Without the dc modulation in service, the disturbance result in a poorly damped interarea mode visible as oscillating ac power flow. In Figure 1.4c the response to a 1,100 MW load rejection is shown. With dc modulation activated the improved POD is clearly visible. The POD improvement, allowed for a rating increase from 2,100 MW to 2,500 MW [10, 11].

Example 1.2 (Four-Machine Two-Area Test System) This example simulates HVDC damping control in a parallel configuration similar to previous example. An HVDC interconnection is installed in a four-machine two-area power system as shown in Figure1.5. The test system was developed in [15] for the study of electromechanical modes. The implemented model, fitted with some modifications, is available in the Simulink library [16]. All four generators are equipped with a steam turbine governor and automatic voltage regulators. To illustrate damping improvement, power system stabilizers (PSS) have been deactivated making the interarea oscillation between Area 1 and 2 unstable. The HVDC link is a 400 MVA, 200 kV point-to-point voltage source converter (VSC) HVDC. The VSC-HVDC is represented using an averaged model and a Π-circuit transmission line with typical converter and line data according to [17].

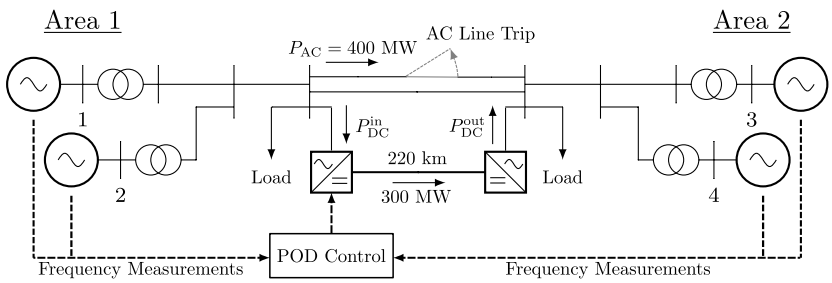

Figure 1.5: A simple four-machine two-area test system with a VSC-HVDC link in parallel with the ac interconnection.

The system is initiated with a 400 MW ac and 300 MW dc power flow from Area 1 to Area 2 as seen in Figure 1.5. The interarea oscillations are triggered by tripping one of the ac transmission lines interconnecting the two areas. Without HVDC damping control the system is unstable and the two areas eventually separate as seen in Figure 1.6.

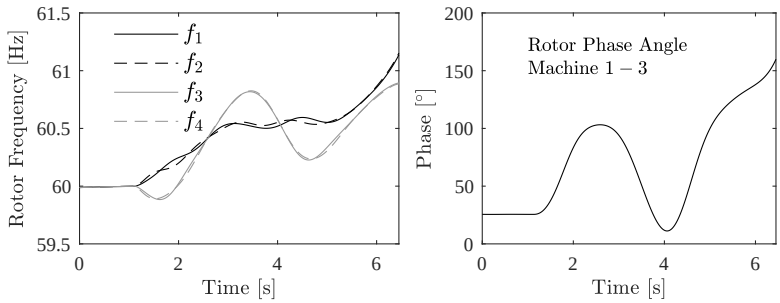

Figure 1.6: Rotor frequencies and phase angel difference between machine 1 and 3 of the four-machine two-area test system following ac transmission line trip as seen in Figure 1.5. Without HVDC POD control the system is unstable.

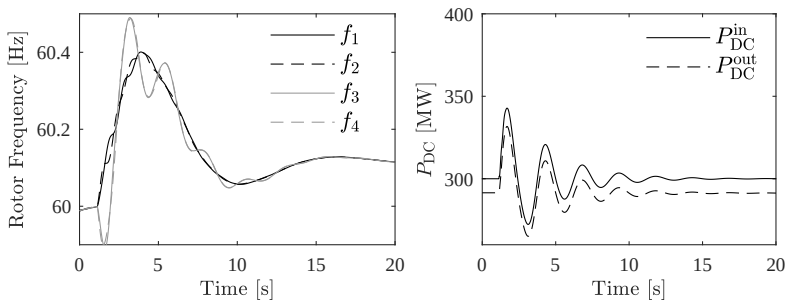

Figure 1.7: Rotor frequencies and dc active power of the four-machine two-area test system following ac transmission line trip as seen in Figure 1.5. DC active power is control using (1.1) with a proportional gain, $K_{\mathrm{DC}} = 200\,\mathrm{MW/Hz}$.

To stabilize the system we use feedback control of the VSC-HVDC link. Controllability analysis shows, as seen in previous studies [6, 18, 19], that active power-modulation is effective at improving POD in the proposed system. For illustrative purposes we here assume an ideal scenario were rotor frequency measurements from all four machines are available to represent the inter area mode as

$$\Delta f = \frac{f_1 + f_2}{2} - \frac{f_3 + f_4}{2}.$$

HVDC active power is modulated using proportional control

$$P_{\mathrm{DC}}^{\mathrm{in}} = K_{\mathrm{DC}} \Delta f \tag{1.1}$$

With feedback gain $K_{\mathrm{DC}} = 200\,\mathrm{MW/Hz}$ we see in Figure 1.7 that POD is improved.

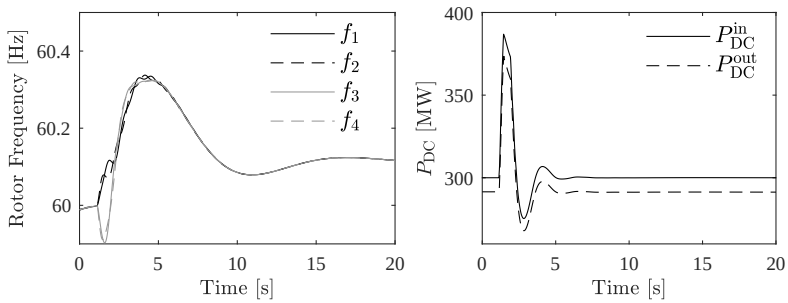

Figure 1.8: Machine speeds and dc active power of the four-machine two-area test system following ac transmission line trip as seen in Figure 1.5. DC active power is control using (1.1) with a proportional gain, $K_{\mathrm{DC}} = 600\,\mathrm{MW/Hz}$. Compared to Figure 1.7 we see that a faster disturbance attenuation is achieved at the cost of a higher dc active power.

With higher feedback gain, even stronger damping is achievable. By increasing the feedback gain, K_{DC} to 600 MW/Hz, we see (in Figure 1.8) that damping of the interarea modes is improved at the cost of active power usage.

Example 1.3 (HVDC-Interconnected Asynchronous AC Networks) The system in Example 1.2 is modified. Two two-area test systems is interconnected using a VSC-HVDC as seen in Figure 1.9. The system are structurally identical. An interarea oscillation is triggered by a load disturbance in the top ac network. The disturbance is attenuated with the help of an assisting ac network (the bottom network) through HVDC POD control. The system will be uncontrollable if the eigenvalues corresponding to the considered interarea modes coincide [20]. To avoid this, the machine inertias of the assisting network have been scaled to increase the interarea mode by 20 %. In Figure 1.10a it is seen that the system can be stabilized by HVDC active power modulation. As in Example 1.2 the two systems

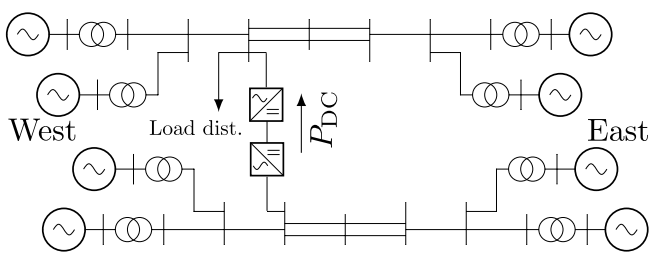

Figure 1.9: A simple four-machine two-area test system with a VSC-HVDC link an parallel with ac interconnection.

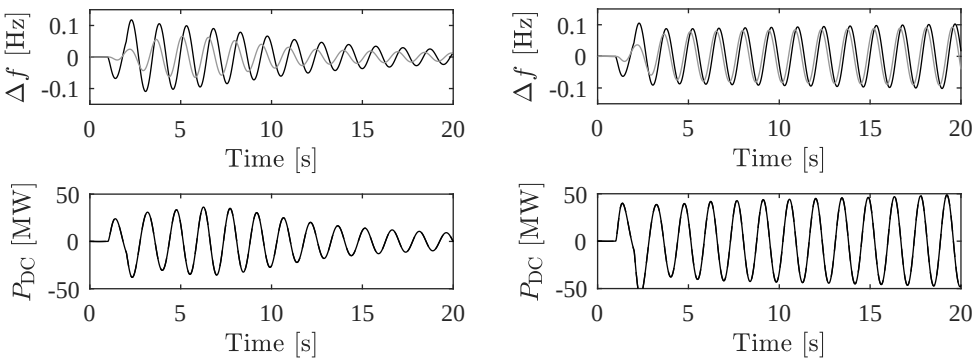

(a) 400 MW/Hz (b) 800 MW/Hz

Figure 1.10: Frequency difference between western and eastern areas in the two HVDC interconnected ac networks following a 200 MW load disturbance at time 1–2 s. With a higher feedback gain in (b) we see that the control fails to stabilize the system.

are inherently unstable. Following a load disturbance[1] the top system (as shown in to Figure 1.9) the ensuing interarea oscillation is attenuated and both systems are stabilized by HVDC active power modulation. In Chapter 3 it is shown how POD control moves the eigenvalues of the interconnected networks towards each other. With increasing feedback gain the controllability of the interarea modes are reduced until the controller can no longer stabilize the system as seen in Figure 1.10b.

1.3 Problem Formulation

In this thesis we consider HVDC active power modulation for damping of oscillatory interarea modes. Interarea modes are a complex dynamic phenomena involving groups of machines in one end of the system swinging against machines in other parts of the system. Swinging of the machine results in ac power oscillating in the interconnecting tie-lines, interarea oscillations are therefore also known as power oscillations. By modulating the HVDC link between two networks, active power is injected from one network to the other causing the interarea modes of the two networks to interact. To simplify the analysis, a model abstraction is performed. We let the dominant interarea mode be represented by a two-machine model. Consider the Nordic 32-bus Cigré test system [21] shown in Figure 1.11a. The mode

[1] Controllability is greatly affected by the eigenvalues of the two interconnected networks. The tripping of a transmission line (as was done in Example 1.2) will greatly affect the eigenvalues corresponding to the interarea mode in the affected system. To simplify this example we instead consider a load disturbance which will have less effect on system eigenvalues.

of interest is chosen as the poorly damped interarea mode between the north and south area. The dynamics of this mode is represented using a two-machine model where each machine represent a lumped sum of the machines in each respective area. In Figure 1.11b a similar simplification is shown on the four-machine two-area test system. Aggregating multiple machines in one area into a single machine is a common simplifying approach used in analysis. The benefit of the simplified representation is that the interarea mode is easier to analyze. However, interesting dynamics might be lost in the simplification. For instance the two-machine model contains no information about the local modes occurring between the machines within the two areas in Figure 1.11b.

The dynamics of a power system can be described by a set of differential algebraic equations

$$\dot{x} = f(x, \theta, u)$$
$$0 = g(x, \theta, u)$$

where vectors x and θ contains system state and algebraic variables respectively. The vector u contains control inputs, which in this case is the HVDC active power input. For the purpose of analyzing the stability of electromechanical modes a linearized small-signal model is enough. The small-signal model considers small deviations $[\Delta x, \Delta\theta, \Delta u]$ around an operating point $[x, \theta, u] = [x_0, \theta_0, u_0]$. Deviations are assumed sufficiently small so that (if $\frac{\partial g}{\partial \theta}$ is invertible) the linearized model

$$\Delta\dot{x} = \left(\frac{\partial f}{\partial x} - \frac{\partial f}{\partial \theta}\left(\frac{\partial g}{\partial \theta}\right)^{-1}\frac{\partial g}{\partial x}\right)\Delta x + \left(\frac{\partial f}{\partial u} - \frac{\partial f}{\partial \theta}\left(\frac{\partial g}{\partial \theta}\right)^{-1}\frac{\partial g}{\partial u}\right)\Delta u \qquad (1.2)$$

accurately describes system dynamics [15]. The linearized model (1.2) gives a linear time-invariant state-space representation

$$\Delta\dot{x} = A\Delta x + B\Delta x$$
$$\Delta y = C\Delta x$$

where A and B are system state and input matrices given by the partial derivatives in (1.2), Δy is some output with corresponding output matrix C.

The objective of this thesis is to describe the underlying system properties that limit achievable performance in terms of power oscillation damping (POD). Using HVDC links interconnecting two asynchronous power systems as shown in Figure 1.12. Using a feedback controller

$$\Delta u = K\Delta y$$

the goal is to stabilize the interarea modes by increasing the POD in both of the HVDC-interconnected ac networks. The considered controller K can be either static (memory-less) or dynamic. Due to interactions between the two interconnected ac networks, achievable damping performance may be limited. Another important factor is the electrical position of the HVDC terminals involved in POD control.

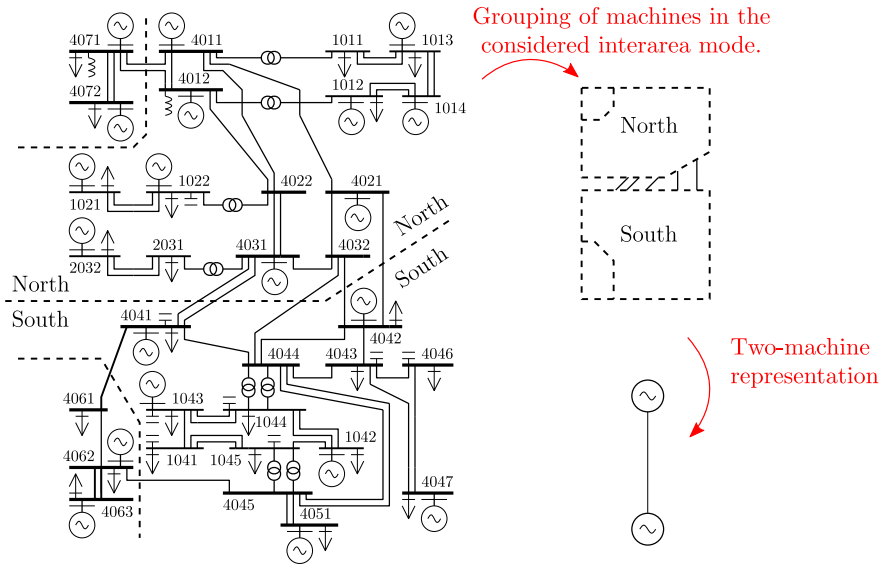

(a) Nordic 32-bus test system.

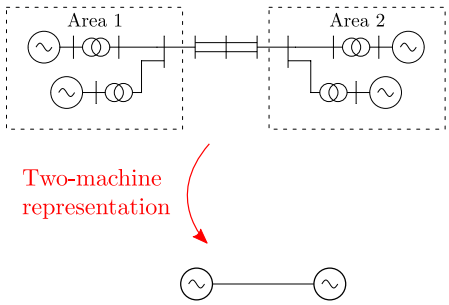

(b) Four-machine two-area system.

Figure 1.11: Model abstraction of dominating interarea mode in two power system models. The simplified two-machine representation lose information about tie-line flows and local modes within the two areas and between other machine groupings.

In the simplified model representation shown in Figure 1.12 line impedance, thus electrical position, is visualized as length of the transmission line.

For the analysis, we let each ac network be represented by a two-machine model to characterize the dominant interarea mode in each network. Using this simplified model, valuable insight can be obtained about the fundamental control limitations of the HVDC-interconnected system.

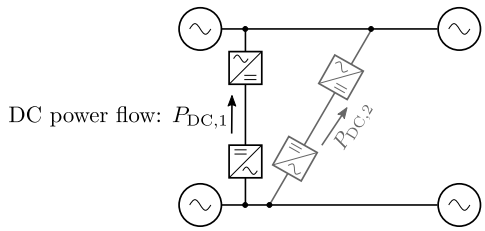

Figure 1.12: Two asynchronous power systems interconnected by two HVDC transmission lines.

1.4 Outline and Contributions

The outline of the remainder of this thesis and its main contributions can by summarized as:

Chapter 2: Background

In this chapter we give some short overview of power system stability and control. A brief introduction to HVDC technology and a literature study of HVDC control for power oscillation damping is given.

Chapter 3: Fundamental Performance Limitations

As a first contribution of this thesis, we study the fundamental performance limitations in utilizing HVDC for POD when interconnecting two asynchronous power systems with a single HVDC line. Using a simplified model, an analytical study is performed. The goal is to investigate the limitations for POD using active power modulation of a single HVDC link with no energy storage. It is shown how the proximity of interarea modes puts a fundamental limit to achievable performance. The findings are evaluated on a small model with two HVDC-interconnected two-machine networks as well as on an interconnection of two Nordic 32-bus Cigré test systems [21].

Chapter 3 is based on the publication

- J. Björk, K. H. Johansson, and L. Harnefors, "Fundamental performance limitations in utilizing HVDC to damp interarea modes," *IEEE Transactions on Power Systems*, vol. 34, no. 2, pp. 1095–1104, Mar. 2019

Chapter 4: Coordinated HVDC Control

In the second contribution of this thesis, we build on the problem formulation of Chapter 3 by adding additional HVDC links. By coordinated control of multiple HVDC links, the limitations studied in Chapter 3 can be circumvented. In addition

it is shown that decoupled control of the concern modes is achievable using a proportional controller. The best coordinated control design is investigated by looking on input usage and stability following dc link failure.

Chapter 4 is based on the publication

- J. Björk, K. H. Johansson, L. Harnefors, and R. Eriksson, "Analysis of coordinated HVDC control for power oscillation damping," in *IEEE eGrid*, Charleston, SC, Nov. 2018, pp. 1–6, best paper award recieved for e-poster presentation

Chapter 5: Conclusions and Future Work

Finally, in this chapter we conclude the thesis, summarizing and discussing the result. We also outline some future and ongoing work, indicating some possible directions in which this work can be extended.

Chapter 2

Background

A power system can typically be divided in three parts: generation, transmission, and distribution as shown in Figure 2.1. The function of an electric power system is to generate electricity from naturally available forms and to transmit it to customers connected to the distribution grid. The advantage of the electrical form of energy is that it can be transported and controlled with high efficiency and reliability. However, unlike other types of energy, electricity cannot be conveniently stored in sufficient quantities. A major challenge of the power system is therefore to meet the continually changing load demands. Today this is becoming increasingly challenging as conventional synchronous generation such as coal, gas, and nuclear, are being replaced by inverter based generation from intermittent sources such as wind and solar.

Energy should be supplied at minimum cost and optimal efficiency. Losses in the transmission system is minimized by controlling tie-line flows. This can be done by allocating generation, connecting and disconnecting transmission lines, controlling HVDC power transmission etc. Tie-line flows can also be controlled by adjusting

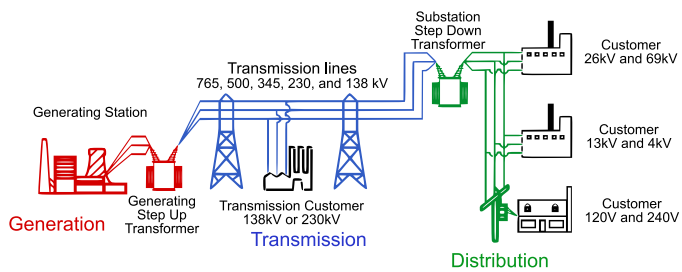

Figure 2.1: Typical power system. Image courtesy of United States Department of Energy[1].

[1]United States Department of Energy, SVG version by User:J JMesserly [CC BY 3.0 (`https://creativecommons.org/licenses/by/3.0`) or Public domain], via Wikimedia Commons. Changes made to label positions and the text of customer labels.

system voltages using tap-changing transformers, generator excitation, or power electronic devices controlling reactive power such as HVDC and FACTS.

Controls should also contribute to maintaining an adequate power quality with respect to: constancy of frequency, constancy of voltage, and level of reliability. The aforementioned control methods all have a big impact on the dynamic performance of the power system [15]. The focus of this thesis is on reliability in terms of dynamical stability of the power system.

The remainder of this chapter is organized as follows. In Sections 2.1 and 2.2 an introduction to classifications of power system stability and interarea oscillations is given. A Conventional method of improving power system stability using generator excitation control is shown. In Section 2.3 an introduction to HVDC technologies are given. In Section 2.4 the function, control and modeling of HVDC is briefly explained. In Section 2.5 we discuss how HVDC can be used to provide frequency support between asynchronous grids. Finally Section 2.6 presents a literature survey of resent work on HVDC damping control methods.

2.1 Power System Stability

The modern power system is mankind's largest an most complex machine. It is the backbone of the modern economy and our daily lives. Many crucial parts of our society rely on a high quality, constant and dependable supply of electricity. Thus, stability of the power system, like the stability of any dynamic system, is crucial. The stability of a power system can be defined as follows. [3]

"Power system stability is the ability of an electric power system, for a given initial operating condition, to regain a state of operating equilibrium after being subjected to a physical disturbance, with most system variables bounded so that practically the entire system remains intact."

This definition is wider than that of a single stable operating point. However, in this work we will mostly consider stability in the sense of stable operating points. The definition of system security is closely related to stability but may be distinguished from stability in terms of the resulting consequences. [15]

"Security of a power system refers to the degree of risk in its ability to survive imminent disturbances (contingencies) without interruption of customer service. It relates to robustness of the system to imminent disturbances and, hence, depends on the system operating condition as well as the contingent probability of disturbances."

Power system security is usually guaranteed in the sense on $N-1$ stability. The $N-1$ criterion states that the power system must be operated at all times such that after an unplanned loss of an important generator or transmission line it will remain in a secure state.

The ability of ac networks to reliably transfer power is referred to as transfer capacity (or capability). The net transfer capacity may be limited by various factors:

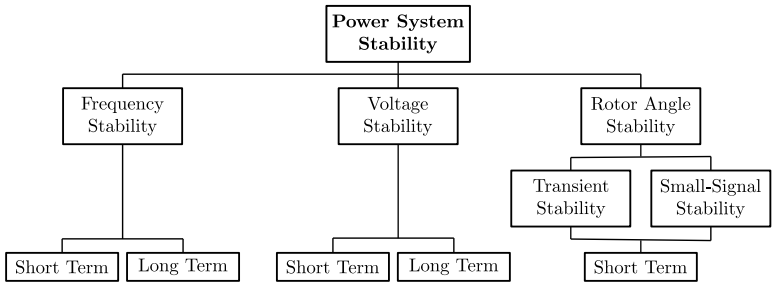

Figure 2.2: Classification of dynamical power system stability [3].

- *Thermal limits* are given by the maximum current a conductor can tolerate before risking overheating. Higher than rated currents may be allowed for some period of time.
- *Voltage limits* are given by the acceptable voltage levels at each point in the system. Voltage drop due to reactive power flows in an inductive power system set a limit to the amount of power that can be transfered while still maintaining acceptable voltages.
- *Stability limits* are determined by system stability following small and large disturbances of different types. The system must be operated so that the system is able to survive disturbances through the transient and following dynamical time period ranging from millisecond to minutes. In complex, heavily loaded transmission systems, stability limitations often set the transfer capacity limit.

Dynamical power system stability is usually separated into the three categories shown in Figure 2.2, namely, frequency stability, voltage stability, and rotor angle stability. The following is an introduction to these definitions.

Frequency Stability

System frequency is maintained by balancing generation with load. A simple representation of overall frequency dynamics is given by the aggregate swing equation

$$M\dot{\omega} = P_{\mathrm{m}}(\omega) - P_{\mathrm{load}}(\omega) \tag{2.1}$$

where ω is the global average frequency, M is the combined inertia of all the synchronous machines. Following a load disturbance, change in P_{load}, the system frequency will start to deviate from its initial state. Frequency stability is concerned with the ability to maintain and restore system frequency by balancing load demands with that of mechanical input power P_{m}. In this thesis, frequency control measures will be discussed in terms of primary and secondary reserves. Primary

reserves, also referred to as frequency containment reserves, have the purpose to stabilize the system frequency following a load disturbance, and to maintain the frequency within allowed boundaries [24]. As seen in (2.1) an increase in system load will lead to a decreasing system frequency. To counteract this, generated power need to be increased to stabilize the system frequency.

A secondary control, also referred to as frequency restoration reserves, act replace the activated primary reserves and possibly to restore system frequency to its nominal value. This can be done either by manually controlling the mechanical powers or adding a integrating feedback. There are also other slower mechanics with the purpose of restoring secondary reserves and to redistribute production to increase system safety and minimize losses [24].

The concept of primary and secondary control is explained in the following example.

Example 2.1 (Frequency Stability) The total controllable input power in the power system (2.1) is represented by a single hydro turbine with governor as shown in Figure 2.3. Primary control is realized as a proportional droop controller in charge of maintaining system frequency close to its nominal value ω_n in case of load changes. Due to the proportional primary control, the system will stabilize at a new steady state frequency. To restore system frequency, a secondary control with integral action is implemented. Figure 2.4 shows the system response to a load step.

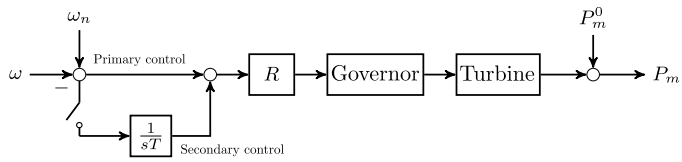

Figure 2.3: Governor controlling a hydro turbine representing the aggregate controllable reserves of the power system.

Initial frequency stability concerns are that of the rate of change of frequency (RoCoF) and the maximum frequency deviation (the nadir) shown in Figure 2.4. RoCoF is proportional to the occurring load/generation disturbance and inversely proportional to the system inertia. The nadir is proportional to the size of the disturbance and the inverse system inertia as well as the available primary reserves and the speed of which these can be activated. Exceeding allowed RoCoF and nadir limits may lead to tripping of system components and a cascading failure [25].

A problem with renewable inverter based power production is that these do not contribute to the overall system inertia. This increases the need for fast acting primary reserves. At the same time, renewable energy such as wind and solar are an intermittent energy source leading to further power fluctuations in the system. To allow for a high penetration of renewable energy it is important that such sources participate in the primary reserves.

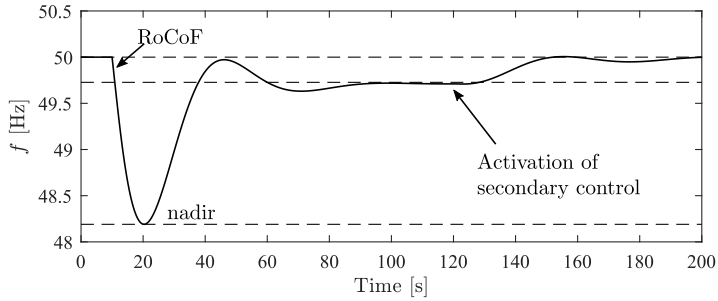

Figure 2.4: System response to a load step. Primary and secondary reserves is provided by hydro turbine with governor control shown in Figure 2.3. As can be seen, the primary control manage to maintain a steady state frequency deviation of 0.25 Hz. As the secondary controller is activated 120 s into the simulation, frequency is restored to its nominal value.

A complement to reserves within the interconnected system is to utilize HVDC to share primary reserves between asynchronous grids. One such example is the sharing of Nordic hydro power to the European system [26].

Historically, when power systems where small scale with operators supplying small geographical regions or cities, frequency stability was a big problem since variability of load and production caused a severe impact on system power balance. The solution to this problem was the introduction of the large scale power system with long distance transmission interconnecting not only cities and regions but also countries. As power systems grow larger, the impact of single variations become smaller. The dynamics of the system become slower, making it easier to maintain a steady frequency. As power system grow in complexity however, new issues are introduced.

Voltage Stability

Voltage stability refers to the power systems ability to maintain acceptable voltages at all buses following a system disturbance. The driving force for instability is usually loads attempting to restore their power using control mechanisms such as tap-changers. Failure to meet load demands lead to a progressive drop in voltage. Voltage instability is usually a local phenomena, although its consequences can be wide spread [3, 15, 27].

On way to improve the voltage stability is through load reduction or reactive power support. Reactive power support from the transmission system is limited by the voltage drop that occurs when active and reactive power flow in the inductive transmission lines. Since voltage stability is a local phenomena, an efficient solution is to provide local reactive power support. Reactive power injection using flexible ac transmission system (FACTS) devices such as, static var compensator (SVCs)

or a static synchronous compensator (STATCOM) have proven to be efficient at improving voltage stability of power systems [3, 15, 27].

Rotor Angle Stability

Rotor angle stability refers to the power systems ability to maintain synchronism following disturbances. Instability may occur in the form immediate separation or increasing angular swings between synchronous generators. This may result from the disconnection of one or a group of generators from the rest of the system.

Transient Stability

Transient stability is concerned with the power systems ability to maintain synchronism following large disturbances such as the outage of a transmission line or a generating unit. Transient stability is influenced by the non-linear power-angle relationship resulting in aperiodic instability. Following a fault, the speed of generators start to deviate due changing operating condition, resulting in a deviation of rotor angle. A lack of synchronizing torque may cause a system separation resulting in what is called *first-swing instability*. Installing fast-acting exciters with automatic voltage regulation (AVR) can greatly improve the synchronizing torque of the generator as seen in Example 2.2. The need for AVR increases as transmission distances and transmitted power increases. In large power systems however, this phenomena may be more complex and and instability may not always occur with the first swing. Transient stability depends on both the initial operating point as well as the location of the failure [15, 28].

As seen in Example 2.2 the act of AVR often tend to reduce the damping torque of the system, risking the system to become oscillatory unstable. Thus, AVR often has to be accompanied by stabilizing controllers such as power system stabilizers (PSS), stabilizing FACTS control, or HVDC control as seen in Examples 1.2 and 1.3.

Small-Signal Stability

Small-signal (or small-disturbance) stability considers the power systems response to small changes around an operating point. The disturbances are considered to be sufficiently small so that a linearized model is suitable for analysis.

Instability can occur in two forms [3]:

- aperiodic increase in rotor angle due to lack of sufficient synchronizing torque;
- rotor oscillation of increasing amplitude due to lack of damping torque.

In today's power systems, small-signal stability is mainly an issue of damping of oscillations.

Oscillations are due to natural modes in the power system and cannot be completely eliminated. One of the primary source of negative damping torque are the AVR control of synchronous generators as illustrated in the following example.

Example 2.2 (Rotor Angle Stability) Example 13.2 from [15] is implemented in Simulink Simscape Electrical. A single machine, representing the aggregation of four synchronous machines, feeds 0.9 p.u. active power into an infinite bus as shown in Figure 2.5. At time $t = 1\,\text{s}$ a three phase ground fault occurs at one of the transmission lines. The fault is cleared by disconnecting the affected line at both ends. Two scenarios with a fault clearing time of 0.07 s and 0.10 s respectively are run to illustrate the destabilizing effect of AVR control and the need for PSS.

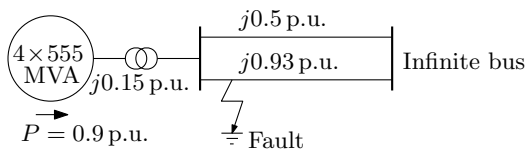

Figure 2.5: Single machine network with reactances in p.u. on 2,220 MVA base.

- *Constant field voltage:* With no excitation control, the generator survives with 0.07 s fault clearing time and remains stable under the new configuration as seen in Figure 2.7. However, for a 0.10 s fault clearing time, the generator is first-swing unstable due to a lack of synchronizing torque as seen in Figure 2.6.

- *AVR without PSS:* A fast-acting exciter and AVR is used to increase the synchronizing torque making the generator first-swing stable for a 0.10 s fault clearing time as seen in Figure 2.6. However, the degradation of damping torque cause the generator to loose synchronism during the second swing.

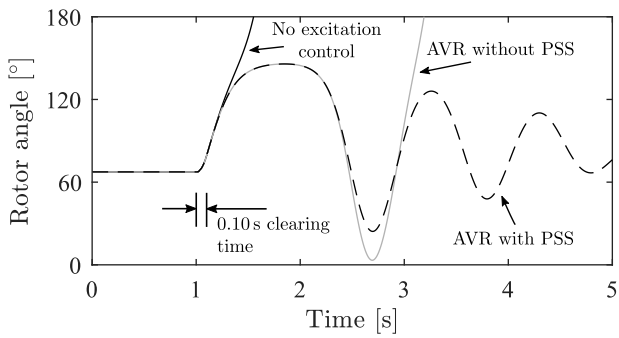

Figure 2.6: Simulation result showing rotor angle response with fault cleared in 0.10 s.

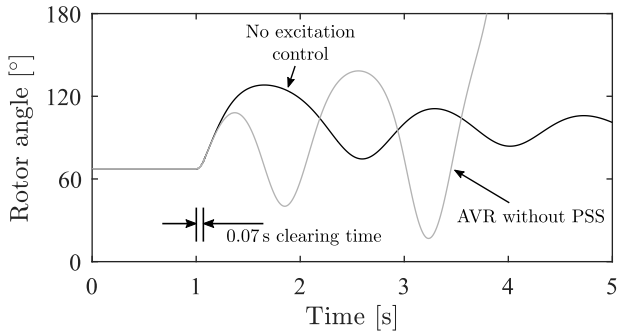

Figure 2.7: Simulation result showing rotor angle response with fault cleared in 0.07 s.

In addition, the introduction of AVR makes the previously stable system unstable due to a lack of damping torque as seen inf Figure 2.7. Because of this, the system can no longer survive even with 0.07 s fault clearing time. To increase the allowed fault clearing time without sacrificing stability, damping torque can be increased by adding a PSS to the generators excitation control.

- *AVR with PSS:* The addition of a PSS contribute to the damping torque ensuring transient as well as small-signal stability of the system as seen in Figure 2.6.

Electromechanical dynamics are those associated with the oscillation of synchronous machine such as the one seen in previous example. These comes in two types [29]:

- *Local modes* are between one or a groups of units at a generating station against the rest of the system. The time frame of such oscillations is typically around 1–3 Hz.
- *Interarea modes* are associated with groups of generators in one area of the system swinging against machines in other areas of the power system. Inter-area oscillations are caused by weak transmission line and large line loadings.

Other modes relevant for the analysis of synchronous machine involve [29]:

- *Control modes* associated with control equipment. Poorly tuned exciters, HVDC converters, or STATCOM devises are the usual cause of instability of these modes which typically are close to 3 Hz.
- *Torsional modes*, which are faster modes, typically in the range of 10–50 Hz, associated with the turbine-generator shaft rotations system. Instability are generally caused by interaction with control equipment.

2.2 Stability of Interarea Modes

The main focus of this work is on the stability of interarea modes. These modes involve complex interactions between multiple machines. As more power is being transfered over long distances, stability of these mode may deteriorate. For long networks, such as the Nordic transmission system, or the Western Interconnection of North America, this often pose a limiting factor for ac transmission capacity [12, 30]. In the 10 August 1996 power blackout in the western North America, growing power oscillation due to insufficient damping was found to be a decisive factor [13]. As interconnection increases with an increase in international trade due to deregulated electricity markets, these problems are likely to become worse in the future. At the same time, the shift towards renewable energy sources such as wind and solar impose further changes to the grid. The intermittent nature of these sources increases the demand for international interconnection to help balance load and production and maintaining system frequency [26].

In addition to excitation control of synchronous machines, interarea modes are also heavily affected by load dynamics. With an increasing amount of power electronics in loads and production facilities, constant power load characteristics are becoming increasingly dominant in the system. This further reduces the inherent damping in the system.

Conventional control methods such as PSS based on local measurements may prove insufficient to damp interarea modes due to actuator limitations and limited observability of the considered modes. Some methods to improve performance is coordinated PSS control using either local or wide-area measurements from phase measurement units (PMUs). Control of power electronic devises such as FACTS, and HVDC have also proved a useful complement for improving the damping of interarea modes [2, 30]. In what follows are two incidents reports where poor damping of interarea modes was reported in the Continental European (CE) power system. In both occasions the investigations concluded that new methods are needed for ensuring stability in the changing power system.

On the 1^{th} of December 2016 an unexpected tripping of a line interconnecting the French power system to the Spanish system occurred. The event triggered triggered an East-Center-West interarea oscillation in the CE system. In the event the Iberian Peninsula and the Turkish system oscillated in anti-phase with the central part of the CE system. The oscillations were damped in three minutes after mitigation actions were taken by the Spanish transmission system operator. Analysis of the incidents showed that reactive power modulation of the HVDC line between France and Spain contributed in damping of the oscillation. Investigations into optimizing active and reactive HVDC modulation for damping of interarea oscillations was investigated following the event [31].

On the 3^{rd} December 2017 a north-south interarea oscillations was registered in the CE system. The oscillation began at 1.09 a.m. and reached its maximum at around 1.15 a.m. when actions were taken. The causes of the incident was identified as

- low consumption (low load contribution to damping)
- high voltage phase angle differences in the Italian power system
- unavailability of some generators caused non-standard power flows
- huge imports to the southern part of the CE system

leading to a gradual decrease of general damping. A conclusion drawn from the event was that changes and integrations of new technologies in the European electricity calls for additional innovative damping countermeasures. New devises and methods must be developed to minimize serious consequences of interarea oscillations [32].

In this thesis we investigate the usage of active power modulation in HVDC lines for damping of interarea modes. The critical operation requirement on the grid and the complexity of interarea oscillations motivates the need for an increased system understanding. In this thesis we therefore strive to understand the fundamental nature and limitations of oscillation damping control using simplified dynamical models.

2.3 HVDC Technologies

HVDC is one of the most promising technologies for strengthening the future grid due to its high efficiency and controllability. In this section we give a brief overview of different HVDC converter technologies.

Line Commutated Converters

The first commercial application of HVDC was to connect the island of Gotland to the mainland of Sweden in 1954. The installation provided 20 MW through an 96 km underwater cable using mercury-arc valves developed by Uno Lamm and his team at ASEA (now ABB). Since the 1970s thyristor valve converters have replaced the less durable and cost efficient mercury-arc technology. The first commercial thyristor based HVDC installation was the Eel River scheme, installed in 1972 between the Canadian provinces of New Brunswick and Quebec [15, 33]. Thyristors are capable of conducting the current in one direction only and will do so when switched on by the gate signal and will continue to do so as long as the anode is positive with respect to the cathode. This technology is called line commutated converter (LCC) HVDC. As this control method relies on the grid voltage to stop conducting, switching has to occur at grid frequency.

LCC-HVDC could in theory be operated as either current source or voltage source. In practice however, current source converters prevail as the commutation process is less sensitive to ac voltage disturbances [34]. The converters absorb reactive power, as the current is always lagging behind the voltage. The reactive power requirement is in the order of 60 % of power rating and depends on power flow level.

Figure 2.8: The first commercial HVDC link manufactured by ASEA (now ABB) connected the Island of Gotland to the mainland of Sweden in 1954.

Due to this, LCC-HVDC installations, in weak systems, need to be accompanied by reactive power compensation such as STATCOM or SVC [15, 33–36].

The shortcomings of LCC-HVDC, such as reactive power consumption and ac grid requirements, spurred the development of force commutated converters.

Force Commutated Converters

Since the 1990s insulated-gate bipolar transistors (IGBTs) have been implemented in voltage source converter (VSC) HVDC applications. This new semiconductor technology allows for commutation (switching) operations regardless of ac line voltage and allows for control of reactive power and installation in weak ac systems [35]. Early adoptions of the VSC technology uses an pulse-width modulation (PWM) at high frequency to approximate the ac waveform. However due to switching losses this method is unfavorable to the traditional thyristor based LCC converters for high power installation. The modular multilevel converter (MMC) has improved the efficiency of VSC-HVDC since switching can be done at grid frequency. This greatly reduces power losses making VSC competitive with the traditional LCC technology.

Some of the advantages of force commutated voltage source converters over line commutated current source converters are [33]:

- the commutation does not fail when ac voltage is decreased or distorted;
- pulse-width modulation reduce low-order harmonics, greatly reducing requirements of harmonic filters;
- independent control of active and reactive power at each terminal;
- no local reactive power supply required;

- allows for connection to weak ac grids such as off-shore wind power plants.

Multi-Terminal HVDC

Most HVDC installation today are point-to-point installation. However, a lot of research focus today is towards multi-terminal HVDC (MTDC) system where converters are interconnected with two or more additional converters. The most promising technology for this is MMC-HVDC as it offers lower switching losses, better fault performance, and higher controllability [4, 36–40]. There are currently two MTDC projects in operation using the MMC technology: the Nan'ao Multi-terminal VSC-HVDC project [41], and the Zhoushan dc power grid project [42].

Advantages of HVDC

HVDC transmission has some advantages over ac transmission [15, 33, 43].

- Transmission losses for HVDC are lower than ac making it an attractive solution for bulk energy transmission. However, the terminal cost and losses are higher for HVDC. Typically, the break-even distance for overhead lines is around 500–800 km as shown in Figure 2.9.
- AC transmission via long underground or submarine cable is impractical due to the high capacitance. These restrictions do not apply to dc. The typical break-even distance is reduced to around 50 km for submarine cables.
- DC constitutes an asynchronous connection allows for the interconnection of asynchronous power systems, possibly with different frequencies, as seen in Figure 2.16.
- The asynchronous connection also allows for an increased transmission capacity without increasing the short-circuit power at the connection points. This means that it will not be necessary to change ac circuit breakers.
- The active power flow in the HVDC links can easily be controlled at high speed. With appropriate control the HVDC link can be used to improve ac-system stability.

HVDC is typically installed where ac is infeasible such as between asynchronous grids or for long submarine cables. However, together with other properties such as controllability there are many important factors to consider in the overall cost analysis for HVDC installations.

The property that is of most interest in this work is the controllability of HVDC active power flows. The possibility to almost instantaneously control power injections in between different ends of the power system may prove a vital role of ensuring stable and secure operations in the future grid.

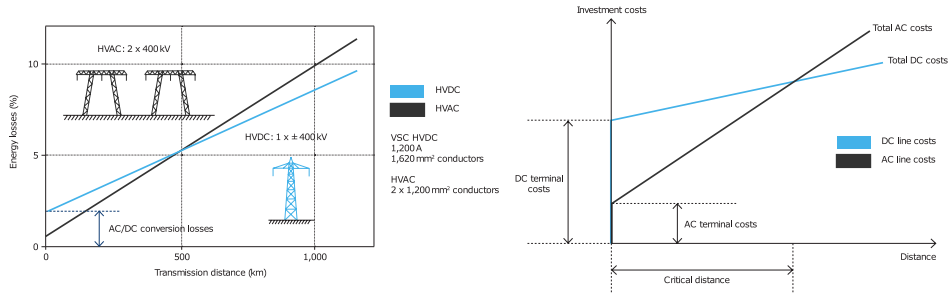

(a) Losses of HVDC compared to HVAC.

(b) Cost of HVDC compared to HVAC.

Figure 2.9: Losses and cost for HVDC converter stations and transmission compared to similarly rated high-voltage alternating current (HVAC) overhead lines [43]. Images courtesy of ABB.

2.4 HVDC Dynamics and Control

The converters of HVDC acts as a bridge between ac and dc side. By the switching of valves, dc is turned in to ac and vice versa. In this section we show the principle of how this is done for LCC- and VSC-HVDC.

LCC-HVDC

The workings of a LCC is easiest understood by studying the 6-pulse thyristor bridge shown in Figure 2.10a. A nearly constant dc current[2], $i_{\mathrm{DC}} = I_{\mathrm{DC}}$, is ensured by a large dc inductance L_{DC}. Thus the converter is operated as a current source. The thyristor are switched between phases to crate an ac waveform. The resulting square wave seen in Figure 2.10b is rich in harmonics that need to be filtered out. Typically two 6-pulse bridges are stacked to create a 12-pulse bridge is used to produce an output with less harmonics.

Thyristors are capable of conducting the current in one direction only and will do so when switched on by the gate signal and will continue to do so as long as the anode is positive with respect to the cathode. By controlling the firing angle, α, turn-on is controlled. The dc output voltage is given by [44]

$$v_{\mathrm{DC}} = \frac{3\sqrt{2}E}{\pi}\cos\alpha - R_c I_{\mathrm{DC}} \tag{2.2}$$

where E is the line-to-line root-mean-squared ac voltage. Due to commutation inductance, L_c, the ac current cannot change instantly. This result in a commutation delay, μ, where the current commutates between phases. The resistance R_c in (2.2) models the resulting voltage drop due to commutation losses.

[2]Lower case letters are used to emphasize that we are considering time varying parameters.

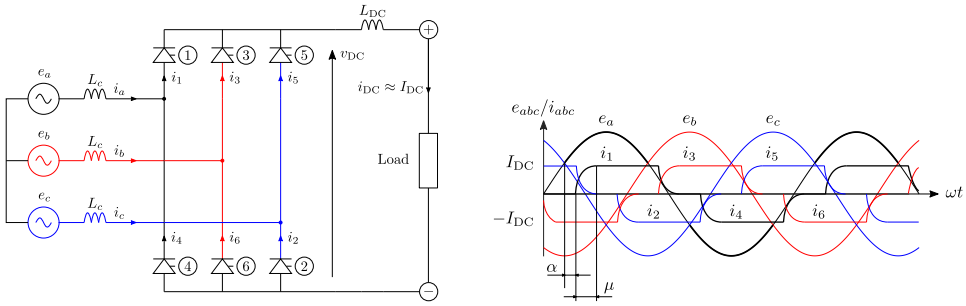

(a) 6-pulse thyristor bridge.

(b) AC line-to-neutral voltage and current at converter terminal under rectifier operation.

Figure 2.10: Simplified single-line diagram of a three-phase LCC 6-pulse bridge.

From (2.2) we see that if $\alpha < 90°$ the converter works as a rectifier. With higher firing angle the dc voltage goes negative and the converters becomes an inverter. The firing angle in rectifying operation can be reduced to around 5°. This is to ensure sufficiently high positive voltage over the valves and to account for small asymmetries in ac line voltages. Inverter operation is a bit more complicated. A commutation margin $\gamma = \pi - \alpha - \mu$ of 15° (18°) is typically needed for 50 Hz (60 Hz) systems. This is because the thyristor valves require a certain time interval with negative voltage to recover its blocking capability. If the thyristor fails to turn off, commutation failure occurs where the dc side becomes short circuited [33, 34, 44].

As the current is always lagging behind the voltage, the LCC consumes reactive power proportional to active power at both rectifier and inverter terminals.

VSC-HVDC

The VSC synthesizes an ac voltage from a dc voltage source maintained by a large dc capacitance. Thus the converter is inherently a voltage source. Since the IGBTs used in VSC can be turned off regardless of ac line voltage, any desirable ac voltage can be imposed at the converter terminal. Provided that operation is within the voltage/current capability of the converter and a power source/sink is able to maintain the dc voltage v_{DC} at desired level V_{DC}.

The basic operation of a VSC can be understood by studying the single-phase two-level converter shown in Figure 2.11a. The ac terminal is switched between positive and negative dc voltage. Pulse-width modulation is implemented by comparing a triangular wave to a sinusoidal carrier wave of desired shape. By switching between voltage levels a sinusoidal is emulated as seen in Figure 2.11a. Only filtering of higher switching harmonics is required. This significantly reduces ac filter sizes compared to LCC-HVDC. By adding a connection at neutral dc voltage (Figure 2.11b) a three level converter which gives a better ac approximation. [44]

Switching frequency is typically 1–2 kHz. For high power applications, switch-

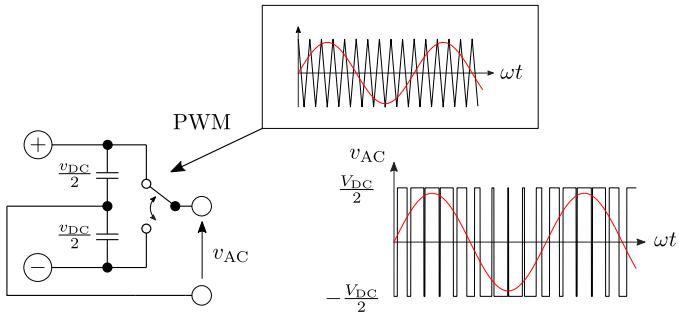

(a) Single-phase two-level converter.

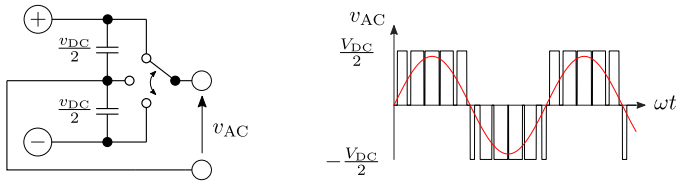

(b) Single-phase three-level converter.

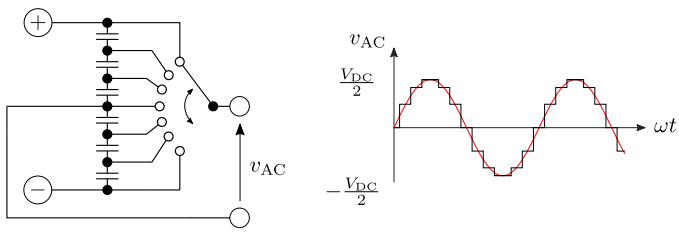

(c) Single-phase MMC.

Figure 2.11: Operating principle of VSC-HVDC.

ing losses limits the achievable switching frequency and the usefulnesses for VSC. Thyristors are also a more mature technology than IGBTs allowing for higher voltage ratings. Therefore LCC is still the dominating technology when it comes to high power applications. With the development of MMCs the efficiency of VSC is approaching LCC however.

The MMC synthesize a high-quality sinusoidal voltage waveform by incrementally switching between a high number of series-connected voltage sources as shown in Figure 2.11c[3]. Switching frequency can be reduced to 100–150 Hz. Thus, switching losses are reduced. Typically converter station losses are 1.5–2 % for two- and -three level VSC, 0.8–1 % for MMC, and 0.6–0.8 % for LCC [36].

[3]In practice PWM occurs between adjacent voltage levels similar to the three-level VSC.

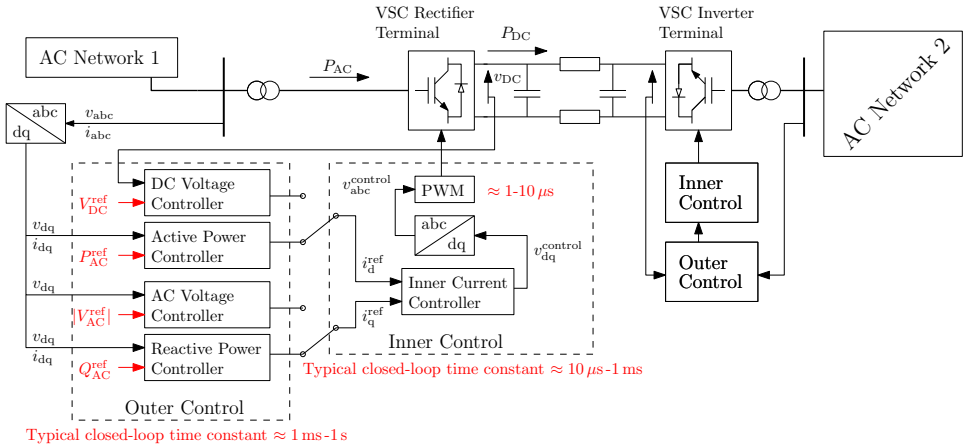

Figure 2.12: Topology of VSC-HVDC with control system in a dq reference frame.

Modeling HVDC Dynamics

Traditional LCC-HVDC still dominates applications for bulk power transmission as the mature thyristor technology offers lowest losses. However, with the development of MMC, VSC are approaching the efficiency of LCC and is thus seeing an increased market share. The independent control of active and reactive power and ability to connect to weak ac systems makes VSC-HVDC an important technology in a power system where synchronous generation is being phased out [4, 44]. Because of this, this work mainly focuses on VSC-HVDC but the results can also be extended to LCC.

As previously mentioned, one of the benefits of power electronic based components such ac HVDC are the speed of which these can be controlled. Bandwidths in tens of Hz can easily be obtained for the HVDC current control. Even for devises rated hundreds of MW [45]. When analyzing the electromechanical dynamics involved in interarea oscillations (0.1–1 Hz) most HVDC dynamics can be neglected. For the analysis of interarea modes, HVDC links are therefore often modeled as constant power loads [20, 46]. This simplification is justified in by the following example.

Simulating a VSC-HVDC Link

Figure 2.12 shows a typical control scheme of a VSC-HVDC link. Controls are implemented in a *dq* framework where the *d* current controls either the dc voltage or the activate power and the *q* current controls either the ac voltage or the reactive power. For stable operation, one of the terminals need to control the dc voltage. In the following example it is shown how the dc link can be controlled using a *master-slave* architecture where rectifier controls active power while the inverter controls

dc voltage.

Example 2.3 (Master-Slave Control) Consider a VSC-HVDC link interconnecting two ac terminals as seen in Figure 2.13. In this example we use a average value model[4] of the converters. This means that switching dynamics are not modeled. This is typically the level of detailed needed to study ac and dc dynamics for the high level control system design [44]. Modeling the dc transmission as a Π-circuit, the dynamics of interest for the dc system are

- voltage dynamics at the dc terminals

$$C\frac{dv_{\mathrm{DC}}^{\mathrm{rec}}}{dt} = i_{\mathrm{rec}} - i_{\mathrm{DC}}$$
$$C\frac{dv_{\mathrm{DC}}^{\mathrm{inv}}}{dt} = i_{\mathrm{DC}} - i_{\mathrm{inv}}$$

  where C includes capacitance of converter sub-modules, dc cable, and dc capacitors;

- dc current dynamics

$$L\frac{di_{\mathrm{DC}}}{dt} = v_{\mathrm{DC}}^{\mathrm{rec}} - v_{\mathrm{DC}}^{\mathrm{inv}} - Ri_{\mathrm{DC}}$$

  where L and R are the inductance and resistance of the dc cable.

Neglecting converter losses, active power at the dc and ac terminals are given by

$$P_{\mathrm{AC}}^{\mathrm{rec}} = i_{\mathrm{rec}}v_{\mathrm{DC}}^{\mathrm{rec}}$$
$$P_{\mathrm{AC}}^{\mathrm{inv}} = i_{\mathrm{inv}}v_{\mathrm{DC}}^{\mathrm{inv}}.$$

Power flow and dc voltage can be controlled using a master-slave architecture as shown in Figure 2.13.

Here, active power is controlled using a PI-controller at the rectifier with sufficient bandwidth to follow a reference step with 0.2 s rise time and a 0.5 Hz sinusoid as shown in Figure 2.14. Similarly the dc voltage is controlled at the inverter terminal as seen in Figure 2.15. The dc voltage is controlled so that the inverter active power tracks the power injected at the rectifier terminal. For the time frame of interest, the only considerable difference between the two power flows are the small resistive losses in the converters and the cable. For the analysis of interarea modes, which falls in the 0.1-1 Hz range, modeling the converters as constant power loads can therefore be considered a reasonable approximation.

The rating of the dc cable and the tuning of the PI-controllers are shown in Tables 2.1 and 2.2 respectively.

[4]Simulations are implemented in Simulink. VSCs are based on a static synchronous compensator (STATCOM) phasor type model available in the Simulink library.

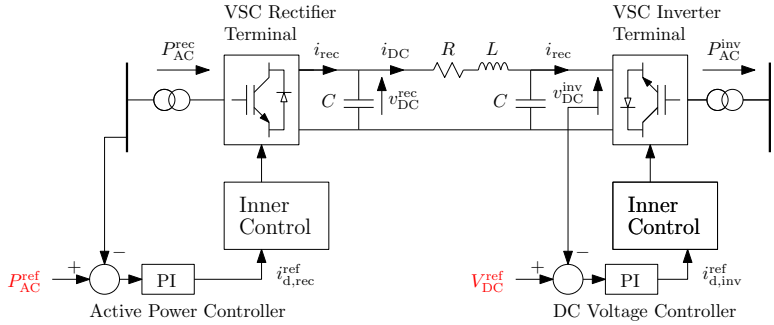

Figure 2.13: Master-slave control of a VSC-HVDC link.

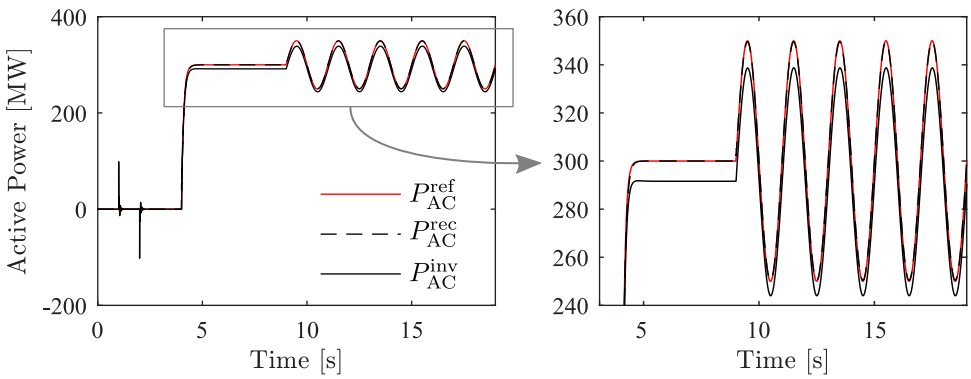

Figure 2.14: Active power reference tracked by using a PI-controller at the rectifier terminal. Initial disturbances are due to a change in dc voltage reference according to Figure 2.15.

The dc controller needs to maintain the voltage within acceptable levels. Thus sufficient closed-loop bandwidth is needed. For connection to weak ac systems, this can be a problem as non-minimum phase behavior of the ac transmission system limit the achievable bandwidth. With larger dc capacitors however, the voltage control can be relaxed. Taking advantage of dc energy storage, the rectifier and inverter power flows could also be decoupled to some extent. For instance, auxiliary control such as a virtual synchronous generator control [47] could be added at the inverter terminal to provide power oscillation damping to the ac network connected on the inverter side. In this thesis however, we do not consider dc energy storage. Instead the focus is on the interaction between the HVDC-interconnected ac networks.

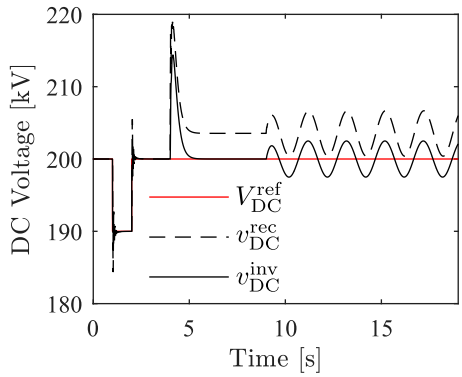

Figure 2.15: DC voltage reference tracked by using a PI-controller at the inverter terminal. Initially, small voltage reference steps are done. This is followed by active power changes according to Figure 2.14.

Table 2.1: Converter and line data obtained from [17]. DC capacitance includes lines, converter sub-modules and dc capacitors.

Voltage rating	200 kV
Power rating	400 MVA
Length	220 km
R	0.011 Ω/km
L	2.615 mH/km
C	175 µF

Table 2.2: PI-controller settings. Both controllers prevent wind up by limiting integral action at ±1 p.u.

Active Power Controller	
Proportional gain	10 p.u.
Integral gain	100 p.u.
DC Voltage Controller	
Proportional gain	5 p.u.
Integral gain	25 p.u.

2.5 Frequency Support Using HVDC

Contrary to traditional ac transmission, HVDC enables the interconnection of asynchronous grids. Active power modulation, if made fast enough, allows for the networks to share primary control reserves, reducing the maximum frequency fall (the nadir) and the steady-state frequency deviation following disturbances in load or production [20, 40, 48–51]. This facilitates a higher penetration of renewable power production, where inertia and primary are important concerns.

HVDC transmission allows production resources to be shared between asynchronous power systems such as the CE system and the Nordic system as seen in Figure 2.16. HVDC-interconnections are becoming increasingly important to balance the increased share of intermittent renewable production [3, 26, 54]. An increased interconnection of the energy market is crucial in the transition towards a renewable and sustainable power sector. Since this expansion may lead to an increased system complexity, and an even higher demand on transmission capacity, the stability of interarea modes is likely to become a greater concern in the future.

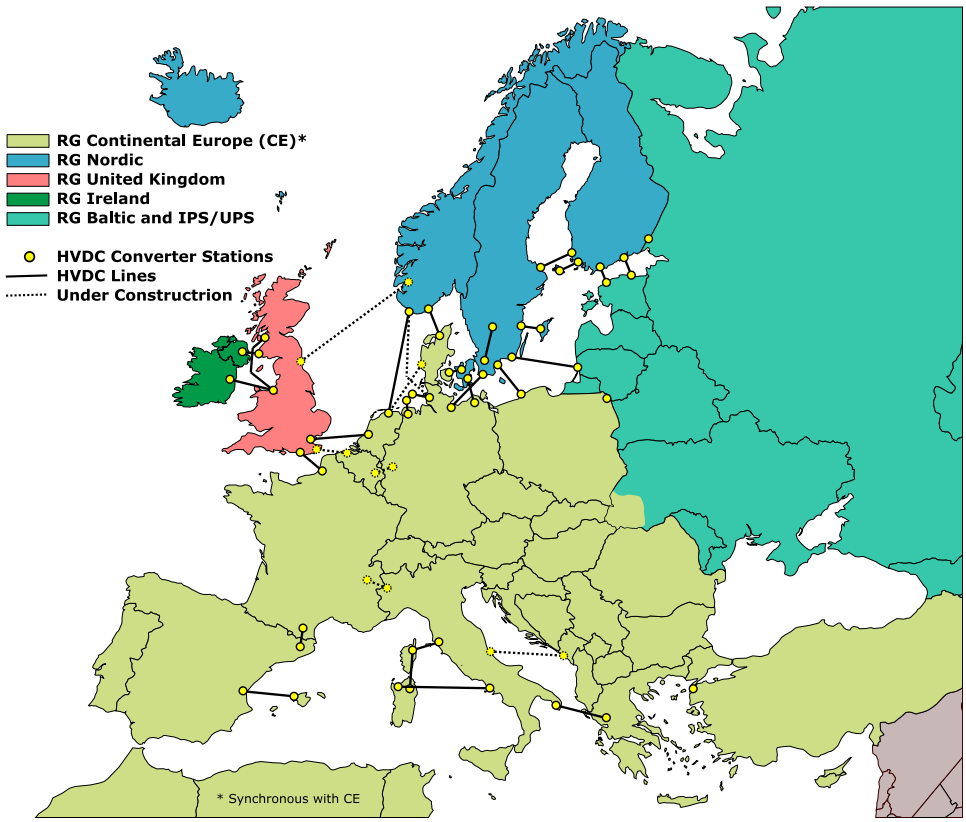

Figure 2.16: Map of the synchronous ac interconnections in Europe with an overview of HVDC interconnections in operation and under construction [52]. The high amount of hydro production with reservoirs in the Nordic region provides a relatively cheap flexibility both on a day-ahead and hourly operation. With increasing interconnection to the Continental European, the UK, and the Baltic regions, the competition for this low cost flexibility provided by hydro will increase. This may lead to greater changes in power flows and a more stressed system [53].

Utilization of hydro power in the Nordic system, as flexible production reserves, is an interesting business opportunity but will also play an important role in reducing the fossil dependency in the CE grid. However, usage of HVDC to share primary reserves may put further stress on system transmission [26, 53]. Due to its geographic extensiveness, the Nordic system is already limited by stability of inter-area oscillations [1, 30]. Utilization of HVDC for frequency support would increase the need for POD, which could be provided by said HVDC interconnections.

2.6 Power Oscillation Damping Using HVDC

Since HVDC transmissions often bridge long distances, they have a strong influence on dominant power system modes. Controlling the active power, local rotor speed deviations at the HVDC terminals can be reduced, thereby improving power oscillation damping (POD). In the 1970s active power modulation of the Pacific HVDC Intertie (PDCI) was implemented to improve POD in the western North American power system, thereby increasing the transfer capacity of the parallel Pacific AC Intertie [10–12]. Control of the LCC-HVDC link is implemented by modulating dc active power of the rectifier using ac power flow measurements of the parallel ac lines. In LCC-HVDC, active and reactive control are heavily coupled. With coordinated control of rectifier firing angle and inverter extinction angle however, some degree of decoupling can be achieved. In [55], Grund *et al.* develop such a method by modulating rectifier dc current and the inverter dc voltage. The implemented controller is a linear quadratic Gaussian (LQG) regulator designed to minimize the system measurement requirements. The incorporation of reactive power control is shown to give an increased POD performance. With VSC technology, possible POD benefits are even higher as active power (typically at the rectifier terminal) and reactive power at both dc terminals can be controlled independently within the capability curve of the VSC system [56].

The addition of reactive power control may not always improve POD performance as it depends on ac network topology and placement of the dc terminals. In [46], Smed and Andersson show that the effect of active and reactive modulation are complementary. Active modulation being effective at dc terminals adjacent to generators participating in the interarea mode, while reactive modulation has highest controllability in the mass-weighted electrical midpoint between the two areas. An example of this is seen in [6] where Pipelzadeh *et al.* design a coordinated control scheme for VSC-HVDC POD control. The control design was implemented in the four-machine two-area test system [15] (shown in Example 1.2). It is found that although reactive power control at both terminals is implemented, the control design favor active power control. It is found that controllability from reactive power control improved as the ac power flow increased which agrees with the findings of [46].

Wide Area Measurement Systems

The availability of wide area information from phase measurement units (PMU) offer new possibilities for damping of interarea oscillations in large systems. Recent development in wide area measurement systems (WAMS) allows for greater observability and coordination of multiple control units [57]. Trudnowski *et al.* [12] evaluate PDCI damping control in the western North American power system. The conclusion is that the relative feedback between the two dc terminals of the PDCI gives better robustness properties than local frequency or ac power flow measurements. In [58], Preece *et al.* evaluate the robustness and performance of WAMS based POD control using a probabilistic methodology. The centralized and decen-

tralized control of two VSC-HVDC links is designed using a modal linear quadratic Gaussian (MLQG) method targeting weakly damped modes. The method allows for individual modes to be targeted and synthesize a controller based on the available measurement [18, 59]. In [60], Hadjikypris *et al.* use the same MLQG design to coordinately control two FACTS devises and a VSC-HVDC link for POD. Juanjuan *et al.* [61] design a WAMS-based POD control for multiple HVDC lines in the China Southern Power Grid, known as the largest ac/dc paralleling transmission system in the world. The transfer capacity of the system is often limited by weakly damped interarea modes. The control of HVDC proved advantageous over conventional methods where achievable POD is limited by the adjustable capacity of generators under PSS control and FACTS supplementary damping control. In [9], Azad *et al.* design a decentralized supplementary control of multiple LCC-HVDC links in a meshed ac network. The controller is designed using sparsity-promoting optimal control to prevent interactions among the HVDC links and to enhance damping of interarea modes. The sparsity-promoting optimal control simultaneously identify the optimal control structure and optimize the closed-loop performance [8, 62].

Multi-Terminal HVDC

With more controllable devices in the system, optimal placements of new installation need to be considered in order to maximize controllability of poorly damped modes. In [20], Harnefors *et al.* investigate POD from active power modulation of three- and four-terminal HVDC network embedded in a single ac network and when interconnecting two asynchronous grids. The study show that the pairing of two terminals in general provides the best result. Using an analytical approach, recommendations for terminal pairings are developed. In [63], Fuchs and Morari present a linear matrix inequality based method for optimal placement of multiple point-to-point HVDC lines within a meshed ac network. Coordinated control of multi-terminal HVDC (MTDC) offers potentially more controllability and flexibility than point-to-point HVDC. With few active systems in operation today, MTDC is receiving a lot of research focus [4, 37–39]. In [37], Eriksson develops a decentralized control method to improve POD through an MTDC system connected to an ac grid. Active-power is controlled at the dc terminal with strongest controllability of the oscillatory mode. Voltage droop controllers, at the remaining dc terminals, are then tuned to maximize POD without the need of communication between the terminals. In [38] a cascaded control strategy is developed to provide virtual inertia to an ac network by utilizing energy stored in dc capacitors and the inertia of the wind turbines. It is shown that utilizing power stored in dc capacitors before exerting power from wind turbine inertia could help increase wind power production by allowing for a better power point tracking. However, it is shown that HVDC capacitor value had little effect on overall inertia support compared to the kinetic energy stored in the wind turbines. In [39] the interaction between an ac network and an MTDC system integrated with wind power is analyzed. Normally, electromechanical dynamics are much slower than the converter control of the MTDC.

However, it is shown that the dc voltage control, under certain conditions, may cause strong dynamical interactions between the MTDC and ac systems, degrading POD performance.

HVDC Interconnecting Asynchronous Power Systems

Most existing literature focus on the dc and inverter dynamics, or paralleling ac/dc transmission systems. To complement existing research, this work instead focuses on the electromechanical interactions between HVDC-interconnected asynchronous grids. One concern that arises when utilizing HVDC active power control for POD is that interarea modes of the assisting network may be excited [20]. Since poorly damped interarea modes usually fall in the same frequency ranges [15], control methods should avoid unnecessary excitation of weekly damped modes. In a case study of a future North Sea grid, Ndreko *et al.* [64] describe how HVDC active power modulation can be utilized to improve a poorly damped oscillatory mode of 0.5 Hz in the UK grid. This, however, results in a disturbance propagating through the North Sea HVDC network, exciting a poorly damped interarea mode of 0.5 Hz in the Nordic grid at the other end. The interaction between the interconnected ac systems can be mitigated by utilizing the wind power resources in the North Sea grid [64] or in the dc capacitors [47, 65]. The latter method may however increase the cost of the dc installation since larger capacitors may be needed. In addition such control methods require careful tuning since the introduced dc dynamics may interact with the ac system and degrade POD performance [39]. In [66], Van Hertem *et al.* show that coordinated control of two links that interconnect two asynchronous ac system can be used to improve power POD in one of the networks. The poorly damped system is modeled as a two-machine system with a dc terminal close to each machine. Controlling the terminals in anti-phase, the setup resembles a long HVDC link interconnecting the two areas HVDC link in anti-phase, the link resembles a long HVDC link interconnecting the two areas. Oscillation damping is improved by injecting power between the two areas, using the asynchronous ac network to which the HVDC links is connected, as a power sink. In Chapter 4 we extend this analysis to more general configuration. In particular we consider the case were dynamics of the external HVDC-interconnected cannot be neglected. The considered design criteria are stability of interarea modes, input usage, and stability in the event of dc link failure.

Due to the complexity and high order of the power systems, almost all works addressing POD rely on numerical studies. Although necessary for practical application, resorting to a numerical representation sacrifices physical intuition. In this thesis we build on the analytical approach of [20, 46, 67] to achieve more insight into the problem at hand. In [46], Smed and Andersson lay the foundational work for the theory used in this thesis. It is shown that active and reactive power control complement each other in the ability to provide POD. Since the focus of this work is on how electromechanical interactions limit achievable POD from HVDC interconnecting asynchronous grids, the focus of this work is on active power modulation.

In [20], Harnefors *et al.* investigate POD in asynchronous ac networks interconnected by a single point-to-point HVDC link. Active-power modulation using local frequency measurement is shown to be a robust control strategy both for sharing of primary reserves and providing POD to the interconnected systems. In Chapter 3 we investigate to what extent oscillation damping in the HVDC-interconnected system can be improved. Since we use active power modulation of the HVDC link the interconnected ac systems will interact. This causes limitations to achievable performance and may make POD improvement infeasible.

Chapter 3

Fundamental Performance Limitations

This chapter considers power oscillation damping (POD) using active power modulation of high-voltage direct current (HVDC) transmissions. An analytical study of how the proximity between interarea modal frequencies in two interconnected asynchronous grids puts a fundamental limit to the achievable performance is presented. It is shown that the ratio between the modal frequencies is the sole factor determining the achievable performance. This is of course assuming that the HVDC can provide the desired power and that the ac buses are strong enough to receive the power injections. Since the control cannot exceed rated HVDC power the latter of these points should not be an issue for a properly installed HVDC link. To verify the derived limitations, simulations using a proportional controller tuned to optimize performance in terms of POD are done. The influence of limited system information and unmodeled dynamics is shown on a simplified two-machine model. The analytical result is then tested on a realistic model with two interconnected 32-bus networks. The result shows that the analytical result are useful for assessing the fundamental performance limitations also as networks grow in complexity.

The proximity in frequency of two poorly damped oscillatory modes can be troublesome. It greatly affects the controllability of the interarea modes and therefore impairs the achievable POD from HVDC active power modulation. This *modal interaction* is the main focus of this chapter. In [20] it is shown that HVDC primary frequency control never decreases POD under some simplifying assumptions. This is proven by using a simple proportional droop controller, phase compensated for the HVDC active power actuation lag, with feedback from local frequency measurements at the two HVDC terminals. Such a control allows for efficient sharing of inertial response and primary reserves between the connected systems using only local measurements. In general, dc dynamics are orders of magnitude faster than interarea modes (see Section 2.4). For the remainder of this work, a residualized model [68] will be used, where faster dc dynamics are neglected. Instead, the focus will be on interactions occurring between ac systems interconnected with HVDC.

The main contribution of this chapter is to show how modal interaction lim-

its the achievable POD from HVDC active power modulation. This is done by extending the work of [20, 46, 67]. In our analysis, the well-known controllability Gramian [69, 70] is used to assess the controllability of the system. The Gramian gives a fundamental measure for how hard it is to control the interarea oscillations, independent of control structure.

The remainder of this chapter is organized as follows. In Section 3.1 nonlinear and linear models of the HVDC-interconnected system are defined. In Section 3.2, reduction of the linear model is done along with an energy interpretation. In Section 3.3, controllability analysis of the reduced model is made. In Section 3.4 and 3.5 a droop controller is synthesized and implemented in simulations to show POD performance and sensitivity. The chapter is summarized in Section 3.6.

3.1 Model of the HVDC-Interconnected System

Consider the HVDC-interconnected system in Figure 3.1. We let the dominant interarea mode in Network 1 (top) and Network 2 (bottom) be represented by two synchronous machines connected by an ac transmission line.

Machines are modeled, using the classical machine model, as a stiff electromotive force behind a transient reactance. Higher-order ac dynamics such as impact from machine damper windings, voltage regulators and system loads, governors etc. are lumped into the damping constant D_{ij}. In addition, transmission is assumed lossless and the electrical distance between machine ij and dc bus i is represented by the reactance X_{ij}, consisting of transient machine reactance, transformers, and transmission lines [15]. Thus, the electromechanical dynamics for network $i \in \{1, 2\}$ is given by the swing equation

$$\begin{aligned} \dot{\delta}_{ij} &= \omega_{ij} \\ M_{ij}\dot{\omega}_{ij} &= \underbrace{P_{m,ij} - P_{\text{load},ij}}_{\Delta P_{ij}} - \underbrace{\frac{V_{ij}V_i}{X_{ij}} \sin(\delta_{ij} - \theta_i)}_{P_{e,ij}} - D_{ij}\omega_{ij} \end{aligned} \tag{3.1}$$

for machines $j \in \{1, 2\}$, where δ_{ij} is the machine busbar-voltage, ω_{ij} represents machine ij's deviation from the nominal frequency ω_n. The constant M_{ij} represents the frequency and pole-pair scaled inertia of each machine.

The difference between the mechanical input power from the machines and the local loads is given by ΔPij. Since load dynamics are not of interest in the analysis, loads are assumed to act directly on generator states. DC busbar-voltage phase angle θ_i is given by the active power

$$P_{\text{DC}} + \sum_{j=1}^{2} \frac{V_{ij}V_i}{X_{ij}} \sin(\delta_{ij} - \theta_i) = 0 \tag{3.2}$$

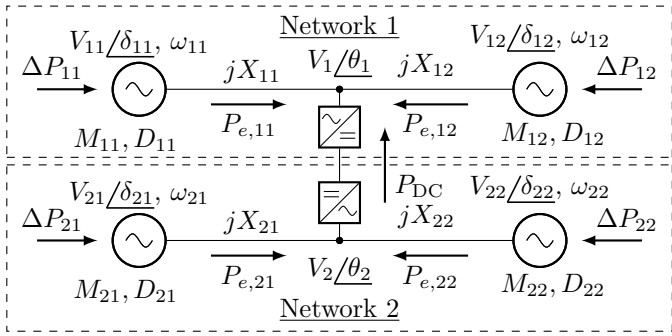

Figure 3.1: The HVDC-interconnected system used to study modal interaction, between two ac networks.

and reactive power balance

$$Q_{\mathrm{DC}} + \sum_{j=1}^{2} \frac{V_{ij} V_i \cos(\delta_{ij} - \theta_i) - V_i^2}{X_{ij}} = 0 \tag{3.3}$$

where P_{DC} and Q_{DC} is active and reactive power injected at the HVDC terminal. In addition we make the simplifying assumption that machine excitation and reactive power at the HVDC terminal are controlled (using, e.g., a voltage source converter HVDC terminal, a static var compensator, or a variable shunt capacitor bank) so that all buses have the voltage amplitude V for the time frame of interest [20].

Linearization and further simplifications commonly done in small-signal studies of power systems are made next. The second machine is set as phase reference in each network. Without loss of generality: $\delta_{i2} = 0$, $\Delta\delta_i = \delta_{i1} - \delta_{i2}$, and $\Delta\dot{\delta}_i = \omega_{i1} - \omega_{i2}$. Assuming small power flows, with $\Delta P_{ij} \approx 0$, gives small voltage phase-angle differences between buses. This implies that $\cos(\delta_{ij} - \theta) \approx 1$. If we let $Q_{\mathrm{DC}} = 0$ then (3.3) does not play a role in the small-signal dynamics. The assumption of small voltage phase-angle differences also implies $\sin(\delta_{ij} - \theta) \approx \delta_{ij} - \theta$ in (3.1) and, similarly, from (3.2) then approximately

$$\theta_i = \frac{X_{i2}}{X_{\Sigma,i}}\delta + \frac{X_{i1}X_{i2}}{V^2 X_{\Sigma,i}} P_{\mathrm{DC}}$$

where $X_{\Sigma,i} := X_1 + X_2$ is the total series impedance in Network i. These simplifications result in the linear state-space model

$$\begin{aligned} \dot{x}_i &= \mathcal{A}_i x_i + \mathcal{B}_i u \\ y_i &= \mathcal{C}_i x_i \end{aligned} \tag{3.4}$$

with state vector $x_i = \begin{bmatrix} \Delta\delta_i, & \omega_{i1}, & \omega_{i2} \end{bmatrix}^T$, input $u = P_{\mathrm{DC}}$, and y some general output.

For the study of POD and modal interaction, additional simplifications are possible without loss of relevant dynamics. This is essential in order to analytically analyze the HVDC-interconnected system. Only the electromechanical oscillations between the two machines are of interest. Therefore, only frequency in relation to the center of inertia (COI) frequency

$$\omega_{\mathrm{COI},i} = \frac{M_{i1}}{M_{\Sigma,i}}\omega_{i1} + \frac{M_{i2}}{M_{\Sigma,i}}\omega_{i2}$$

where $M_{\Sigma,i} = M_{i1} + M_{i2}$, needs to be considered. We therefore let the output vector be $y_i = \left[\Delta\delta_i,\, \omega_{i1} - \omega_{\mathrm{COI},i},\, \omega_{i2} - \omega_{\mathrm{COI},i}\right]$. Additionally, we make the following assumption that will let us reduce the system.

Assumption 3.1 (Damping Proportional to Inertia) The machine damping is evenly distributed and proportional to the machine inertia constant (which in turn is proportional to rated power)

$$D_{ij} = D_i \frac{M_{ij}}{M_{\Sigma,i}}$$

such that the machines become scaled versions of each other.

Remark 3.1 Since the mode (corresponding eigenvalue λ) is assumed poorly damped ($|\mathrm{Re}(\lambda)| \ll |\lambda|$) Assumption 3.1 has little effect on model accuracy. This is further discussed in the Section 3.2.

With Assumption 3.1, the system matrices in (3.4) becomes

$$\mathcal{A}_i = \begin{bmatrix} 0 & 1 & -1 \\ \frac{-V^2}{M_{i1}X_{\Sigma,i}} & \frac{-D_i}{M_{\Sigma,i}} & 0 \\ \frac{V^2}{M_{i2}X_{\Sigma,i}} & 0 & \frac{-D_i}{M_{\Sigma,i}} \end{bmatrix},\ \mathcal{B}_i = \begin{bmatrix} 0 \\ \frac{X_{i2}}{M_{i1}X_{\Sigma,i}} \\ \frac{X_{i1}}{M_{i2}X_{\Sigma,i}} \end{bmatrix} \tag{3.5}$$

and since

$$\omega_{i1} - \omega_{\mathrm{COI},i} = \left(1 - \frac{M_{i1}}{M_{\Sigma,i}}\right)\omega_{i1} - \frac{M_{i2}}{M_{\Sigma,i}}\omega_{i2} = \frac{M_{i2}}{M_{\Sigma,i}}\omega_{i1} - \frac{M_{i2}}{M_{\Sigma,i}}\omega_{i2}$$

the output matrix becomes

$$\mathcal{C}_i = \begin{bmatrix} 1 & 0 & 0 \\ 0 & \frac{M_{i2}}{M_{\Sigma,i}} & \frac{-M_{i2}}{M_{\Sigma,i}} \\ 0 & \frac{-M_{i1}}{M_{\Sigma,i}} & \frac{M_{i1}}{M_{\Sigma,i}} \end{bmatrix}. \tag{3.6}$$

3.2 Model Reduction and Energy Interpretation

In this section we discuss how to reduce the state dimension of the model introduced previously, and how to make a useful energy interpretation of the model.

Due to assumption (3.1), the two machines are linearly scaled versions of each other. Therefore, only machine frequency deviations, scaled by M_{i1} resp. M_{i2}, around $\omega_{\mathrm{COI},i}$ are observable in y_i. Hence, only the difference $\omega_{i1} - \omega_{i2}$ (and not the absolute states) is observable. Thus the model (3.4)–(3.6) is not a minimal realization but can be reduced further without losing additional control information [69].

Model Reduction

Let z_i be a reduced state vector that represents the observable subspace of (3.4)–(3.6) given by $z_i = P^\dagger x_i$. The transformation matrix P is time invariant and $P^\dagger$ is its Moore-Penrose pseudoinverse. A minimal (observable and controllable) realization of (3.4)–(3.6) is then

$$\begin{aligned} \dot{z}_i &= A_i z_i + B_i u \\ y_i &= C_i z_i \end{aligned} \tag{3.7}$$

where $A_i = P^\dagger \mathcal{A}_i P$, $B_i = P^\dagger \mathcal{B}_i$ and $C_i = \mathcal{C}_i P$ [69, Theorem 10.13].

For the analysis, it is convenient to let the reduced state vector $z_i = \left[\Delta\delta_i,\, \Delta\omega_i\right]^T$ where $\Delta\omega_i = \omega_{i1} - \omega_{i2}$. This is achieved by choosing

$$P^\dagger := \begin{bmatrix} 1 & 0 & 0 \\ 0 & 1 & -1 \end{bmatrix}. \tag{3.8}$$

The matrices in (3.7) thus become

$$\begin{aligned} A_i &= \begin{bmatrix} 0 & 1 \\ \frac{-V^2 M_{\Sigma,i}}{M_{i1} M_{i2} X_{\Sigma,i}} & \frac{-D_i}{M_{\Sigma,i}} \end{bmatrix}, \; B_i = \begin{bmatrix} 0 \\ \frac{M_{i2} X_{i2} - M_{i1} X_{i1}}{M_{i1} M_{i2} X_{\Sigma,i}} \end{bmatrix}, \\ C_i &= \begin{bmatrix} 1 & 0 & 0 \\ 0 & \frac{M_{i2}}{M_{\Sigma,i}} & \frac{-M_{i1}}{M_{\Sigma,i}} \end{bmatrix}^T \end{aligned} \tag{3.9}$$

where the undamped frequency of the interarea mode is given by

$$\Omega_i = \sqrt{\frac{V^2 M_{\Sigma,i}}{M_{i1} M_{i2} X_{\Sigma,i}}}. \tag{3.10}$$

This construction can be compared to the classical two-body problem of Newtonian mechanics [71]. From (3.9) it is easily seen that the interarea mode is controllable using active power injection, as long the HVDC terminal is not located at the mass-scaled electrical midpoint between the two machines, i.e., as long as $M_{i1} X_{i1} \neq M_{i2} X_{i2}$. This result is also found in [20, 46, 67]. To simplify the analysis further, consider the special case $M_{i1} = M_{i2} = M_i$, which we refer to as a *symmetric network*. The system matrices become

$$A_i = \begin{bmatrix} 0 & 1 \\ \frac{-2V^2}{M_i X_{\Sigma,i}} & \frac{-D_i}{2M_i} \end{bmatrix}, \; B_i = \begin{bmatrix} 0 \\ \frac{X_{B,i}}{M_i} \end{bmatrix}, \; C_i = \begin{bmatrix} 1 & 0 \\ 0 & 0.5 \\ 0 & -0.5 \end{bmatrix} \tag{3.11}$$

where $X_{B,i} = \frac{X_{i2}-X_{i1}}{X_{\Sigma,i}} \in [-1, 1]$ is the electric position of the dc bus in network i w.r.t. line impedance.

For system (3.9) to be a minimal realization of (3.4) it is required that the machines are scaled versions of each other according to Assumption 3.1. In the following example we study the effects of this assumption.

Example 3.1 (Consequence of Assumption 3.1) Consider a nominal network G_0 where Assumption 3.1 holds and a perturbed network G where there is no damping at the second machine.

- *Nominal network*, G_0. The nominal network is defined with $f_n = 50\,\text{Hz}$, unit voltage, unit line impedance and an undamped modal frequency set to $\Omega_1/2\pi = 0.5\,\text{Hz}$. From (3.10), $\Omega_1 = \sqrt{2/M}$ and thus $M = 2/\Omega_1^2$. The damping constant D at both machines are chosen such that the 0.5 Hz inter-area mode in the nominal network have a damping ratio of 8 % as shown in Appendix A.6.

- *Perturbed network*, G. In the perturbed network we let system damping be concentrated in machine 1. That is, let $D_1 = 2D$ and $D_2 = 0$.

In the reduced model (3.9) original state variables $\left[\Delta\delta_i,\, \omega_{i1},\, \omega_{i1}\right]^T$ are reduced to $\left[\Delta\delta_i,\, \Delta\omega_i = \omega_{i1} - \omega_{i1}\right]^T$. This reduction requires that Assumption 3.1 holds. In Figure 3.2 we study the accuracy of this reduction. The bode plot of the transfer function from input u to output $\Delta\omega_i$ are shown for the nominal and perturbed system respectively.

In Figure 3.2a we consider a system with $X_B = 0.5$, i.e., the dc bus is located close to machine 1. In Figure 3.2b the we consider a system with $X_B = -0.5$, thus the dc bus is closer to the machine without damping. In this case, low frequency response differ from the nominal case. However system gain is already low at these frequencies and at the modal frequency the system perturbations have little effect on system response. Thus, the proposed model reduction is fairly accurate also when Assumption 3.1 does not hold.

Remark 3.2 In modal analysis of power systems, it is common practice to describe system dynamics in terms of eigenvalues [15, 72] as shown in Appendix A.1. The resulting system matrix is diagonal and thus the dynamics of the system states are decoupled from each other. Therefore, the system can easily be reduced. However, as the representation result in complex valued system matrices it is not useful for the purpose of our analysis. As shown in Appendix A.4, a diagonal modal matrix can be transformed into a real Jordan form [73]. Here the system is represented in block diagonal form where complex conjugated eigenvalue pairs $\lambda_n = -\gamma_n \pm j\omega_{e,n}$, corresponding to modes of oscillation, are represented by real 2×2 blocks on the

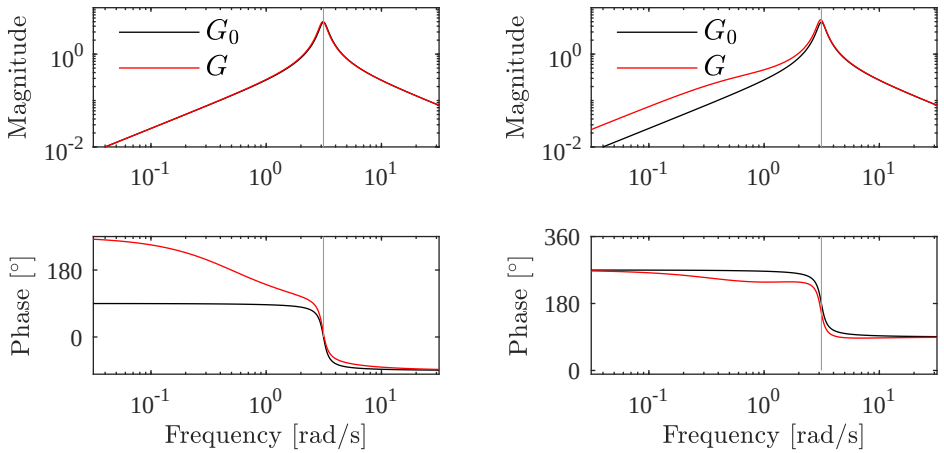

(a) DC bus location $X_B = 0.5$

(b) DC bus location $X_B = -0.5$

Figure 3.2: Transfer function of nominal (G_0) and perturbed system (G) from u to $\Delta\omega_i$ considering two different dc bus locations. Around modal frequency 0.5 Hz (gray line) system perturbation has little effect.

form

$$\begin{bmatrix} \gamma_n & \omega_{e,n} \\ -\omega_{e,n} & \gamma_n \end{bmatrix}.$$

If Assumption 3.1 holds then transformation with (3.8) also preserves the dynamics of the interarea oscillations. This, since the transformation matrix is a linear combination of the relevant eigenvectors. The benefit of the proposed reduction method is that the states of the new model reflects properties of the original system that are easy to study and interpret. If the assumption does not hold, the system can still be reduced but the new states are going to be a combination of original state variables, thus making analytical study infeasible.

Energy Interpretation

In this section we derive an expression for the *oscillatory energy* stored in Network i at state $\left[\Delta\delta_i,\, \Delta\omega_i\right]^T = \left[\delta_{0,i},\, \omega_{0,i}\right]^T$.

Interarea oscillations (or power oscillations) are electric power being transfered between machines. Consider the unforced, undamped symmetrical ac network shown in Figure 3.3, where the swing equation (3.1) gives

$$M_i\dot{\omega}_{0,i} = -2P_{e,i1} = -\frac{V^2}{X_{\Sigma,i}/2}\delta_{0,i}. \tag{3.12}$$

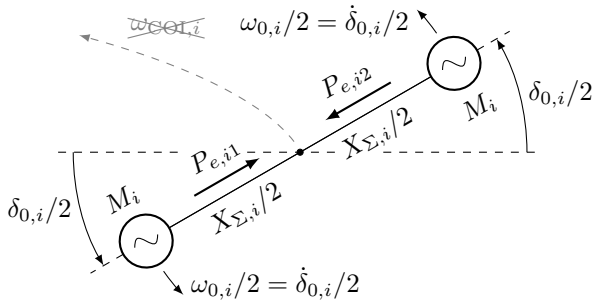

Figure 3.3: Visualization of a reduced two-machine ac network.

Work is the conversion between mechanical kinetic energy and electrical potential energy. Hence, power oscillations are an electromechanical phenomenon. Multiplying both sides in (3.12) by $d\Delta\delta_i/dt = \Delta\omega_i$ and deriving work done to both machines as the integral of power over time, t, we get

$$2\int M\omega_{0,i}\frac{d\omega_{0,i}}{dt}dt = -2\int \frac{V^2}{X_{\Sigma,i}/2}\delta_{i,0}\frac{d\delta_{0,i}}{dt}dt \tag{3.13}$$

or

$$\frac{2V^2}{X_{\Sigma,i}}\delta_{0,i}^2 + M\omega_{0,i}^2 = E_{\mathrm{p},i} + E_{\mathrm{k},i} =: E_{0,i} \tag{3.14}$$

where, since we are dealing with a conservative system, the sum of kinetic $E_{\mathrm{k},i} = M_i\omega_{0,i}^2$ and potential energy $E_{\mathrm{p},i} = \frac{2V^2}{X_{\Sigma,i}}\delta_{0,i}^2$ is constant over time [71]. This sum is referred to as the oscillatory energy $E_{0,i}$, which is the quantity we are interested in controlling using active power injection at the dc terminal.

Modeling the HVDC-Interconnected System

Using (3.7) together with (3.9) or (3.11), the HVDC-interconnected system in Figure 3.1 can now be described by

$$\dot{z} := \begin{bmatrix}\dot{z}_1\\ \dot{z}_2\end{bmatrix} = \begin{bmatrix}A_1 & 0\\ 0 & A_2\end{bmatrix}\begin{bmatrix}z_1\\ z_2\end{bmatrix} + \begin{bmatrix}B_1\\ -B_2\end{bmatrix}u =: Az + Bu. \tag{3.15}$$

3.3 Controllability Analysis

In this section we introduce some mathematical tool that are commonly known in control theory. These will be useful for the analysis of the system.

Consider a N-dimensional linear time invariant (LTI) system. As long as the controllability matrix

$$\mathcal{C} = \begin{bmatrix}B\, AB\, A^2B \cdots A^{N-1}B\end{bmatrix} \tag{3.16}$$

have full rank, the system is controllable.

Theorem 3.1 (Controllability Gramian [70]) *The LTI system* (3.15) *is controllable if and only if the controllability Gramian*

$$W_C = \int_0^T e^{At} B B^T e^{A^T t} dt. \tag{3.17}$$

is nonsingular for any $T > 0$.

Theorem 3.1 is equivalent to the controllability matrix (3.16) having full rank [70, Theorem 6.1]. However, the controllability Gramian has more uses as it gives us information on how hard the system is to control.

If damping constants D_1, $D_2 > 0$ then A is strictly Hurwitz, i.e., its eigenvalues have strictly negative real part. The controllability Gramian W_C over infinite time, $T = \infty$, can then be obtained by solving a Lyapunov equation.

Theorem 3.2 (Controllability Gramian $t \to \infty$ [70]) *If A is strictly Hurwitz, then the controllability Gramian, with $t \to \infty$, is given by the unique solution to the Lyapunov equation*

$$A W_C + W_C A^T + B B^T = 0. \tag{3.18}$$

The controllability Gramian gives us the minimal energy control, or *control effort*, required to transfer the system from one state to another.

Theorem 3.3 (Control Effort [70]) *The control effort required to transfer an initially disturbed system state, $z(t = 0) = z_0$, to the origin, $\lim_{t\to\infty} z(t) = 0$, is given by*

$$\|u\|_2^2 = z_0^T W_C^{-1} z_0$$

where $u \in L_2[0,\ \infty)$.

Definition 3.1 (Unitary Matrix [74]) A (complex) matrix $\mathcal{V}$ is unitary if its complex conjugate transpose

$$\mathcal{V}^H = \mathcal{V}^{-1}.$$

Definition 3.2 (Singular Value Decomposition (SVD) [74]) The SVD of a matrix $W \in \mathbb{C}^{N\times N}$ is based on the existence of orthogonal (unitary) matrices $\mathcal{U} \in \mathbb{R}^{N\times N}$ such that

$$W = \mathcal{U}\Sigma\mathcal{V}^H$$

where

$$\Sigma = \mathrm{diag}\{\sigma_1, \sigma_2, \ldots \sigma_N\}$$

and

$$\bar{\sigma} := \sigma_1 \geq \sigma_2 \geq \cdots \geq \sigma_N =: \underline{\sigma}$$

are the singular values of W. SVD is also applicable to non square matrices.

Since W_C is created from the square of two matrices (3.17) $W_C \geq 0$ and $W_C = W_C^T$. In addition W_C and thus $\mathcal{U}$ and $\mathcal{V}$ are real. This means that

$$W_C = \mathcal{U}\Sigma\mathcal{V}^T \Leftrightarrow W_C^T = \left(\mathcal{U}\Sigma\mathcal{V}^T\right)^T = V\Sigma U^T.$$

Consequently $\mathcal{V} = \mathcal{U}$, and $\sigma_n(W_C)$ is the same as the eigenvalue $\lambda_n(W_C)$.

With $z_n := v_n^T z_0$, where singular vectors v_n are the columns in $\mathcal{V}$, it follows that the control effort can be computed as

$$\|u\|_2^2 = z_0^T \mathcal{V}\Sigma^{-1}\mathcal{V}^T z_0 = \sum_{n=1}^{N} \frac{z_0^2}{\sigma_n}. \tag{3.19}$$

Assessing Controllability of an Isolated AC Network

Consider the single ac network i in (3.11) with $D_i > 0$, controlled with an arbitrary active power injection at the dc bus from a source with negligible dynamics, e.g., a large battery storage. By Theorem 3.2, the controllability Gramian for the two-machine network is (see Appendix A.5)

$$W_{C,i} = \frac{X_{B,i}^2}{D_i} \begin{bmatrix} \frac{X_{\Sigma,i}}{2V^2} & 0 \\ 0 & \frac{1}{M_i} \end{bmatrix}. \tag{3.20}$$

According to (3.19), the control effort required to transfer the system from an initially disturbed state to zero is given by

$$\|u\|_2^2 = z_{0,i}^T W_{C,i}^{-1} z_{0,i} = \frac{D_i}{X_{B,i}^2}\frac{2V^2}{X_{\Sigma,i}}\delta_{0,i}^2 + \frac{D_i}{X_{B,i}^2} M\omega_{0,i}^2. \tag{3.21}$$

Expressing (3.21) in the terms of oscillatory energy (3.14), we get

$$\|u_i\|_2^2 = \frac{D_i}{X_{B,i}^2}(E_{\mathrm{p},i} + E_{\mathrm{k},i}) = \frac{D_i}{X_{B,i}^2} E_{0,i}. \tag{3.22}$$

Here it is seen that control effort is inversely proportional to the squared (mass-weighted) electric position, $X_{B,i}^2$, of the dc terminal. This agrees with the findings of [20, 46, 67].

Remark 3.3 If we let $D_i = 0$, then the finite-time controllability Gramian (Theorem 3.1) gives us an intuitive interpretation of the required control effort (Theorem 3.3). The time, T, is a measure of the control aggressiveness.

For large T, we have (see Appendix A.5)

$$W_{C,i} \approx X_{B,i}^2 \frac{T}{2M_i} \begin{bmatrix} \frac{X_{\Sigma,i}}{2V^2} & 0 \\ 0 & \frac{1}{M_i} \end{bmatrix}$$

which is the same as (3.20) with

$$D_i = \frac{2M_i}{T}.$$

Thus, (3.18) is considered a good controllability estimate with $D_i > 0$ representing the control aggressiveness.

The finite-time controllability Gramian becomes impractical as the dimension of the system increases. Therefore, Theorem 3.2 will be used to analyze the HVDC-interconnected system.

Computing the Gramian W_C

The controllability Gramian (3.18) for the HVDC-interconnected system, computed using Kronecker products [75] (see Appendix A.5) yields

$$W_C = \begin{bmatrix} a_1 & -\alpha & 0 & -\gamma \\ -\alpha & a_2 & \gamma & 0 \\ 0 & \gamma & b_1 & -\beta \\ -\gamma & 0 & -\beta & b_2 \end{bmatrix} \tag{3.23}$$

with state variables ordered $z = \begin{bmatrix} \Delta\delta_1, \Delta\delta_2, \Delta\omega_1, \Delta\omega_2 \end{bmatrix}$. The elements of (3.23) depend on the parameters of Network 1 and 2. The main factor determining controllability is the undamped modal frequencies Ω_1 and Ω_2 in (3.10).

Assumption 3.2 (Identical Networks, Except for the Inertia Constant) For the following analysis we choose $M := M_1$, $M_2 := M + \epsilon$ and let the systems be identical in all other aspects, i.e., let $D_1 = D_2 =: D$ and $X_{\Sigma,1} = X_{\Sigma,2} =: X_\Sigma$. Note that $\Omega_1 \neq \Omega_2$ if $\epsilon \neq 0$.

The elements of (3.23) are then given by

$$\begin{aligned} a_1 &= a_2 = \frac{X_B^2}{D}\frac{X_\Sigma}{2V^2} =: a \\ b_1 &= \frac{X_B^2}{D}\frac{1}{M} =: b \\ b_2 &= b\frac{M}{M+\epsilon} \\ \alpha &= a\frac{2M+\epsilon}{2M+\epsilon+2c\epsilon^2} \\ \beta &= b\frac{2M}{2M+\epsilon+2c\epsilon^2} \\ \gamma &= \frac{X_B^2}{D^2}\frac{2\epsilon}{2M+\epsilon+2c\epsilon^2} \\ c &= \frac{2V^2}{D^2 X_\Sigma}. \end{aligned} \tag{3.24}$$

Here we note that $\alpha \to a$, $\beta \to b$, $b_2 \to b$, and $\gamma \to 0$, as $\epsilon \to 0$, which make W_C rank deficient. Moreover, the matrix of singular vectors is given by

$$\lim_{\epsilon\to 0} \mathcal{V} = \frac{1}{\sqrt{2}}\begin{bmatrix} 0 & 1 & 0 & 1 \\ 0 & -1 & 0 & 1 \\ 1 & 0 & 1 & 0 \\ -1 & 0 & 1 & 0 \end{bmatrix} \tag{3.25}$$

As can be expected for the control of a multivariable system, *directionality* will have to be considered [76]. With state variables ordered $z = \left[\Delta\delta_1,\, \Delta\delta_2,\, \Delta\omega_1,\, \Delta\omega_2\right]$ we see (according to (3.14)) that the interesting singular vectors corresponding to the least controllable directions represent potential energy, $E_\mathrm{p} := E_{\mathrm{p}1} + E_{\mathrm{p}2}$, $z_0 \in \mathrm{span}(v_4)$; and kinetic energy, $E_\mathrm{k} := E_{\mathrm{k}1} + E_{\mathrm{k}2}$, $z_0 \in \mathrm{span}(v_3)$. Interpreted as oscillatory energy, this becomes $E_0 := E_\mathrm{p} + E_\mathrm{k}$, $z_0 \in \mathrm{span}(v_3, v_4)$.

For small ϵ, networks will have similar modal frequencies, and controllability is going to be greatly affected by system interactions α, β and γ. The two smallest singular values of W_C corresponding to directions v_n with highest required control effort are the most interesting ones. Approximating these gives an analytical estimate of the controllability.

Making a Maclaurin series expansion of matrix elements (3.24) with respect to ϵ (see Appendix A.7) shows that for small ϵ

$$\left|\frac{d\alpha(\epsilon)}{d\epsilon}\right| < \left|\frac{d\beta(\epsilon)}{d\epsilon}\right| < \left|\frac{db_2(\epsilon)}{d\epsilon}\right| < \left|\frac{d\gamma(\epsilon)}{d\epsilon}\right|.$$

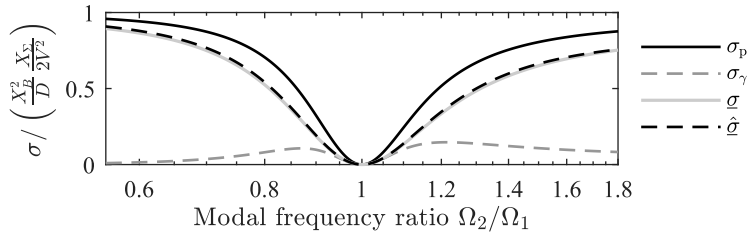

Figure 3.4: (Example 3.2) Estimated singular values σ_γ and σ_{p} together with numerically calculated $\underline{\sigma}$ and estimate $\underline{\hat{\sigma}}$. Modal frequencies Ω_1 and Ω_2 according to (3.10) and Assumption 3.2.

A simplification of W_C, accurate for small ϵ, is then

$$W_C^\gamma := \begin{bmatrix} a & -a & 0 & -\gamma \\ -a & a & \gamma & 0 \\ 0 & \gamma & b & -b \\ -\gamma & 0 & -b & b \end{bmatrix}$$

where the smallest singular value becomes

$$\sigma_\gamma := \min\left(\mathrm{svd}(W_C^\gamma)\right) = \left| b - \sqrt{(b^2+\gamma^2)} \right|. \tag{3.26}$$

Maclaurin series expansion of σ_γ gives the estimate

$$\sigma_\gamma(\epsilon) = \frac{X_B^2}{D} \frac{1}{2D^2 M} \epsilon^2 + \mathcal{O}(\epsilon^3). \tag{3.27}$$

Example 3.2 In Figure 3.4 we let the networks 1 and 2 be defined with $f_n = 50\,\mathrm{Hz}$, $X_B = 0.5$, unit voltage, unit line impedance and the undamped modal frequency are set to $\Omega_1/2\pi = 0.5\,\mathrm{Hz}$. From (3.10), $\Omega_1 = \sqrt{2/M}$ and thus $M = 2/\Omega_1^2$.

To study how modal interaction affects controllability, the undamped modal frequency in Network 2 is set to $\Omega_2 = \sqrt{2/(M+\epsilon)}$ according to Assumption 3.2.

The damping constant D are chosen such that the $0.5\,\mathrm{Hz}$ interarea mode in Network 1 have a damping ratio of $8\,\%$ as shown in the Appendix A.6.

As seen in Figure 3.4, the estimate (3.26) is only accurate for small ϵ. For slightly larger ϵ the properties of W_C is dominated by the diagonal blocks

$$W_C^{\mathrm{p}} := \begin{bmatrix} a & -\alpha \\ -\alpha & a \end{bmatrix} \text{ and } W_C^{\mathrm{k}} := \begin{bmatrix} b & -\beta \\ -\beta & b_2 \end{bmatrix}$$

in (3.23), where, the smallest singular value

$$\sigma_{\mathrm{p}} := \min\left(\mathrm{svd}(W_C^{\mathrm{p}})\right) = |a - \alpha|$$

together with (3.24) becomes

$$\sigma_{\mathrm{p}}(\epsilon) = \frac{X_B^2}{D}\frac{X_\Sigma}{2V^2}\frac{2c\epsilon^2}{2M+\epsilon+2c\epsilon^2}. \tag{3.28}$$

Maclaurin series expansion of (3.28) yields

$$\sigma_{\mathrm{p}} = \frac{X_B^2}{D}\frac{cX_\Sigma}{2D^2M}\epsilon^2 + \mathcal{O}(\epsilon^3).$$

With $c = \frac{2V^2}{D^2X_\Sigma}$ according to (3.24) (3.28) becomes

$$\sigma_{\mathrm{p}}(\epsilon) \approx \frac{X_B^2}{D}\frac{1}{D^2M}\epsilon^2. \tag{3.29}$$

From (3.27) we have that that for small ϵ

$$\sigma_\gamma(\epsilon) \approx \frac{X_B^2}{D}\frac{1}{2D^2M}\epsilon^2. \tag{3.30}$$

For the second-order term of (3.29) to match that of (3.30), c in (3.28) needs to be replaced by $c/2$, suggesting the estimate

$$\hat{\underline{\sigma}}(\epsilon) = \frac{X_B^2}{D}\frac{X_\Sigma}{2V^2}\frac{c\epsilon^2}{2M+\epsilon+c\epsilon^2}. \tag{3.31}$$

As seen in Figure 3.4 this is a fairly accurate analytical estimate of the real singular value.

Modal Interaction and Energy Interpretation

From (3.10) and Assumption 3.2 it follows that

$$\epsilon = \frac{2V^2}{X_\Sigma\Omega_2^2} - M. \tag{3.32}$$

Substituting (3.32) in (3.31) yields

$$\hat{\underline{\sigma}}(\epsilon) = \frac{2V^2}{X_\Sigma}\frac{D}{X_B^2}\left(1 + D^2\frac{1+\Omega_1^2/\Omega_2^2}{\frac{2V^2M}{X_\Sigma}(1-\Omega_1^2/\Omega_2^2)^2}\right).$$

The control effort required for an initial disturbed state, $z_0 \in \mathrm{span}(v_4)$ and $E_{\mathrm{p}} = v_4^T\frac{2V^2}{X_\Sigma}v_4$ becomes

$$\|u\|_2^2 \approx E_{\mathrm{p}}\frac{D}{X_B^2}\left(1 + D^2\frac{1+\Omega_1^2/\Omega_2^2}{\frac{2V^2M}{X_\Sigma}(1-\Omega_1^2/\Omega_2^2)^2}\right) \tag{3.33}$$

However, as implied by (3.22) and (3.25), (3.33) holds for any $z_0 \in \text{span}(v_3, v_4)$ thus E_p can be replaced by E_0. This allows us to express the worst-case required control effort due to modal interaction between the HVDC-interconnected ac networks as

$$\|u_D\|_2^2 := E_0 \frac{D}{X_B^2} \left(1 + D^2 \frac{1 + \Omega_1^2/\Omega_2^2}{\frac{2V^2M}{X_\Sigma}(1 - \Omega_1^2/\Omega_2^2)^2} \right). \tag{3.34}$$

The subscript D indicates that the controllability Gramian is calculated using Theorem 3.2 and thus depends on the damping constant.

Remark 3.4 For differences in the HVDC-interconnected networks parameters, some adjustments to (3.34) is needed to get an accurate estimate (see Appendix A.8). This is however left out here for the sake of readability.

In Figure 3.5 the estimate (3.34) is compared with numerical results using a finite-time controllability Gramian (3.17) for an undamped system

$$\|u_T\|_2^2 := z_0^T \left(\int_0^T e^{At} B B^T e^{A^T t} dt \right)^{-1} z_0 \tag{3.35}$$

where $z_0 \in \text{span}(v_3, v_4)$ and we let $T \propto 1/D$ used in (3.34). For the graphical comparison in Figure 3.5, the measures (3.34) and (3.35) are normalized as

$$\|\bar{u}_D\|_2 := \left(1 + D^2 \frac{1 + \Omega_1^2/\Omega_2^2}{\frac{2V^2M}{X_\Sigma}(1 - \Omega_1^2/\Omega_2^2)^2} \right) \tag{3.36}$$

and

$$\|\bar{u}_T\|_2 := \sqrt{\frac{\|u_T\|_2^2}{\|u_{T,1}\|_2^2 + \|u_{T,2}\|_2^2}} \tag{3.37}$$

where $\|u_{T,1}\|_2^2$ and $\|u_{T,2}\|_2^2$ are the corresponding finite-time minimal control effort for Network 1 and Network 2, respectively.

Remark 3.5 In Figure 3.5 it is shown how the modal interaction puts a limit to how aggressive the control action can be. As for a single ac network (see Remark 3.3) an inverse relation between D and T is seen. This indicates that D is a reasonable representation of control aggressiveness also for the interconnected system.

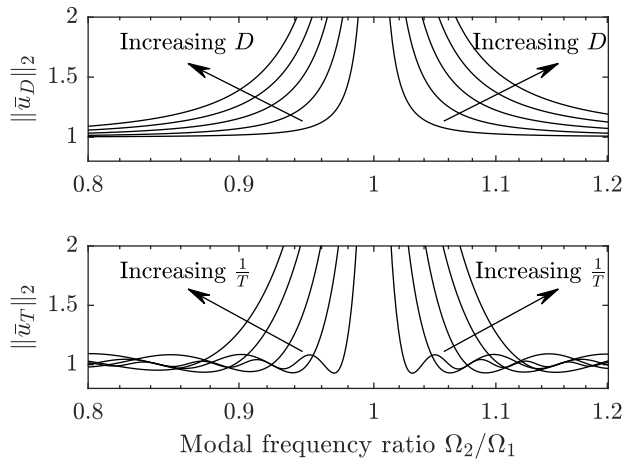

Figure 3.5: The normalized minimal energy control calculated using (3.36)(top) with D chosen to give damping factor $\zeta = \{2, 4, 6, 8, 10\,\%\}$ and (3.37) (bottom) with no inherent damping and $T = 1/D$. It follows that a more aggressive control comes at the cost of increased sensitivity to modal interaction.

3.4 Control Synthesis

As seen in Section 2.1, oscillatory instability is caused by a lack of damping torque. In this section, a controller designed to optimize achievable damping torque by maximizing the minimal system damping ratio is proposed.

First consider an individual network

$$\dot{z}_i \begin{bmatrix} 0 & 1 \\ \frac{-2V^2}{M_i X_{\Sigma,i}} & \frac{-D_i}{2M_i} \end{bmatrix} z_i + \begin{bmatrix} 0 \\ \frac{X_{B,i}}{M_i} \end{bmatrix} u.$$

With $u = -K_i \Delta\omega_i,\ K_i > 0$ we see that damping torque is improved as the complex eigenvalue pair is moved left in the complex plane [46]. With an increasing gain K_i system performance in terms of POD is improved if controlled from a source with negligible dynamics, e.g., a large battery storage. However, as shown in Section 3.3, modal interaction will put a limit to achievable POD performance in the HVDC-interconnected system.

Consider the HVDC-interconnected system depicted in Figure 3.1. The input $u = P_{\mathrm{DC}}$ is controlled with proportional feedback. Neglecting the HVDC actuation lag, the following control law is used:

$$u = P^0_{\mathrm{DC}} - Ky. \tag{3.38}$$

Here we propose the output signal

$$y = \begin{bmatrix} \Delta\omega_1 \\ \Delta\omega_2 \end{bmatrix} := \begin{bmatrix} \omega_{11} - \omega_{12} \\ \omega_{21} - \omega_{22} \end{bmatrix} \tag{3.39}$$

to increase the damping torque and to target the oscillatory energy in each system. For simplicity a proportional droop controller, $K = \begin{bmatrix} K_1, & -K_2 \end{bmatrix}$ is considered.

Let λ_n, $n \in \{1, \ldots, N\}$ be the eigenvalues of the closed-loop system

$$\dot{z} = Az - BKy. \tag{3.40}$$

The damping ratio of the modes is given by

$$\zeta_n = -\mathrm{Re}(\lambda_n)/|\lambda_n|$$

with the minimal damping ratio for all N modes given by

$$\zeta_{\min} := \min_{n \in \{1,\ldots,N\}} \zeta_n.$$

For optimal performance in terms of POD, we seek K such that

$$\max_K \min_{n \in \{1,\ldots,N\}} \zeta_n. \tag{3.42}$$

This control strategy requires that a good estimate of y is available, which for practical application could be obtained using local or external measurements [77].

Detailed Model Specification

To illustrate the control strategy on a more detailed system, we consider a HVDC-interconnected system as seen in Figure 3.1 where each network $i \in \{1, 2\}$ is represented using two synchronous machines $j \in \{1, 2\}$ where

- the nonlinear dynamics given by (3.1), (3.2) are considered; item we allow asymmetric networks with $X_{B,1} \neq X_{B,2}$ and

$$M_{i1} := M_i, \; M_{i2} := \alpha_i M_i;$$

- each machine is equipped with primary frequency control, whose active power injection is given by the first-order governor

$$P_{m,ij} = P^0_{m,ij} - \frac{1}{sT_g + 1} \frac{R_g}{\omega_n} \omega_{ij} \tag{3.43}$$

with time constant $T_g = 2\,\mathrm{s}$ and droop gain $R_g = 25\,\mathrm{p.u.}$ for all machines;

- HVDC is utilized to share primary frequency reserves by adding the additional primary control to (3.38)

$$u = P_{\mathrm{DC}}^0 - Ky + \frac{1}{sT_{\mathrm{DC}}+1}\frac{R_{\mathrm{DC}}}{\omega_n}(\omega_{\mathrm{COI},1} - \omega_{\mathrm{COI},2}) \tag{3.44}$$

  where $T_{\mathrm{DC}} = 2\,\mathrm{s}$ and $R_{\mathrm{DC}} = 50\,\mathrm{p.u.}$

Four cases of HVDC-interconnected ac networks as specified in Table 3.1 are considered. The system parameters are given in per unit (p.u.). Common to all cases is that we let $D_1 = D_2 = 2/\omega_n$, $\alpha_1 = \alpha_2 = 1$, and primary control at machines and dc terminals as specified by (3.43) and (3.44). Machine inertia constant $M_i = 2H_iS_r/\omega_n$ are based on the inertia time constant H, which usually falls within 3–8 s for a power system dominated by synchronous machines [15]. Rated power of each machine is set to $S_r = 4\,\mathrm{p.u.}$, $f_n = 50\,\mathrm{Hz}$, and $V_1 = V_2 = 1\,\mathrm{p.u.}$ Network impedance is given by (3.10) such that $\Omega_i, i \in 1, 2$ are obtained for the cases in Table 3.1. As an example, $\left[X_{\Sigma,1},\, X_{\Sigma,2}\right] \approx \left[1.3,\, 1.2\right]$ for Case 1. The active power injection is consumed locally at each machine bus. Hence, $\Delta P_i = P_{e,i} = P_{\mathrm{DC}}^0 = 0,\ \forall i$.

Table 3.1: The four considered cases together with optimal gain and damping obtained for simplified and detailed model.

Case	1		2		3		4	
Network	1	2	1	2	1	2	1	2
$\Omega/2\pi$ [Hz]	0.5	0.525	0.5	0.6	0.5	0.6	0.5	0.6
H [s]	6	6	6	6	4	6	6	6
X_B	0.5	0.5	0.5	0.5	0.5	0.5	0.8	0.5

Reconstructing a Simplified Model

The controllability analysis done in Section 3.3 and the control strategy (3.42) are based on a simplified model where higher-order dynamics such as primary frequency control, (3.43) and (3.44), are lumped into the damping constant D. The effect of the unmodeled dynamics is studied by synthesizing a controller based on the simplified forth order HVDC-interconnected system model (3.11). Performance, in terms of POD, is then compared between the simplified and the detailed model.

To investigate the sensitivity to unmodeled dynamics we assume that the only information available is the estimated eigenvalues $\hat{\lambda}_n = -\hat{\gamma}_n \pm j\hat{\omega}_{e,n}$. In particular interest are the eigenvalues representing the poorly damped interarea mode in Network 1 and Network 2, respectively. Using this information, a model of the reduced networks in (3.9) is reconstructed by solving the characteristic equation of A_i:

$$\Delta\ddot{\delta}_i + \underbrace{\frac{D_i}{M_{\Sigma,i}}}_{2\gamma_i}\Delta\dot{\delta}_i + \underbrace{\frac{V_i^2 M_{\Sigma,i}}{M_{i1}M_{i2}X_{\Sigma,i}}}_{\Omega_i^2}\Delta\delta_i = 0. \tag{3.45}$$

Remark 3.6 From the characteristic equation (3.45), and the state space representation (3.9), we see that proportional (negative) feedback of $\Delta\omega_i = \Delta\dot{\delta}_i$ will move the pole straight in the negative real direction. This will increase the damping torque (in phase with $\Delta\omega_i$) of the electromechanical mode.

Since the mode is poorly damped, we assume $\omega_{e,i} \approx \Omega_i$. Proposing some parameter estimates $\hat{H}_i$, $\hat{X}_{B,i}$, and $\hat{\alpha}_i$ allows us to reconstruct the second order state-space representation (3.9)

$$\hat{G}_i \overset{s}{=} \left[\begin{array}{c|c} \hat{A}_i & \hat{B}_i \\ \hline \hat{C}_i & 0 \end{array}\right]$$

of each network. The HVDC controller is then tuned on the interconnected model

$$\hat{G} = \begin{bmatrix} \hat{G}_1 \\ -\hat{G}_2 \end{bmatrix}$$

using (3.42).

Tuning Result Using Reconstructed Model

In this section we compare the result using the reconstructed and the detailed model for tuning. In Table 3.2 it is seen that the controller gains $\hat{K}$ result in slightly lower POD when applied to the detailed model ($\zeta_{\min} < \hat{\zeta}_{\min}$). Comparing $\hat{K}$ with the optimal gain obtained for the detailed system K^*, we see that a good conservative approach to account for these unmodeled dynamics would be to scale $\hat{K}$ with some factor smaller than one. The main reason for POD deterioration is the HVDC primary control (3.44), which could be taken into account in the tuning process. In Figure 3.6 the minimal system damping ratio $\zeta_{\min}$ for Case 3 is shown as a

Table 3.2: Feedback gain $\hat{K}$ and $\hat{\zeta}_{\min}$ are obtained by solving (3.42) for a reconstructed simplified model (see Section 3.4) while $\zeta_{\min}$ is the actual damping ratio achieved using $\hat{K}$ on the complete detailed model. Optimal gain feedback gain K^* and $\zeta^*_{\min}$ are obtained by solving (3.42) with complete knowledge of the system.

	Case	1		2		3		4	
	Network	1	2	1	2	1	2	1	2
Reconstructed simplified model	$\hat{K}$ [Hz^{-1}]	0.27	0.29	1.02	1.23	0.64	1.18	0.64	1.24
	$\hat{\zeta}_{\min}$ [%]	2.9		9.4		9.2		9.4	
	$\zeta_{\min}$ [%]	2.2		7.0		6.9		7.0	
Complete model	K^* [Hz^{-1}]	0.26	0.29	1.02	1.22	0.64	1.18	0.64	1.23
	$\zeta^*_{\min}$ [%]	2.7		9.1		9.0		9.2	

function of both K_1 and K_2 while Figure 3.7 shows the highest $\zeta_{\min}$ achieved at each given K_1. In Figure 3.7 it is seen that lowering the inertia, or moving the

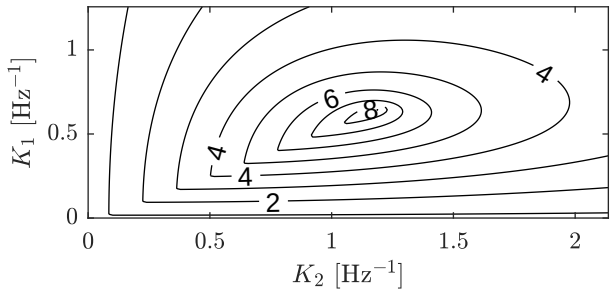

Figure 3.6: Case 3: Level curves for the minimal system damping ratio $\zeta_{\min}$ [%] as a function of both K_1 and K_2.

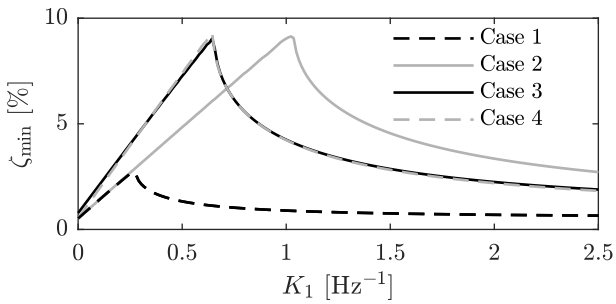

Figure 3.7: The highest minimal system damping ratio $\zeta_{\min}$ as a function of K_1.

dc bus location closer to one of the generator as in 3 and 4, respectively, makes Network 1 more controllable. Feedback gain K_1 consequently has a higher effect on POD in Network 1. However, its seen that only the modal frequency ratio Ω_1/Ω_2 will have a significant effect on optimal performance as indicated in Section 3.3. Consequently, this means a lower optimal K_1 for the more controllable cases.

Root Locus

Let the HVDC POD controller be $K = kK'$, where K' is either or $\hat{K}$ or K^* obtained from the reconstructed or detailed model respectively. In Figure 3.8 the root locus of the HVDC-interconnected system is drawn showing poles of the poorly damped interarea modes as k goes from zero to infinity. Note that oscillatory modes appear as complex conjugates. For clarity only the eigenvalues with positive imaginary part are shown in Figure 3.8. Their conjugate counterparts are mirrored over the real axis.

As the gain increases the poles move towards each other until they diverge. At the bifurcation point the eigenvalues of the two system are identical. Afterwards they split up into two new eigenvalues pairs. The pair corresponding to the easily

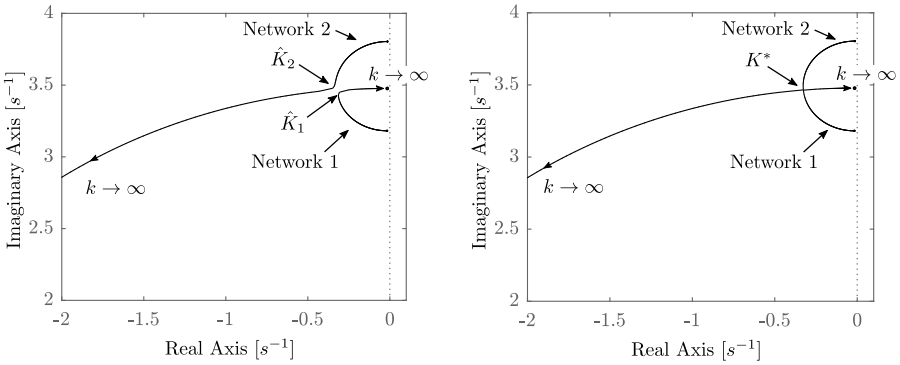

(a) Controller tuned using reconstructed model, $K = k\hat{K}$

(b) Controller tuned using detailed model, $K = kK^*$

Figure 3.8: Case 2: Root locus of the electromechanical mode in each of the HVDC-interconnected systems using HVDC POD control.

controllable system direction (which in Section 3.3 corresponds to state variables in $\text{span}(v_1, v_2)$) continues into the left hand plane. The pair that corresponds to the least controllable directions $\text{span}(v_3, v_4)$ moves back towards the imaginary axis until all additional damping from the HVDC control is lost. This might be a problem if one of the ac networks are inherently unstable. The innacurracy of the reconstructed model causes the poles to diverge when they are further apart, as seen in Figure 3.8a.

Simulation Study

MATLAB simulations using the model considered in Section 3.4 are presented next. A disturbance in the form of a sudden 0.4 p.u. load increase at machine-bus 1 in Network 1 is the considered scenario.

Machine speeds with feedback gain $\hat{K}$ obtained from the simplified model, using the procedure introduced in Section 3.4, are presented in Figures 3.9 and 3.10 for Case 1 and 2, respectively.

An immediate frequency fall can be seen at machine-bus 1 in Network 1 where the load increase occurs. The load imbalance causes a separation in machine speeds and an ensuing power oscillation between the two machines. The proposed control scheme (3.40) is implemented to increase POD, consequently spreading the power oscillation to the assisting network. A larger difference between Ω_1 and Ω_2 gives a lower modal interaction between the networks according to Section 3.3. Hence, Case 2 facilitates a higher POD performance compared to Case 1. A higher feedback gain moves Ω_1 and Ω_2 closer to each other as seen in Figure 3.8. As the modal frequencies move closer to each other, controllability and thus, POD benefits are reduced.

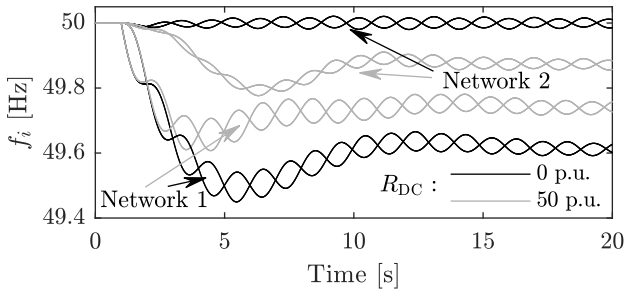

Figure 3.9: Case 1: Machine speeds for the HVDC-interconnected two-machine networks following a 0.4 p.u. load increase in Network 1 (bottom line-pair) aided by Network 2 (top line-pair). Gray and black lines shows performance with and without sharing of primary reserves through the HVDC link (3.44), respectively.

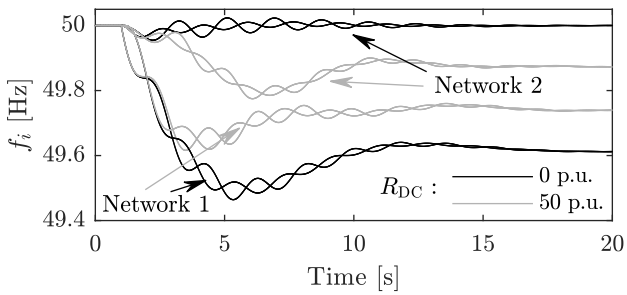

Figure 3.10: Case 2: Scenario identical to Figure 3.9.

To illustrate the effect of primary control (3.44) we also consider a model with $R_{\mathrm{DC}} = 0$ in both cases. Comparing the cases with primary control (gray lines), to those without (black lines) we see that sharing of primary reserves, to reduce nadir and steady state frequency deviation, can be implemented independent of POD control.

Sensitivity to Parameter Estimates

To show the effect of misjudging the dc busbar location in the tuning process, we consider Case 2 (see Table 3.1) with two different estimates of $\hat{X}_B$, given in Table 3.3. Here we let $R_{\mathrm{DC}} = 0$ so as to not get interference from primary control.

External Measurement

First we study the case where the ideal feedback signal from (3.39)

$$y = \begin{bmatrix} \Delta\omega_1 \\ \Delta\omega_2 \end{bmatrix} \tag{3.46}$$

is available using communication from remote phasor measurement units at the machine busbars.

Local Measurement

Assume that $\Delta\omega_i$ is estimated using local frequency measurements at the dc terminals. A good estimate, $\Delta\hat{\omega}_i$, will require accurate knowledge of the model. Missjudging the observability (which for this case is the same as the controllability $X_{B,i}$) will affect the magnitude of the estimate and will therefore give the same effect as an incorrectly tuned feedback gain. Since the focus of this chapter is not on observer design we are here assuming that

$$\Delta\hat{\omega}_i = \Delta\omega_i \frac{X_{B,i}}{\hat{X}_{B,i}} \tag{3.47}$$

i.e., if the observability is underestimated we are going to have an overestimate of $\Delta\omega_i$. In Table 3.3 we see how the use of local measurements makes the control method more sensitive to model error.

Table 3.3: Sensitivity to parameter estimate $\hat{X}_B$ using ideal feedback $\Delta\omega$ (3.46) and estimate $\Delta\hat{\omega}$ (3.47) from local frequency measurements.

			Feedback Signal		$\Delta\omega$		$\Delta\hat{\omega}$	
Case	$\hat{X}_B$	$\hat{K}_1$	$\hat{K}_2$ [Hz^{-1}]	$\hat{\zeta}_{\min}$	ζ_1	ζ_2	ζ_1	ζ_2 [%]
2	0.5	1.08	1.31	9.4	9.9	8.8	9.9	8.8
2.a	0.25	2.16	1.31	9.4	24	3.2	44	1.5
2.b	0.75	0.72	1.31	9.4	5.5	10	3.8	10
2.0	-	-	-	-	0.52	0.39	0.52	0.39

Remark 3.7 In practice $\Delta\hat{\omega}_i$ could be obtained using a washout or band-pass filter, in which case transient response and phase would be affected by model error and filter tuning. To achieve a more robust estimate, additional feedback signals such as ac power flow and voltage could be used.

Simulation of Oscillatory Energy Following a Load Step

In Case 2.a, where controllability and observability is underestimated, an overestimated $\hat{K}_1$ greatly increases POD performance in Network 1 at the cost of overall

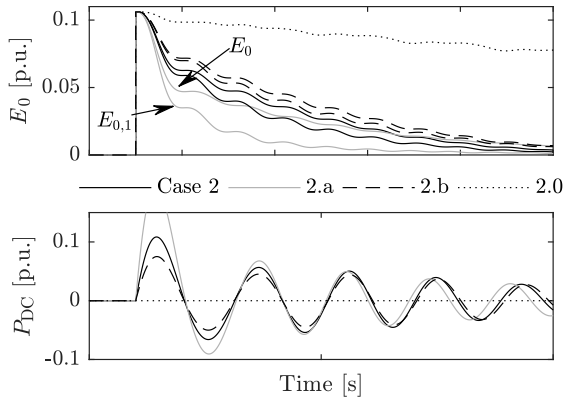

Figure 3.11: Oscillatory energy (top) following a 0.4 p.u. load increase in Network 1 for the cases specified in Table 3.3, with the resulting P_{DC} (bottom). Per unit energy is calculated using (3.13), where the potential energy is in relation to pre- and post-disturbed steady state. Control is implemented using ideal feedback $\Delta\omega$.

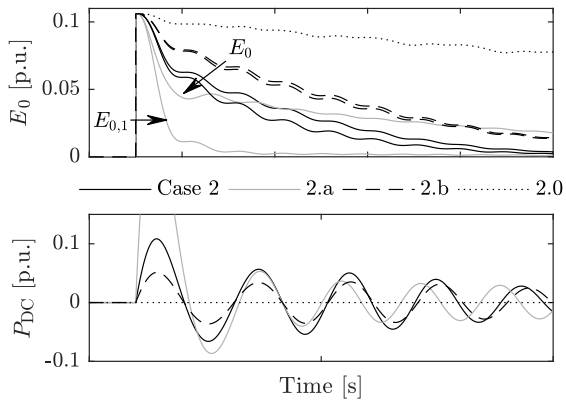

Figure 3.12: Same scenario as in Figure 3.11 but with feedback signal $\Delta\hat{\omega}$ (3.47). We see that the dependency on observability of $\Delta\omega$ from local measurements gives increased sensitivity to model error.

system performance, measured by $\zeta_{\min}$. In Figures 3.11 and 3.12 the oscillatory energy (3.13) following a sudden 0.4 p.u. load increase at machine-bus 1 is shown. The oscillatory energy E_0 in the disturbed network is greatly reduced due to a high initial P_{DC}. This however, introduce a large oscillatory energy $E_{0,2}$ in the assisting network where the POD is lower, reducing overall system performance. Comparing Figure 3.11 with Figure 3.12 we see that the negative impact of model error

increases if we also considers the effect on observability. As can be seen, underestimating $\hat{K}$ in Case 2.b gives the opposite result. For comparison Case 2.0 gives an base reference where POD control is not utilized. From Case 2.0 we see that even though badly tuned K gives poor POD, we can always expect an improvement from the case without POD control.

3.5 Simulation Study: Two Nordic 32-Bus Networks

To improve the confidence in the analytical results, simulations on more detailed power system models are made in Simulink. We consider the Nordic 32-bus Cigré test systems (N32) [21]. The model is implemented in Simulink Simscape Electrical with synchronous machines, excitation systems, governors, transmission, transformers, and load characteristics as specified in [21]. The N32 model is a system with large power transfers from the hydro dominated north and external areas (lumped into north area) to loads in the central and southwestern areas (lumped into the south area) where a large amount of thermal power is installed. The implemented N32 model shows a 0.5 Hz interarea mode Ω between the north and south areas. For illustrative purposes, the damping of this mode is reduced to roughly 1% by modifying the PSS at machines 4072 and 1042.

For the study, an artificial system is created by interconnecting two separate N32 networks with a point-to-point HVDC link as shown in Figure 3.13. Four cases with different system topologies are considered. In Cases 1 and 2 the dc link is located at bus 4045 in both ac networks. In Cases 3 and 4 the dc terminal is moved to bus 4072 in Network 1. To illustrate limitations imposed by modal interaction, the inertia time constants are scaled to modify modal frequencies (3.10) of Network 2. The cases are summarized in Table 3.4.

HVDC POD Controller

The HVDC active power is modulated using (3.40) with the relative frequency difference

$$y_i = \frac{\sum_{j\in\text{south}} M_{ij}\omega_{ij}}{\sum_{j\in\text{south}} M_{ij}} - \frac{\sum_{j\in\text{north}} M_{ij}\omega_{ij}}{\sum_{j\in\text{north}} M_{ij}} \tag{3.48}$$

as a single machine equivalent [28, 78] feedback signal from each network.

The signal is obtained by communicating the machine measurements to the dc controller. A proportional controller is implemented using the tuning procedure introduced in Section 3.4. The second-order system representation (3.7), used in the tuning process, is obtained using Simulink's Linear Analysis Tool.

The result shown in Table 3.5 confirms the analytic result that modal interaction limits the potential POD benefits from active power modulation. The control, tuned to each specific case, exploits the modal frequencies. With higher gains they move closer to each other and the system lose controllability of the interarea modes. Moving the dc terminal to the more controllable position at bus 4072 in Cases 3

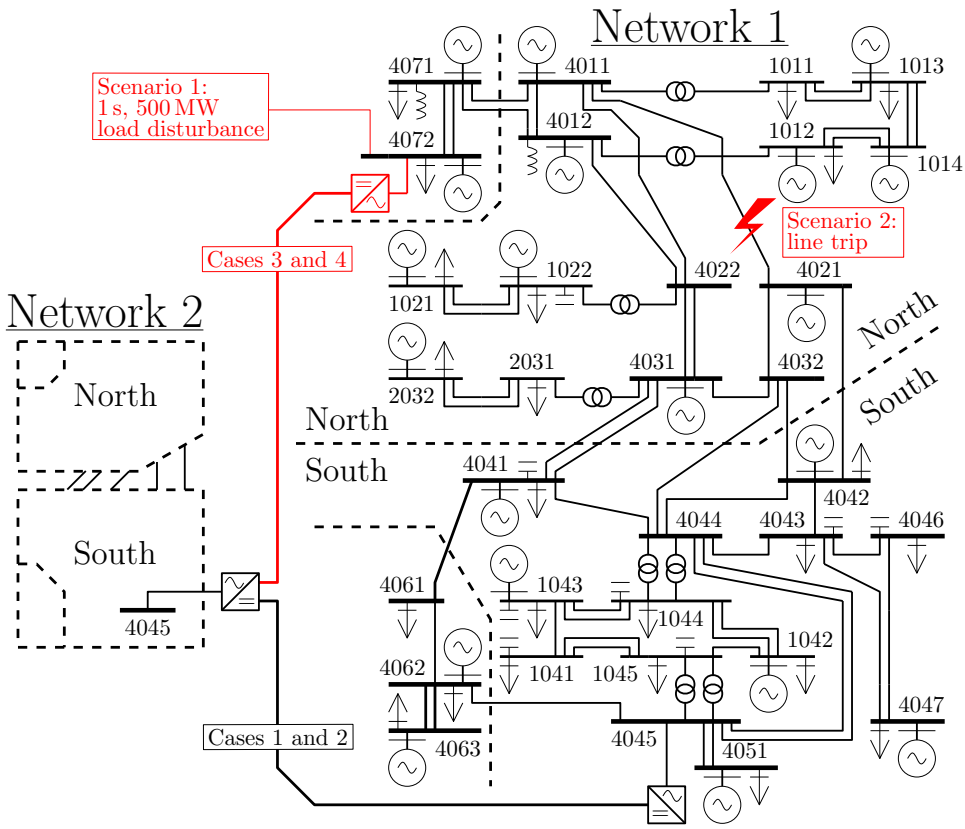

Figure 3.13: The artificial network model consisting of two HVDC-interconnected N32 networks [21].

Table 3.4: Modal frequencies and dc buses of the four considered cases of HVDC-interconnected N32 networks.

Case	1		2		3		4	
Network	1	2	1	2	1	2	1	2
$\Omega/2\pi$ [Hz]	0.51	0.53	0.51	0.60	0.51	0.53	0.51	0.60
DC Bus	4045	4045	4045	4045	4072	4045	4072	4045

and 4 reduces the required dc power actuation but have negligible effect on resulting POD performance.

Simulation Results

To verify the results, simulations of the nonlinear system where made.

Table 3.5: Resulting POD of the HVDC-interconnected N32 networks. Controller K_i is tuned to the corresponding Case i.

Controller	K_1	K_2	K_3	K_4
Gain [MW/Hz]	453 617	1558 1675	190 514	663 1410
$\hat{\zeta}_{\min}$ [%]	3.4	9.4	3.2	8.6
$\zeta_{\min}$(Case 1) [%]	2.9	1.4	1.8	1.6
$\zeta_{\min}$(Case 2) [%]	3.0	6.9	1.8	3.7
$\zeta_{\min}$(Case 3) [%]	1.5	0.9	2.9	1.1
$\zeta_{\min}$(Case 4) [%]	4.2	3.0	3.0	7.1

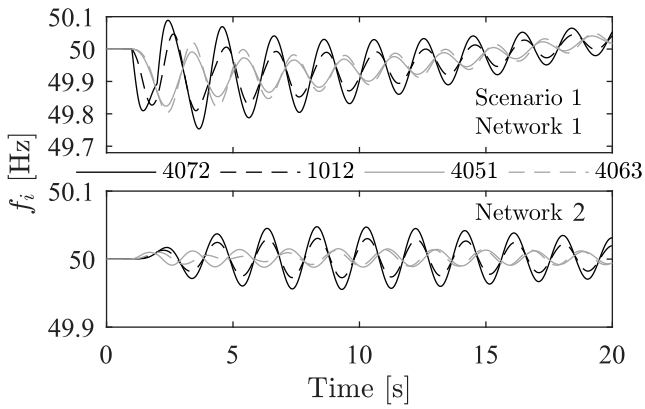

Figure 3.14: Scenario 1: Machine speeds at buses 4072 and 1012 in the northern areas and 4051 and 4063 in the southern areas following a 500 MW load disturbance at bus 4072 in Network 1.

Scenario 1) Load Disturbance, HVDC-Configuration Case 1, Controller K_1

A 500 MW load disturbance occur at the time interval $t = [1,2]$ s at bus 4072 in Network 1. As shown in Figure 3.14 the load disturbance reduces the initial machine speed at bus 4072 ensuing in a north–south interarea oscillation.

Scenario 2) Line Trip, HVDC-Configuration Case 2, Controller K_2

The transmission line between buses 4011 and 4021 is tripped at time $t = 1$ s. Since there is a large power transfer from the north to the south, the initial loss of transfer capacity causes machines in the north area to accelerate while the southern machines decelerate. As seen in Figure 3.15 a local mode within the north area is also excited by the disturbance. However, the local mode is well damped and after a while the response is dominated by the north–south interarea mode.

Resulting HVDC active power for the two scenarios is shown in Figure 3.16. HVDC active power modulation is shown to be effective in both scenarios. In agree-

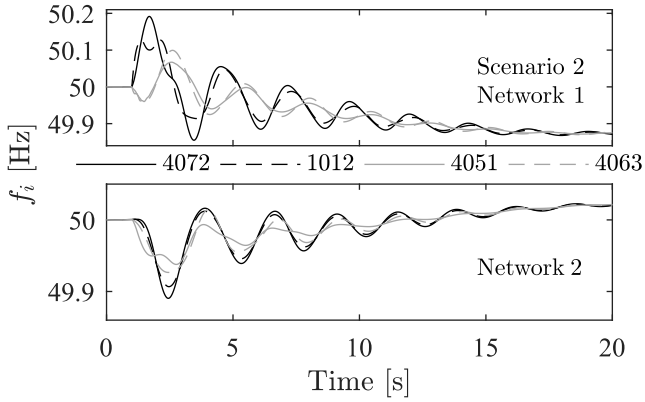

Figure 3.15: Scenario 2: Machine speeds at buses 4072 and 1012 in the northern areas and 4051 and 4063 in the southern areas following a line trip in the northern area of Network 1.

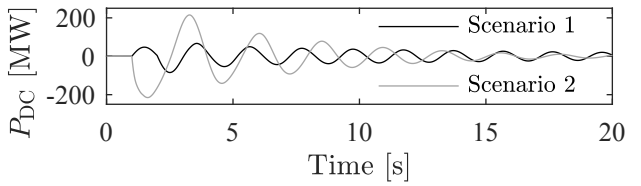

Figure 3.16: HVDC active power following the disturbance of the two scenarios in Figures 3.14 and 3.15.

ment with previous analysis it is also seen that for the line trip in Scenario 2 (where we consider the Case 2 network topology, with higher modal ratio) allows for a higher feedback gain and a higher POD improvement than Case 1.

3.6 Summary

Oscillatory stability has become an increasing concern in the modern power system. Stability of interarea modes often limits the transfer capacity over weak transmission corridors. In this chapter we have analyzed how active power modulation of HVDC transmission that interconnects two asynchronous ac networks can be used to stabilize a poorly damped interarea mode in each network. It was shown that the ratio between the modal frequencies is the sole factor determining the achievable nominal performance. The analytical results was verified by simulating on a simple test case as well as on a detailed model of two HVDC-interconnected 32-bus networks.

Chapter 4

Coordinated HVDC Control

In this chapter, coordination of multiple point-to-point high-voltage direct current (HVDC) lines interconnecting asynchronous ac systems is considered. Using one HVDC link, achievable performance are limited since control actions may excite modes of similar frequencies in the assisting network. However, with coordinated control of two or more HVDC links, the limitations can be circumvented. With decoupling control the system interactions can be avoided altogether. This chapter investigates conditions suitable for decoupling control. It is shown that decoupling between system modes can be achieved using a proportional controller. The control method is compared to decentralized and centralized optimal control. The best control method for different system topologies is investigated by looking on input usage and stability following dc link failure. The results are validated on a realistic model with two interconnected 32-bus networks.

One concern that arises when utilizing HVDC active power control for power oscillation damping (POD) is that interarea modes of the assisting network may be excited [20]. Since poorly damped interarea modes usually fall in the same frequency ranges [15], control methods should avoid unnecessary excitation of weekly damped modes. Interactions can be mitigated by incorporating energy storage from integrated wind power or large capacitor banks in the dc system [38, 39]. In this work, a solution that does not require dc energy storage is proposed. In [20] it was shown that through HVDC active power control, although propagating the disturbance to the assisting network, the overall POD can be improved in both of the HVDC-interconnected ac networks. In Chapter 3 it has been shown that the limiting performance factor for such a control strategy is the proximity of interarea modal frequencies between the two ac networks. A higher feedback gain improves POD of the two ac networks, but also moves the frequency of their interarea modes, and their eigenvalues, closer to each other thereby reducing controllability through modal interaction. With a higher system inertia, stronger control action is needed to improve POD, making this effect independent of system inertia.

With additional HVDC lines, the limitations imposed by modal interactions

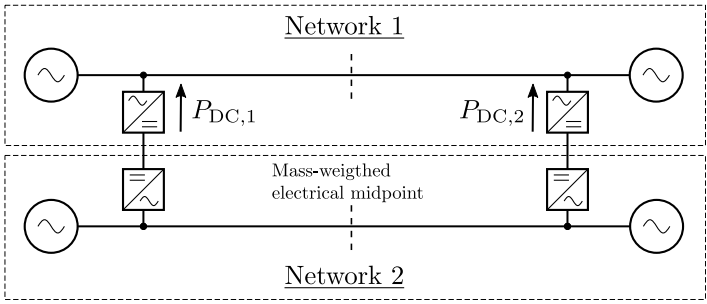

Figure 4.1: Two-sided HVDC-configuration between two asynchronous two-machine networks. Power oscillation damping of one network can be improved by controlling the two links in anti-phase, using the other ac network as a power sink.

can be circumvented. In [66] it was shown that by controlling two distant HVDC links (as seen in Figure 4.1) in anti-phase, the link resembles a long HVDC link interconnecting the two areas. Oscillation damping is then improved by injecting power between the two areas, using the asynchronous ac network two which the HVDC links is connected, as a power sink. Since multiple HVDC connections between asynchronous ac networks are common today, improvement of dynamical performance using coordinated control can be achieved without the need for any additional hardware installations.

The main contribution of this chapter is to show how the system topology affects multivariable interactions in HVDC-interconnected system where both ac networks has poorly damped interarea modes. A decentralized controlled method is compared to a decoupling control method. It is shown that decoupling control, avoiding the interaction between selected interarea modes all-together, can be achieved using a proportional controller. The decentralized and decoupling controllers are compared to a single-line equivalent where the links are controlled as one, as well as a centralized optimal controller. Suitability of the different control methods is analyzed with respect to network topology and sensitivity to dc link failures.

The remainder of the chapter is organized as follows. In Section 4.1 a generalized linear model representation of a power system with arbitrary many buses and HVDC links is presented. In Section 4.2 test systems with different HVDC-configurations are specified. In Section 4.3 some useful tools for analyzing multiple-input multiple-output systems are introduced. In Section 4.4 coordinated control methods are designed for the test cases of interest defined in Section 4.2. In Section 4.5 closed-loop stability properties of the control methods with respect to communication, measurement and actuator failure is discussed. In Section 4.6 it is shown how to implement decoupling control in a system with arbitrary number of states and input-output combinations. In Section 4.7 and Section 4.7 simulations on more detailed power system models are performed to verify analytical findings. Section 4.9 summaries the chapter.

4.1 Model of System with Multiple HVDC Links

With multiple HVDC links, the limitations imposed by modal interactions may be circumvented. To obtain insight into how additional controllable HVDC links may improve achievable system we first introduce a more general system description.

General Model of an HVDC-Interconnected System

The model of an ac network with arbitrary many machine and buses, linearized in the same manner as in Section 3.1, can be described as

$$\begin{bmatrix} I & 0 & 0 \\ 0 & M & 0 \\ 0 & 0 & 0 \end{bmatrix} \begin{bmatrix} \dot{\delta} \\ \dot{\omega} \\ \dot{\theta} \end{bmatrix} = \begin{bmatrix} 0 & I & 0 \\ -Y_{\delta\delta} & -D & -Y_{\delta\theta} \\ -Y_{\theta\delta} & 0 & -Y_{\theta\theta} \end{bmatrix} \begin{bmatrix} \delta \\ \omega \\ \theta \end{bmatrix} + \begin{bmatrix} 0 & 0 \\ I & 0 \\ 0 & I \end{bmatrix} \begin{bmatrix} P_\delta \\ P_\theta \end{bmatrix}$$

where 0 and I are zero and identity matrices of appropriate sizes, M and D are diagonal matrices containing machine inertia and damping constants on the diagonal. External input $P_\delta = P_m - P_{\text{load}}$ is the active power injected to the system from machine buses while P_θ are power injected at other buses e.g. from constant power loads or HVDC power injections. The linear approximation of the ac power flow is given by

$$\begin{bmatrix} P_\delta \\ P_\theta \end{bmatrix} = Y \begin{bmatrix} \delta \\ \theta \end{bmatrix} = \begin{bmatrix} Y_{\delta\delta} & Y_{\delta\theta} \\ Y_{\theta\delta} & Y_{\theta\theta} \end{bmatrix} \begin{bmatrix} \delta \\ \theta \end{bmatrix}$$

where Y is the susceptance matrix of the network while δ and θ are voltage phase angles at machine and dc buses respectively. The susceptance matrix Y is a Laplacian matrix, $Y_{\delta\delta}$ is diagonal, $Y_{\theta\theta}$ is assumed to be invertible, and $Y_{\delta\theta} = Y_{\theta\delta}^T$.

Machine rotor dynamics, is given by the swing equation (3.1)

$$\dot{\omega} = P_m - P_{\text{load}} - P_e - D\omega.$$

Using Kroon reduction [5, 79], P_e can be reduced to a function of state variables δ and active power injection P_θ at the dc buses:

$$P_e = Y_\delta \delta + Y_\theta P_\theta$$

where $Y_\delta = Y_{\delta\delta} - Y_{\delta\theta} Y_{\theta\theta}^{-1} Y_{\theta\delta}$ and $Y_\theta = Y_{\delta\theta} Y_{\theta\theta}^{-1}$. Note that both Y and Y_δ are Laplacian matrices.

Assuming that there are no loads at the dc buses we have $P_\theta = P_{\text{DC}}$. The dynamics of the power system, linearized around an initial operating point, is then given by

$$\begin{bmatrix} \dot{\delta} \\ \dot{\omega} \end{bmatrix} = \begin{bmatrix} 0 & I \\ -M^{-1}Y_\delta & -M^{-1}D \end{bmatrix} \begin{bmatrix} \delta \\ \omega \end{bmatrix} + \begin{bmatrix} 0 & 0 \\ M^{-1} & M^{-1}Y_\theta \end{bmatrix} \begin{bmatrix} P_m - P_{\text{load}} \\ P_{\text{DC}} \end{bmatrix}.$$

Similarly, voltage phase angle or frequency measurements at non generator buses is given by $Y_\theta^T \delta$ and $Y_\theta^T \omega$ respectively [80].

Two-Machine Networks Interconnected by Two HVDC Lines

To simplify the analysis we make the following assumption:

Assumption 4.1 (Damping Proportional to Inertia) The machine damping is evenly distributed and proportional to the machine inertia constant (which in turn is proportional to rated power)

$$D_{ij} = D_i \frac{M_{ij}}{M_{\Sigma,i}}$$

such that the machines become scaled versions of each other.

Remark 4.1 Since the mode (corresponding to eigenvalue λ) is assumed poorly damped ($|\mathrm{Re}(\lambda)| \ll |\lambda|$) Assumption 4.1 has little effect on model accuracy. This is further discussed in the Section 3.2.

As shown in Section 3.2, the swing mode of a two-machine system can then be represented using the relative phase and machine speeds $\Delta\delta_i = \delta_{i1} - \delta_{i2}$ and $\Delta\omega_i = \omega_{i1} - \omega_{i2}$. The linearized dynamics of the system is given by

$$\begin{bmatrix} \Delta\dot{\delta}_i \\ \Delta\dot{\omega}_i \end{bmatrix} = \underbrace{\begin{bmatrix} 0 & 1 \\ \frac{-V_i^2 M_{\Sigma,i}}{M_{i1}M_{i2}X_{\Sigma,i}} & \frac{-D_i}{M_{\Sigma,i}} \end{bmatrix}}_{A_i} \begin{bmatrix} \Delta\delta_i \\ \Delta\omega_i \end{bmatrix} + \underbrace{\begin{bmatrix} 0 & 0 \\ b_{i1} & b_{i2} \end{bmatrix}}_{B_i} \underbrace{\begin{bmatrix} P_{\mathrm{DC1}} \\ P_{\mathrm{DC2}} \end{bmatrix}}_{u}$$

where $X_{\Sigma,i}$ is the series reactance between the machine buses in Network i, A_i, and B_i is the system state and input matrix respectively. The input u are the controlled active power injections of the two dc links. As an example, the input matrix

$$B_1 = \begin{bmatrix} 0 & 0 \\ \frac{M_{12}(X_{12}+X_{13})-M_{11}X_{11}}{M_{11}M_{12}X_{\Sigma,1}} & \frac{M_{12}X_{12}-M_{11}(X_{11}+X_{13})}{M_{11}M_{12}X_{\Sigma,1}} \end{bmatrix} \tag{4.1}$$

is obtained for Network 1 in Figure 4.2.

Let $y_i = \Delta\omega_i$ be the measured output signal. The transfer function $G_i(s)$ from u to y_i then becomes

$$G_i = \begin{bmatrix} 0 & 1 \end{bmatrix} (sI - A_i)^{-1} B_i = \frac{s}{s^2 + s2\gamma_i + \Omega_i^2} \begin{bmatrix} b_{i1} & b_{i2} \end{bmatrix}$$

where

$$\Omega_i = \sqrt{\frac{V_i^2(M_{\Sigma,i})}{M_{i1}M_{i2}X_{\Sigma,i}}}$$

is the undamped frequency of Network i and

$$\gamma_i = \frac{1}{2}\frac{D_i}{M_{\Sigma,i}}.$$

The HVDC-interconnected system to be controlled, is thus represented by the transfer function

$$G = \begin{bmatrix} G_1 \\ -G_2 \end{bmatrix} = \begin{bmatrix} \frac{s}{s^2+s2\gamma_1+\Omega_1^2} & 0 \\ 0 & \frac{s}{s^2+s2\gamma_2+\Omega_2^2} \end{bmatrix} \begin{bmatrix} b_{11} & b_{12} \\ -b_{21} & -b_{22} \end{bmatrix}. \tag{4.2}$$

4.2 Model Specifications

The mutual placement of the HVDC terminals determine the interaction of the two ac networks due to HVDC active power modulation. Thus it will play a big role in POD control design. If we consider the damping of one dominant interarea mode in each of the asynchronous ac networks there are essentially three relevant configurations possible using two HVDC links.

Two-Sided HVDC-Configuration

In a *two-sided* HVDC-configuration the HVDC terminals are located on each side of the mass-weighted electrical midpoint in each system, as seen in Figure 4.1. The mass-weighted electrical midpoint is the location where the interarea mode is uncontrollable using HVDC active power injection. At this location, the corresponding element in the input matrix (4.1) is zero.

One-Sided HVDC-Configuration

We use the term *one-sided* to describe a configuration where both HVDC terminals are located on the same side of the mass-weighted electrical midpoint in each system, as seen in Figure 4.2.

Uneven HVDC-Configuration

The term *uneven* will be used to describe the HVDC-configuration seen in Figure 4.3 where the HVDC terminals are located on either side of the mass-weighted electrical midpoint in one of the ac networks, and on the same side in the other network.

A special case of the uneven configuration is when one of the dc terminals is located directly in the mass-weighted electrical midpoint. It is quite intuitive that interaction between oscillatory modes can be avoided when providing POD in such a setup since the centrally placed link will only affect one of the networks. In the following sections we will investigate this further. For this, we first specify three models with the considered HVDC-configurations.

Model Parameters

To study the effect of multivariable interactions on the HVDC-interconnected system we consider two ac networks, each represented by a two-machine model, interconnected with two point-to-point HVDC lines as seen in Figures 4.1–4.3. The

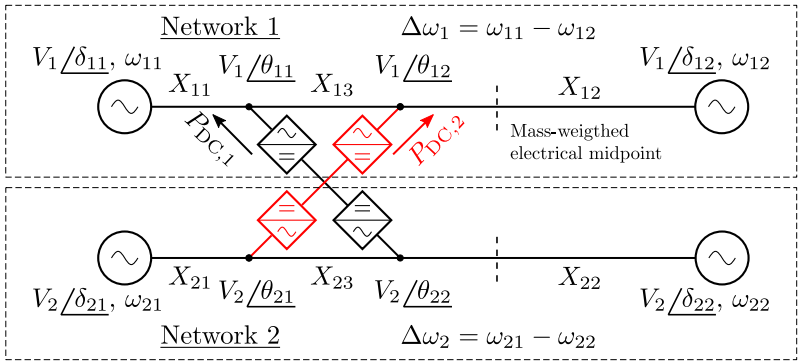

Figure 4.2: One-sided HVDC-configuration between two asynchronous two-machine networks.

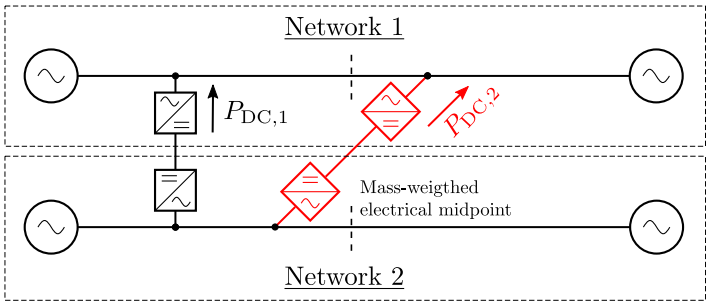

Figure 4.3: Uneven HVDC-configuration between two asynchronous two-machine networks.

Table 4.1: Electrical positions of HVDC terminals $ih \in \{1, 2\}$ for three different HVDC-configurations.

	Network 1		Network 2	
Configuration	$X_{B,11}$	$X_{B,12}$	$X_{B,21}$	$X_{B,22}$
Two-Sided	0.6	-0.4	0.4	-0.6
One-Sided	0.6	0.4	0.4	0.6
Uneven	0.6	-0.4	0.6	0.4

(mass-weighted) electrical position[1] $X_{B,ih} \in [-1, 1]$ for the three considered configurations is shown in Table 4.1. To isolate the effect of HVDC-configuration we considered the two networks to be identical in all scenarios. As shown in Chapter 3 the system would therefore not be controllable using only one dc link. For all three configurations, model dynamics are given by (4.2) with

[1] Calculated according to (4.1), but leaving out machine inertia constants.

- no inherent damping, $D_1 = D_2 = 0$;
- undamped modal frequencies $\Omega_1 = \Omega_2 = 0.5\,\text{Hz}$;
- constant voltage $V_1 = V_2 = 1\,\text{p.u.}$ assumed at all buses;
- identical machine inertia constants $M_{ij} = 2HS_r/\omega_n$. For each machine: rated power $S_r = 4\,\text{p.u.}$, inertia time constant $H = 6\,\text{s}$, and $\omega_n = 2\pi f_n$ where $f_n = 50\,\text{Hz}$ is the nominal system frequency. Since the networks are symmetrical, the mass-weighted electrical midpoint is the same as the electrical midpoint given by $X_{B,ih}$.

Transfer Functions

The transfer functions (4.2) of the three systems specified in Table 4.1 becomes

$$G_{\text{two-sided}} = \begin{bmatrix} \frac{s}{s^2+\pi^2} & 0 \\ 0 & \frac{s}{s^2+\pi^2} \end{bmatrix} \begin{bmatrix} 3.9 & -2.6 \\ -2.6 & 3.9 \end{bmatrix}, \tag{4.3}$$

$$G_{\text{one-sided}} = \begin{bmatrix} \frac{s}{s^2+\pi^2} & 0 \\ 0 & \frac{s}{s^2+\pi^2} \end{bmatrix} \begin{bmatrix} 3.9 & 2.6 \\ -2.6 & -3.9 \end{bmatrix}, \tag{4.4}$$

and

$$G_{\text{uneven}} = \begin{bmatrix} \frac{s}{s^2+\pi^2} & 0 \\ 0 & \frac{s}{s^2+\pi^2} \end{bmatrix} \begin{bmatrix} 3.9 & -2.6 \\ -3.9 & -2.6 \end{bmatrix}. \tag{4.5}$$

The dynamics of the two ac systems are given by the first (diagonal) matrix while the second (input) matrix describe how the corresponding input u_h affect each output y_i.

For the two- and one-sided configuration (4.3)–(4.4) the input have been ordered so that the plant, G, is as diagonal as possible. That is, input u_1 will have most effect on y_1 while u_2 have most effect on y_2. For the uneven configuration (4.5) there is no clear way to order the inputs.

Since the off-diagonal entries of the input matrices are non-zero, each input will affect both outputs. That is, there is *interaction* between the inputs and outputs. How these multivariable interactions affect the potential benefit of adding additional HVDC lines will be studied in the following sections.

4.3 Analysis

Some of the difficulties in mimo system control are an increased sensitivity to uncertainties due to directionality and interactions that may occur between the inputs and outputs. Here we introduce two useful measures for quantifying the degree of directionality and the level of interactions.

Definition 4.1 (Condition Number [76]) The condition number of a matrix G is the ratio between the maximum and minimum singular values

$$\kappa(G) := \frac{\bar{\sigma}(G)}{\underline{\sigma}(G)}.$$

A matrix with a large condition number is said to be *ill-conditioned*. If G is a transfer function then the condition number may be frequency dependent.

If the condition number is small, then problems with multivariable interactions are not likely to be serious. If the condition number are large however this may indicate a control problem. The large condition number may also be the result of input and output scalings. To avoid this, we will instead use the minimized condition number over all possible input and output scalings W_1 and W_2 [76]

$$\kappa^*(G) = \min_{W_1, W_2} \kappa(W_1 G W_2).$$

Another useful measure (independent of input and output scaling) is the RGA.

Definition 4.2 (Relative Gain Array (RGA) [76]) The RGA of a non-singular square matrix G is defined as the Hadamard product (element wise product)

$$\mathrm{RGA}(G) := G \times (G^{-1})^T.$$

The RGA matrix indicates the coupling between inputs and outputs. One property of the RGA is that rows and columns all sum up to one. Input-output combination should be selected so that the corresponding RGA element is as close to 1 as possible [76].

Analysis of HVDC-Interconnected Systems

The (minimized) condition number and RGA of the three systems specified in Section. 4.2 are shown in Table. 4.2. Since the dynamics of the systems are given by a diagonal matrix (4.3)–(4.5), the condition number and RGA are the same for all frequencies.

Table 4.2: Condition number and RGA for the HVDC-interconnected systems (4.3)–(4.5).

	Two-Sided	One-Sided	Uneven
κ^*	5	5	1
RGA	$\begin{bmatrix} 1.8 & -0.8 \\ -0.8 & 1.8 \end{bmatrix}$	$\begin{bmatrix} 1.8 & -0.8 \\ -0.8 & 1.8 \end{bmatrix}$	$\begin{bmatrix} 0.5 & 0.5 \\ 0.5 & 0.5 \end{bmatrix}$

We see that the condition number and RGA is identical for the one- and two-sided systems. This indicates similar issues with respect to multivariable interactions. Because of this we only consider the one-sided configuration in the following control design and simulation study.

In addition we find that the minimized condition number $\kappa^*(G_{\text{uneven}}) = 1$. This indicate that directionality does not limit the achievable performance for the uneven configuration.

4.4 Coordinated Control Design

In this Section we study the HVDC-interconnected system defined in Section 4.2. The goal is to see how multivariable interactions and directionality affect system performance when trying to improve POD in both networks. As shown in Section 4.3 the one- and two-sided HVDC-configurations have the same problem with directionality. We therefore choose to leave out the two-sided configuration.

The one-sided configuration is compared to the uneven configuration which according to Section 4.3 should have no issues with multivariable interactions. To see the implications of this we design four different multivariable controllers designed to improve POD in both of the interconnected ac networks. We then present the simulated system response to a 0.4 p.u. load step at machine-bus 1 in Network 1[2].

Single-Line Control

To counteract ac power flows and improve POD, the dc active power is controlled uniformly for the two HVDC links

$$u_1 = u_2 = \begin{bmatrix} -k & k \end{bmatrix} y$$

were we let $k = 1\,\text{Hz}^{-1}$. As shown in Chapter 3, the achievable POD performance will be limited by modal interactions. Increasing the gain will cause system eigenvalues corresponding to the two interarea modes to approach each other (see Figure 3.8). The controllability of the interarea modes are thereby lost. In this case, since $\Omega_1 = \Omega_2$ the interarea modes are uncontrollable no matter the feedback gain. The only achievable benefit is sharing of the disturbance between the two networks as can be seen in Figure 4.4. In this case, performance can be improved using multivariable control methods.

Decentralized Control

The simplest multivariable control approach is to use a diagonal block controller K where each input is paired with one suitable output measurement. Assuming that each actuator is controlled independently using local measurements, this control method can be called a decentralized. Decentralized control works well if the condition number of G is small and the controllability from chosen input-output pairings are high relative to the other input-output combinations [76]. For the the

[2]System is modeled using (3.1)–(3.2) to incorporate nonlinear power flow.

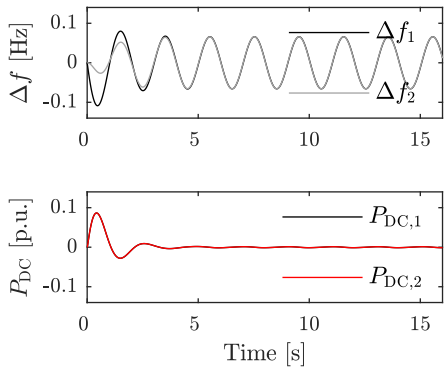

Figure 4.4: Single-line control under one-sided HVDC-configuration following a 0.4 p.u. load step at machine-bus 1 in Network 1.

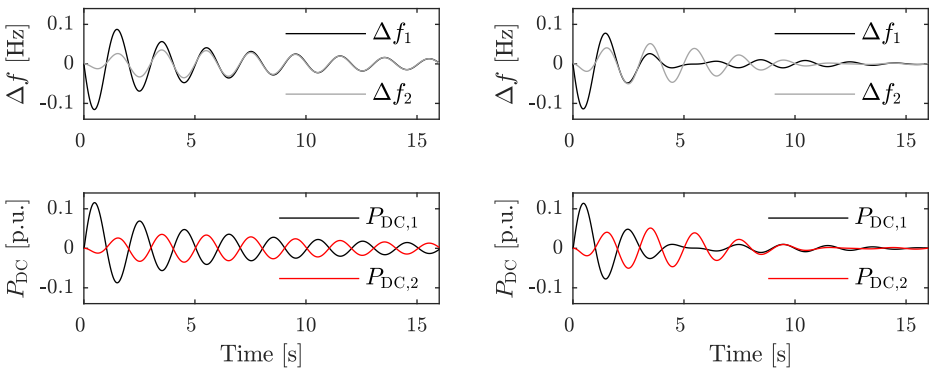

(a) One-sided HVDC-configuration (b) Uneven HVDC-configuration

Figure 4.5: Decentralized control. System response following a 0.4 p.u. load step at machine-bus 1 in Network 1.

one-sided (4.4) and uneven (4.5) HVDC-configurations, satisfactory decentralized control is realized with the diagonal controller

$$u = \begin{bmatrix} -k & 0 \\ 0 & \operatorname{sgn}(b_{22})k \end{bmatrix} y, \ \operatorname{sgn}(b_{11}) := 1. \tag{4.6}$$

In Figure 4.5 it is seen that the decentralized control method manages to circumvent the limitations of the single-line control. For the one-sided configuration this can be expected by looking on the RGA in Table 4.2. For the uneven configuration any input-output pairing is suitable. We also see that the disturbance is attenuated

faster with less input usage. This can be expected since $\kappa(G_{\text{uneven}}) > \kappa(G_{\text{one-sided}})$ indicates that the uneven configuration has less issues with multivariable interactions.

Since a decentralized control method makes no attempt to cancel interactions in G, resulting performance may be poor if these are considerable. This can be improved by using decoupling control where we attempt to cancel out off-diagonal input-output interactions.

Decoupling Control

By shaping $\tilde{G} = GW$ to be a diagonal system, independent control of each input-output combination can be realized using a diagonal controller. Each control-loop can be tuned independently using single-input single-output methods for the corresponding input-output path [76]. The pre-compensator W can be chosen in many ways[3]. Here we choose

$$W = \begin{bmatrix} 1 & \frac{-b_{12}}{b_{11}} \\ \frac{-b_{21}}{b_{22}} & 1 \end{bmatrix} \tag{4.7}$$

and thus

$$\tilde{G} = \begin{bmatrix} \frac{s}{s^2+\Omega_1^2} & 0 \\ 0 & \frac{s}{s^2+\Omega_2^2} \end{bmatrix} \begin{bmatrix} b_{11} - \frac{b_{12}b_{21}}{b_{22}} & 0 \\ 0 & -\left(b_{22} - \frac{b_{12}b_{21}}{b_{11}}\right) \end{bmatrix}.$$

Disturbance rejection, comparable to the decentralized controller (4.6), is achieved using

$$u = W \begin{bmatrix} -k & 0 \\ 0 & \operatorname{sgn}(b_{22})k \end{bmatrix} y = Ky, \ \operatorname{sgn}(b_{11}) = 1. \tag{4.8}$$

With a decoupling controller, the excitation of the interarea mode in the assisting system is avoided as seen in Figure 4.6. The downside of the decoupling control method may be an increased input usage since one link is controlled to counteract the effect on the assisting network. If G is ill-conditioned, no obvious input-output combination exist to control the multivariable system. This makes it unsuitable for both decoupling and decentralized control.

Remark 4.2 Changing ac power flows, system inertia or the connection/disconnection of ac transmission lines may affect the decoupling performance of the controller since the (mass-weighted) electrical midpoint or the HVDC terminals position relative to each other may change. However, such uncertainties are unlikely to be severe enough to cause instability if the system is eligible for decoupling control in the first place.

[3] Choosing $W = G^{-1}$ would result in $\tilde{G} = I$. To make the controller proper however, additional poles would have to be added to K.

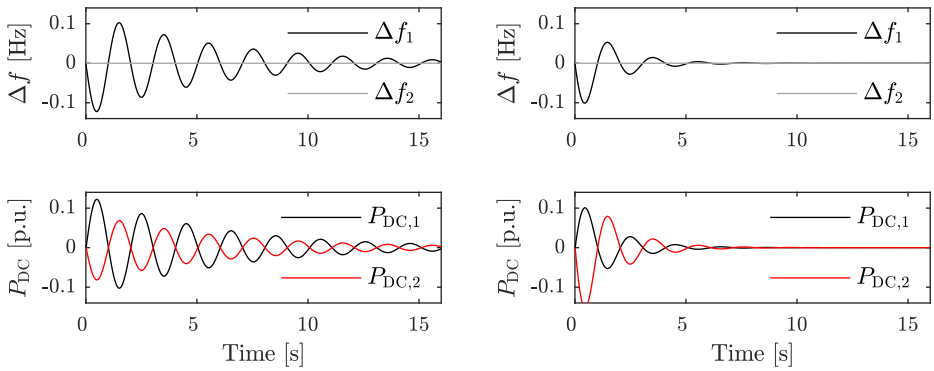

(a) One-sided HVDC-configuration

(b) Uneven HVDC-configuration

Figure 4.6: Decoupling control. System response following a 0.4 p.u. load step at machine-bus 1 in Network 1.

Decoupling using a constant matrix is possible since we represent the interarea mode using individual state variables and assume that these are available from measurement. Basically, we are decoupling the system at the frequency of the interarea mode. In Section 4.6 we generalize this control method to a higher order system.

$\mathcal{H}_2$ Optimal Control

Optimization based methods have been excessively studied for multivariable feedback design in power systems [4, 7]. Such design methods offer a structured way to synthesize multivariable feedback controllers which can potentially yield an better system-wide performance than a decentralized control design. Here we will consider an $\mathcal{H}_2$ optimal controller. Since $\mathcal{H}_2$ weights the disturbances over all channels and frequencies, a controller yielding satisfactory performance can usually be achieved without to much tuning.

The $\mathcal{H}_2$ controller (essentially a linear-quadratic-Gaussian controller [76]) is obtained as the controller K that minimizes the $\mathcal{H}_2$ norm of the closed-loop system shown in Figure 4.7, from input variables ΔP and d_y to performance variables z_y and z_u. For a dynamical response similar to that of the decentralized and decoupled controller, the controller is tuned with

- external inputs $|\Delta P_{ij}| \leq 0.4\,\text{p.u.}$ and $|d_{yi}| \leq 5\%,\ i,j \in \{1,2\}$ over all frequencies;
- performance weights $W_z = 1$ and $W_u = 5$.

Comparing Figures 4.5a and 4.8a we see that $\mathcal{H}_2$ synthesis yields a controller similar to that of the decentralized controller (4.6). This is because the decoupling

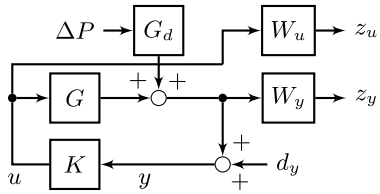

Figure 4.7: The closed-loop feedback system used for $\mathcal{H}_2$ synthesis. Block G_d represents the transfer function from machine bus disturbances to relative machine speeds.

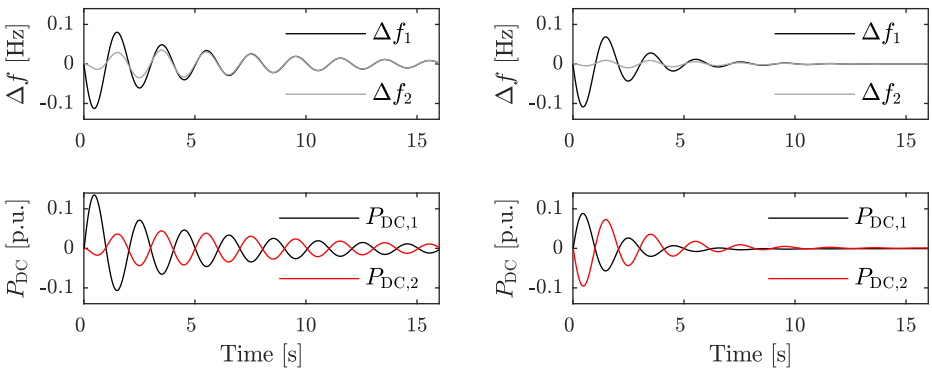

(a) One-sided HVDC-configuration

(b) Uneven HVDC-configuration

Figure 4.8: $\mathcal{H}_2$ optimal control. System response following a 0.4 p.u. load step at machine-bus 1 in Network 1.

controller in the one-sided configuration decouples the system by controlling one dc link in the wrong direction. Since this decoupling control action counteracts disturbance attenuation this will not be the $\mathcal{H}_2$ optimal control method.

For the uneven HVDC-configuration we find that the $\mathcal{H}_2$ optimal controller resembles a decoupling controller as seen in Figures 4.6b and 4.8b. This is because disturbance attenuation and decoupling requires the same dc power direction as indicated by the RGA in Table 4.2. Similarly, if the system is ill-conditioned, the $\mathcal{H}_2$ optimal controller will resemble the single-line controller since cancellation of multivariable interactions will require too much input usage.

4.5 Closed-Loop Stability Properties: HVDC Link Failure

With single-line control, a disconnection will lead to a weaker control action. In the case of decentralized control, disconnection of one HVDC link will leave one of the networks outside the feedback-loop altogether. Neither of the mentioned contingencies will destabilize the system so the $N-1$ criterion (with respect to the

HVDC control) is fulfilled without additional safety actions. With the decoupling controller however, it can be shown (see Appendix B.1) that if

$$-\text{sgn}(b_{22})b_{21}b_{12} > 0,\ \text{sgn}(b_{11}) \text{ and } \text{sgn}(k) := 1 \tag{4.9}$$

is violated, the system will be destabilized by the HVDC controller following a dc link failure. Equation (4.9) thus represent an $N-1$ stability criterion with respect to dc link (or control actuator) failure. If the inherent damping is weak, then instability is likely to ensue if no safety measures are taken.

The $N-1$ stability criterion (4.9) can also be assessed by studying the RGA. The RGA of a two-by-two matrix is given by [76]

$$\text{RGA} = \begin{bmatrix} q & 1-q \\ 1-q & q \end{bmatrix}$$

where for (4.2)

$$q = \frac{1}{1 - \frac{b_{12}b_{21}}{b_{11}b_{22}}}.$$

Assuming that input and outputs are ordered so that $b_{11}, b_{22} \neq 0$, then if (4.9) holds, $0 < q \leq 1$ and all RGA elements are non-negative.

Measurement Failure

If the system experiencing measurement failure is open-loop stable then instability does not ensue.

Communication Failure

If a measurement signal fails to reach one of the dc link controllers and (4.9) is violated, then one link will provide negative feedback while the other link provides positive feedback. If the communication to the negative feedback link fails then the system will be destabilized.

4.6 Decoupling Control in Higher Order Systems

The benefit of a decoupling POD controller is that excitation of poorly damped modes in the assisting network can be avoided. The method proposed in Section 4.4 achieved this using a proportional controller. In this section we will study how this can be extended to a larger system.

Consider a linear time invariant (LTI) system

$$G = C(sI - A)^{-1}B \overset{s}{=} \left[\begin{array}{c|c} A & B \\ \hline C & 0 \end{array}\right].$$

rewritten on modal form (see Appendix A.3)

$$G_v \overset{s}{=} \left[\begin{array}{c|c} \Lambda & V_L B \\ \hline C_v & 0 \end{array}\right] = \left[\begin{array}{c|c} \Lambda & B_\Lambda \\ \hline C_v & 0 \end{array}\right] \tag{4.10}$$

where

- $\Lambda = \text{diag}\{\lambda_1, \ldots, \lambda_N\}$ has eigenvalues of A (poles of G) on its diagonal;
- V_L is a matrix with rows consisting of left eigenvectors of A s.t. $V_L A = \Lambda V_L$;
- v is the set of modes $\xi_v = V_v^L x$ that we are interested to control.

Since Λ is diagonal, system dynamics are decoupled. The poles, and therefore the stability of each mode, can be controlled individually given that a good estimate of ξ_v is used as feedback signal [81].

If we design W so that $V_v^L B W = B_v^\Lambda W$ is diagonal, then λ_n, $n \in v$ can be stabilized without exciting the modes ξ_m, $m \in v$, $m \neq n$. If the transfer function from $|v|$ inputs to the $|v|$ outputs in G_v is invertible, then the system can be decoupled using a constant pre-compensator matrix $W \in \mathbb{C}^{|v|\times|v|}$.

Complex modal states appear in complex conjugate pairs s.t. $\xi_{n+1} = \bar{\xi}_n$. If $y = \text{Re}(V_v^L)V_R^{-1}\xi = \text{Re}(V_v^L)x$ is chosen as feedback signal, only one element in each complex conjugated pairs are needed in v. This can be seen by looking on the real Jordan form of the closed-loop system (see Appendix B.2).

Assumption 4.2 (Phase Condition) Assume that the inputs affect each mode ξ_n with the same phase. Then

$$B_v^\Lambda = \Phi \text{Re}(V_v^L) B$$

where

$$\Phi = \text{diag}\left(e^{j\varphi_1}, \ldots, e^{j\varphi_{|v|}}\right).$$

The selected modes ξ_v can then decoupled with the pre-compensator

$$W = (\text{Re}(V_v^L)B)^{-1} \in \mathbb{R}^{|v|\times|v|}. \tag{4.11}$$

Remark 4.3 The eigenvectors are not uniquely defined. When designing (4.11) its good to align V_v^L so that condition number $\kappa(\text{Re}(V_v^L)B)$ is small.

A good approach is to set $\angle V_v^L(\bar{\omega}_v) = 0$ or π. The notation $V_v^L(\bar{\omega}_v)$ means that we consider the indexes of the left eigenvectors corresponding to the states representing rotor speeds of the machines with highest participation in each of the modes in v. The mode shape, as given by rotor speeds, will then be close to the real axis as seen in Figures 4.9b and 4.15.

The proposed decoupling controller is demonstrated in two simulations examples. In Section 4.7 we consider the interconnection of two three-machine networks. This configuration lets us see how the decoupling control targets specific modes in the system. In Section 4.8 we study the $N-1$ stability criterion (4.9) on two HVDC-interconnected 32-bus networks.

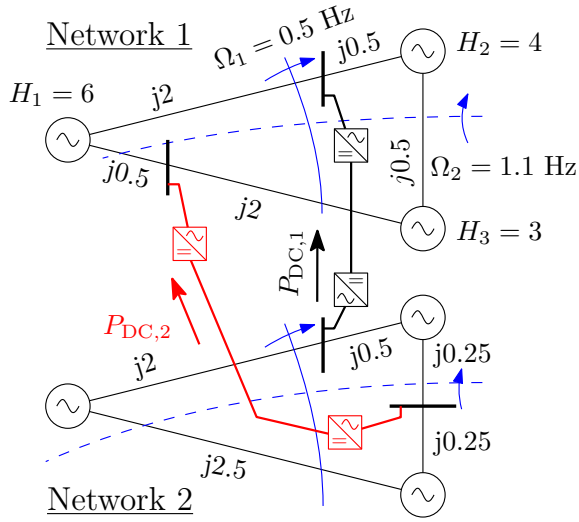

(a) HVDC-interonected system.

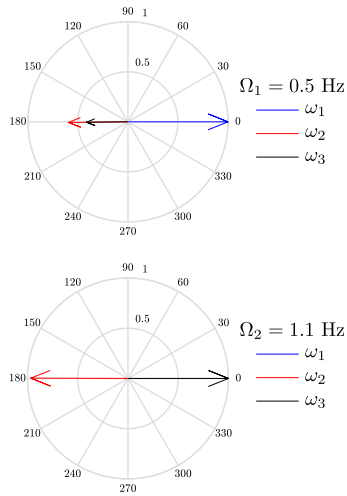

(b) Mode shapes of interarea mode Ω_1 and local mode Ω_2 in each three-machine network.

Figure 4.9: Two identical three-machine networks interconnected by two HVDC links. Line impedances shows electrical position of dc buses in each network.

4.7 Simulation Study: Two Three-Machine Networks

To illustrate the selectivity of the decoupling method, we consider the interconnection of two identical ac networks as shown in Figure4.9a. Each of the networks have an interarea mode Ω_1 at 0.5 Hz and a faster *local* mode Ω_2 at 1.1 Hz. The decoupling controller (designed according to Section 4.6) are then compared to a centralized optimal controller.

Model

The linearized system dynamics (as described in Section 4.1) are given by

$$\begin{bmatrix} \dot{\delta} \\ \dot{\omega} \end{bmatrix} = \underbrace{\begin{bmatrix} 0 & I \\ -M^{-1}Y_\delta & -M^{-1}D(s) \end{bmatrix}}_{A} \begin{bmatrix} \delta \\ \omega \end{bmatrix} + \underbrace{\begin{bmatrix} 0 \\ M^{-1}Y_\theta \end{bmatrix}}_{B} P_{\mathrm{DC}}$$

where:

- Matrix M is diagonal with the machine inertia constants $2H_iS_r/\omega_n$, $i \in \{1,\dots,6\}$ on its diagonal. The machine inertia time constants H_i are shown Figure 4.9a. Rated power of each machine $S_r = 4\,\mathrm{p.u.}$, $\omega_n = 2\pi f_n$, and $f_n = 50\,\mathrm{Hz}$.

- Mechanical input power is affected both by a proportional damping constant as well as a first order governor (3.43). Diagonal elements in $D(s)$ are given by the transfer function

$$D_i(s) = \frac{M_i}{M_\Sigma}\left(2 + \frac{25}{s4+1}\right)\frac{1}{\omega_n}$$

  where M_Σ is the total inertia in each respective network. The machines are thereby scaled versions of each-other and Assumption 4.1 holds.

- Using Kroon reduction [79] the network Laplacian matrix and input matrix are

$$Y_\delta = \begin{bmatrix} 0.8 & -0.4 & -0.4 & 0 & 0 & 0 \\ -0.4 & 2.4 & -2 & 0 & 0 & 0 \\ -0.4 & -2 & 2.4 & 0 & 0 & 0 \\ 0 & 0 & 0 & 0.8 & -0.4 & -0.4 \\ 0 & 0 & 0 & -0.4 & 2.4 & -2 \\ 0 & 0 & 0 & -0.4 & -2 & 2.4 \end{bmatrix}, \text{ and } Y_\theta = \begin{bmatrix} 0.2 & 0.8 \\ 0.8 & 0 \\ 0 & 0.2 \\ -0.2 & 0 \\ -0.8 & -0.5 \\ 0 & -0.5 \end{bmatrix}.$$

Goal

Design a multivariable controller that targets the 0.5 Hz interarea mode in each ac network. The controller should decouple the two modes to avoid exciting the 0.5 Hz mode in the assisting network.

Decoupling Control Design

Let the two eigenvalues (one in each complex conjugated pair) be denoted λ_v where v is the indexes of the consider eigenvalues. Let the corresponding left eigenvectors be given by V_v^L. We have that

$$\angle(V_v^L B) = \begin{bmatrix} -\pi & 0 \\ 0 & 0 \end{bmatrix}$$

thus Assumption 4.2 holds and adequate decoupling should be achievable with a constant pre-compensator.

With $\mathcal{V}_v^L = \mathrm{Re}(V_v^L)$ we have that

$$B_v^\Lambda = \mathcal{V}_v^L B = \begin{bmatrix} -1.5 & 1.8 \\ 1.5 & 2.6 \end{bmatrix}$$

and

$$RGA(G_v) = B_v^\Lambda \times \left((B_v^\Lambda)^{-1}\right)^T = \begin{bmatrix} 0.6 & 0.4 \\ 0.4 & 0.6 \end{bmatrix} \tag{4.12}$$

thus we see that the $N-1$ stability criterion (4.9) is fulfilled and the system should be suitable for decoupling control.

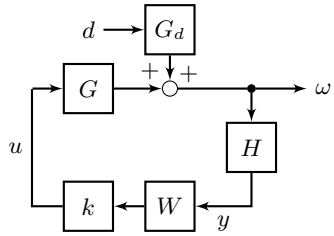

Figure 4.10: Closed-loop system with decoupling POD control.

The decoupling matrix (with columns scaled to have magnitude one on diagonal) becomes

$$W = \left(B_v^{\Lambda}\right)^{-1} \overset{\text{scale}}{=} \begin{bmatrix} 1 & -1.2 \\ -0.6 & -1 \end{bmatrix}.$$

In practice, $z_v = \mathcal{V}_v^L x$ is not available and has to be estimated. Here we assume that machine speed measurements are available and base the observer on the corresponding elements in $\mathcal{V}_v^L$[4]. To have a feedback signal that is zero in steady state we scale the output matrix as in (3.48). Thus the output is given by

$$y = H\omega = \underbrace{\begin{bmatrix} 1 & -0.6 & -0.4 & 0 & 0 & 0 \\ 0 & 0 & 0 & 1 & -0.6 & -0.4 \end{bmatrix}}_{H} \omega.$$

The resulting closed-loop system with

$$u = kWH\omega \tag{4.13}$$

can be seen in in Figure 4.10 where we have added an external input d acting on the system through G_d. For reasonable input usage, we let $k = 1/5\,\mathrm{Hz}^{-1}$.

Remark 4.4 In Chapter 3 we designed a controller considering only one link and found that optimal feedback gain is limited by modal interaction. Here, arbitrary high POD can be achieved since the multivariable control circumvents these limitations. This might not be desirable however since this comes at a higher input cost, increased interaction with other modes, and an increased sensitivity to model error. If the eigenvectors are incorrectly estimated, the feedback will affect other eigenvalues and which might destabilize the system. Therefore it is good practice to keep feedback gain as low as possible.

$\mathcal{H}_2$ Optimal Control Design

As shown in Section 4.4 similar results can easily be obtain with a $\mathcal{H}_2$ optimal control design. Here we consider the $\mathcal{H}_2$ controller K that minimizes the closed-loop system shown in Figure 4.11, where

[4]See the mode shape of interarea mode Ω_1 in Figure 4.9b.

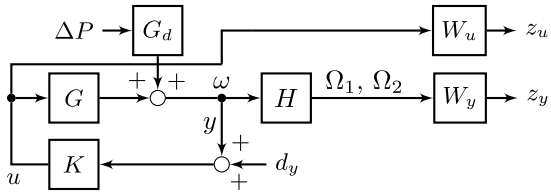

Figure 4.11: The closed-loop feedback system used for $\mathcal{H}_2$ synthesis. Block G_d represents the transfer function from machine bus disturbances to relative machine speeds. Block H gives the mode shapes (Figure 4.9b) of the interarea and local modes in each network.

- load disturbances at all machine-buses $|\Delta P_i| \leq 0.4\,\text{p.u.}$;
- measurement noise $|d_{yi}| \leq 5\,\%$

are the considered external inputs. To target the interarea mode, we choose Ω_1 from each network as a performance variable. Since we also have observability and controllability of the local modes we add Ω_2 as a performance variable. To get a POD performance similar to (4.13) we weight the performance variables by $W_y = 1$ and input usage $W_u = 2.5\frac{s+\pi}{s}$. The integrator is added to avoid steady state input usage. Resulting K is reduced to 10^{th} order[5] using balanced residualization [76].

Simulation Results

The considered scenario is a 0.4 p.u. load increase at machine-bus 1 in Network 1. In Figure 4.12 the system response with no HVDC control is shown. The load step causes a frequency drop in Network 1 and also triggers the interarea mode Ω_1 at 0.5 Hz as seen in Figure 4.12b. The local mode Ω_2 is fairly unaffected by the load disturbance.

We now add the decoupling POD controller (4.13) and consider the same disturbance scenario. As seen in Figure 4.13 the control method greatly improves the damping of Ω_1 in Network 1 without exciting the corresponding interarea mode in Network 2. However, since only decoupling between the interarea modes is implemented, other modes may be affected. For example, we see that the control action excites the local mode Ω_2 in both networks.

In Figure 4.14 the same disturbance scenario is simulated using the $\mathcal{H}_2$ controller. As indicated by the RGA (4.12) the HVDC-configuration is uneven with respect to the interarea modes Ω_1. The $\mathcal{H}_2$ controller therefore decouples the interarea modes fairly well as seen in Figure 4.14b. In addition to POD of the interarea mode, the controller is also tuned to attenuate oscillations in the local modes Ω_2.

[5]The original controller is 18^{th} order, the same as the open-loop system.

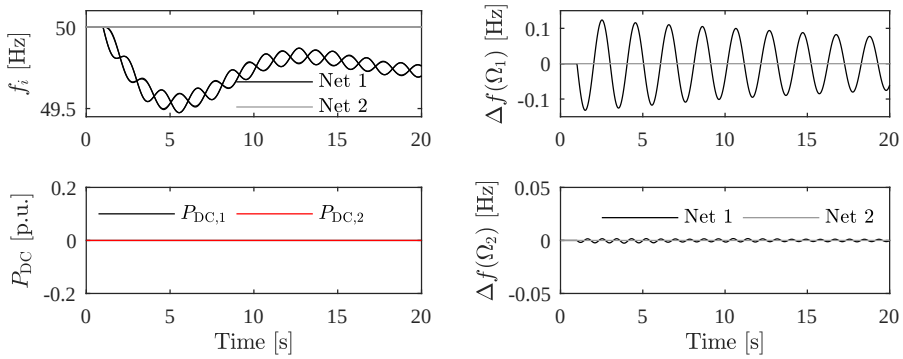

(a) Machine speeds and HVDC active power. (b) Interarea modes Ω_1 and local mode Ω_2 in the two networks.

Figure 4.12: The HVDC-interconnected system in Figure 4.9a following a 0.4 p.u. load increase at machine-bus 1 in Network 1.

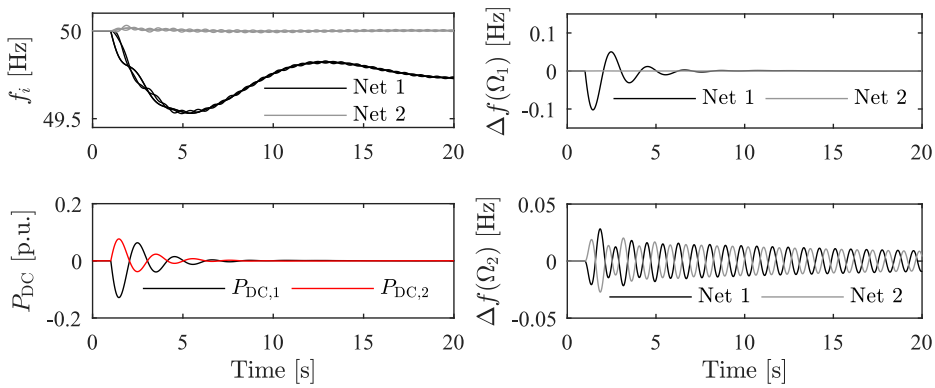

(a) Machine speeds and HVDC active power. (b) Interarea modes Ω_1 and local mode Ω_2 in the two networks.

Figure 4.13: Same scenario as in Figure 4.12 but with the decoupling POD controller (4.13) and $k = 1/5\,\mathrm{Hz}^{-1}$.

The corresponding RGA for the local modes is

$$\mathrm{RGA}(G_{\Omega_2}) = B^{\Lambda}_{\Omega_2} \times \left((B^{\Lambda}_{\Omega_2})^{-1}\right)^{T} = \begin{bmatrix} 2.9 & -1.9 \\ -1.9 & 2.9 \end{bmatrix}$$

thus the $\mathcal{H}_2$ controller does not attempt to decouple the system at the frequency of the local modes, Ω_2, as seen in Figure 4.14b.

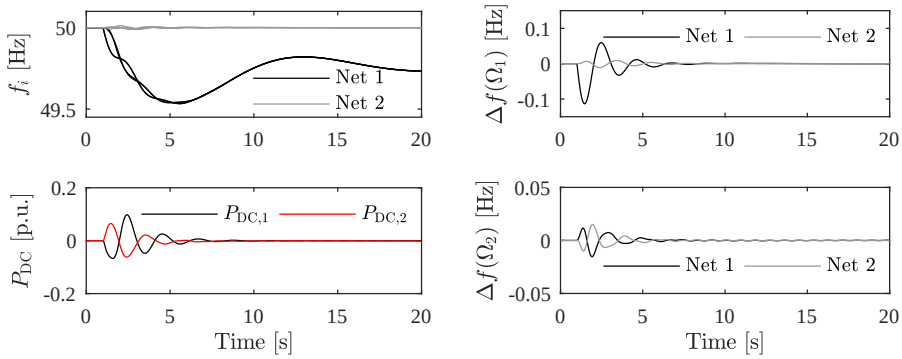

(a) Machine speeds and HVDC active power. (b) Interarea modes Ω_1 and local mode Ω_2 in the two networks.

Figure 4.14: Same scenario as in Figure 4.12 but with a $\mathcal{H}_2$ controller targeting both local and interarea modes.

4.8 Simulation Study: Two Nordic 32-Bus Networks

In this section we will analyze $N-1$ stability with respect to failure of one HVDC link while using decoupling control. We consider an artificial system made up by the interconnection of two Nordic 32-bus Cigré test systems (N32) [21] implemented in Simulink[6].

The N32 system has large power transfers from the hydro dominated north and external areas (lumped into north area) to loads in the central and southwestern areas (lumped into the south area) where a large amount of thermal power is installed. The model shows a 0.5 Hz interarea mode between the north and south areas as shown in Figure 4.15. For illustrative purposes, the damping of this mode is reduced to roughly 1% by modifying the PSS of the machines at buses 4072 and 1042. Since we want to investigate stability issues following HVDC link failure, the system needs to be controllable from a single HVDC link. This is achieved by adjusting the interarea mode of Network 2 to 0.6 Hz by scaling down system inertia.

The two N32 models are interconnected using two different HVDC-configurations, as shown in Figure 4.17. The two systems are identical with respect to relative controllability from the dc bus locations. Let V_Ω^L be the left eigenvector corresponding to the north-south interarea mode and let B be the input vector from all considered dc buses (ordered 4072, 4022, 4045, and 4063) then controllability from each input is given by

$$V_\Omega^L B = \begin{bmatrix} 1\angle 2^\circ & 0.4\angle 8^\circ & 0.4\angle -167^\circ & 0.7\angle -170^\circ \end{bmatrix}.$$

[6]The model was used in Section 3.5 to study controllability.

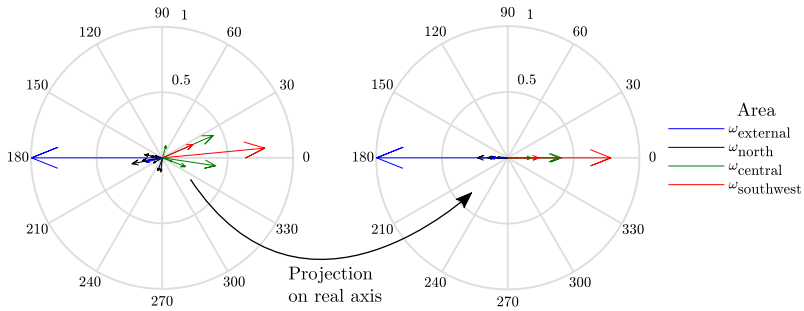

Figure 4.15: Mode shape of the north-south interarea mode in the N32 model given by left eigenvector V_Ω^L (left). Projection on the real axis, $\mathcal{V}_\Omega^L$ used for scaling output (right).

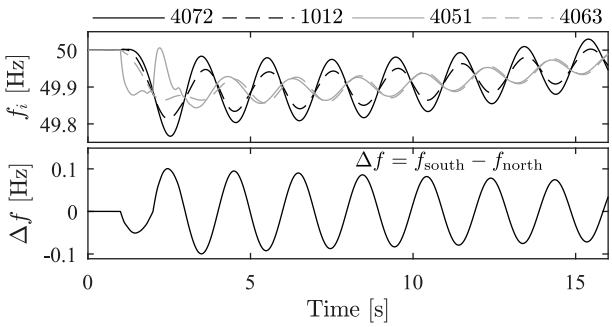

Figure 4.16: Four machine speed measurements (top) following a 500 MW load disturbance without HVDC POD control. The relative machine speed (bottom) is estimated using (4.14).

This indicates that Assumption 4.2 holds fairly well. Thus, interaction between interarea modes can be avoided using a constant pre-compensator designed according to Section 4.6.

The dynamical response following a 500 MW load disturbance (duration 1–2 s) at bus 4051 is simulated and the effect of dc link failure is investigated. The considered output signals are the relative machine speeds

$$\Delta f_i = \sum_{j=1}^{20} \mathcal{V}_{\Omega,j}^L f_{ij} \ , i \in \{1, 2\} \tag{4.14}$$

obtained by measuring generator speeds in both networks as shown in Figure 4.16.

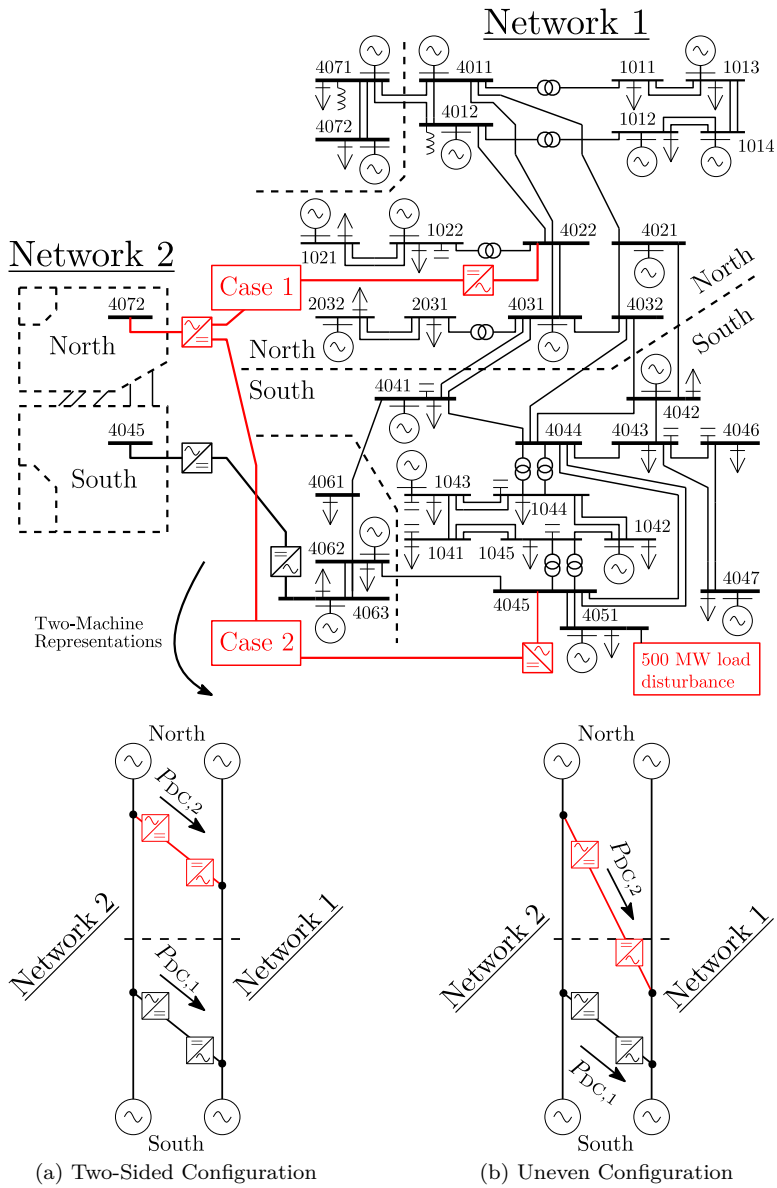

(a) Two-Sided Configuration (b) Uneven Configuration

Figure 4.17: Two HVDC-interconnected N32 networks. The frequency of the interarea mode in Network 1 and Network 2 are 0.5 Hz and 0.6 Hz respectively.

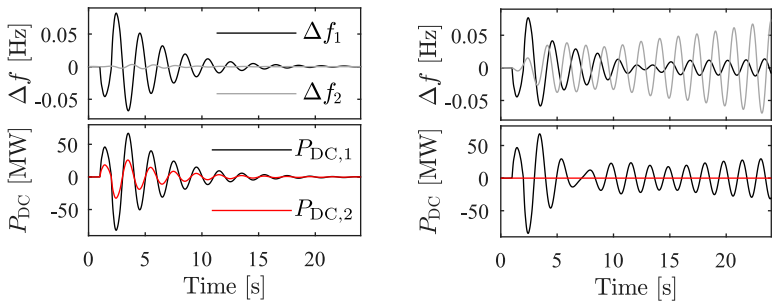

(a) Decoupling Control (b) DC Link 2 Disconnected

Figure 4.18: Case 1: Two-sided HVDC-configuration, Figure 4.17a. Relative machine speeds and HVDC power injections following a 500 MW load disturbance.

Case 1: Two-Sided HVDC-Configuration

The HVDC active power injection are given by

$$u = -k \begin{bmatrix} 1 & 0.5 \\ 0.4 & 1 \end{bmatrix} \begin{bmatrix} \Delta f_1 \\ \Delta f_2 \end{bmatrix}, \; k = 1{,}000\,\mathrm{MW\,Hz^{-1}}.$$

The dc terminals are placed on both side of the electrical mid point in each system as shown in Figure 4.17a. Similar to the one-sided configuration in Figure 4.2 this violates the $N-1$ stability criterion (4.9). Thus, disconnection of one HVDC link lead to instability as shown in Figure 4.18.

Case 2: Uneven HVDC-Configuration

The HVDC active power injection are given by

$$u = -k \begin{bmatrix} 1 & -0.6 \\ 0.4 & 1 \end{bmatrix} \begin{bmatrix} \Delta f_1 \\ \Delta f_2 \end{bmatrix}, \; k = 1{,}000\,\mathrm{MW\,Hz^{-1}}.$$

The dc terminals are placed unevenly in the two systems as shown in Figure 4.17b such that the $N-1$ stability criterion is fulfilled. Therefore, disconnection of one HVDC link does not cause instability. Additionally, the system is controllable from one HVDC link. Thus the HVDC control still stabilizes the system as seen in Figure 4.19.

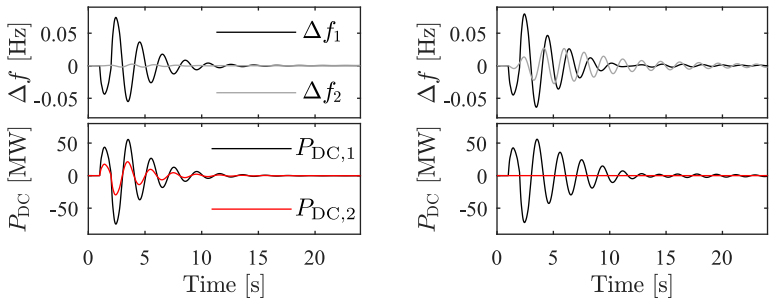

(a) Decoupling Control (b) DC Link 2 Disconnected

Figure 4.19: Case 2: Uneven HVDC-configuration, Figure 4.17b. Relative machine speeds and HVDC power injections following a 500 MW load disturbance.

4.9 Summary

Stability of oscillatory modes has become an increasing concern in the modern power system. To achieve best performance, coordinated control of multiple controllable devises may be required. In this chapter we have analyzed the suitability of different coordinated HVDC control methods with respect to network topology. The focus has been on asynchronous power systems interconnected with two HVDC lines. For certain HVDC-configurations it was shown that a decoupling control method, avoiding excitation of selected troublesome interarea modes between the two networks, is a suitable control method. For some configurations however, it was shown that decoupled control have an excessive input usage and might destabilize the system in the event of dc link failure. The decoupling control method was compared to decentralized, single-line, and centralized optimal control. It was found that the optimal $\mathcal{H}_2$ controller yielded the best combination of the previous methods for the specific HVDC-configuration.

Chapter 5

Conclusions and Future Work

In this chapter we conclude the thesis. In Section 5.1 we summarize and discuss the obtained results. Lastly in Section 5.2 we discuss future research direction in this field.

5.1 Conclusions

This thesis has studied high-voltage direct current (HVDC) control methods for improving the damping of interarea oscillations. The focus has been on asynchronous power systems interconnected by point-to-point HVDC lines. The goal has been to improve the system theoretical understanding of the fundamental difficulties and limitations imposed by network topology and dynamical interactions.

In Chapter 3 we studied the case where two asynchronous power systems was interconnected by a single HVDC line. A model abstraction where the troublesome interarea mode was represented by a two-machine network was used for the analysis. It was shown that active power modulation (depending on the electrical position of the dc terminal) is suitable for improving power oscillation damping (POD). If the dynamics of the power source can be neglected then performance, in terms of damping, is essentially only limited by the available power. However, since active power (unlike reactive power if voltage source converters are used) cannot be controlled independently at the two dc terminals, interactions between the two systems are unavoidable. These interactions have been the focus of the work.

By studying the controllability Gramian, a fundamental measure, independent of the control structure, was obtained for how hard it is to control the interarea oscillations. When considering damping improvement of both networks simultaneously, the ratio between modal frequencies was shown to set a fundamental limitation to achievable performance. With moderate feedback gains, differences in open-loop modal frequencies between the interconnected systems could be used to increase system performance in terms of POD. With too aggressive control, the interarea oscillations of the two systems will essentially be synchronized. High feedback would

allow the networks to share inertial response following disturbances which might be beneficial with regards to transient stability. However, if POD is desired, then feedback gains are limited by the modal interaction. This is because the disturbance propagates and excites the interarea mode in the neighboring system. The findings were validated on a detailed power system of two HVDC-interconnected 32-bus networks.

In Chapter 4 we consider the case with additional HVDC links. It is well known that for a system to be functionally controllable it is required that there are at least as many inputs as outputs. In other words, if we want to freely control the two outputs (i.e. the interarea mode in each network) then we need an additional controllable input. Adding control to an additional HVDC link could solve this problem. Assuming that the condition number of the resulting multi-input multi-output system is sufficiently small, individual control of the two interarea modes is achievable. It was shown that if we want to improve damping of the dominant interarea mode in each of the HVDC-interconnected networks, using two HVDC links and linear control, there are three main control structures: single-line, decentralized, and decoupled. The latter of these avoid interaction between the two modes altogether. This could be desirable if system operators in the different networks are concerned by the excitation of poorly damped modes.

Centralized optimal control was also investigated. By targeting input usage and the desired modes (given by corresponding left eigenvectors), an $\mathcal{H}_2$ optimal design proved convenient for obtaining the most suitable trade-off between the three, previously mentioned, control methods. For certain configuration of the HVDC links, decoupling control risks destabilizing the system in the event of communication or actuator failure. However, decoupling control would here require excessive input usage and is thus not $\mathcal{H}_2$ optimal. If the condition number is sufficiently small, the $\mathcal{H}_2$ design would instead opt for a controller resembling the decentralized controller.

In the study we have considered that external measurements are available from the machines involved in the interarea oscillations, giving us a nearly perfect estimation of the interarea mode to be used as a feedback signal. However, the results also extends to local measurements since an observer can be used to estimate the mode. Using the proposed $\mathcal{H}_2$ method, this is achieved without much adjustments since the designer only have to specify the available measurements in the tuning process. Additional control criteria, such as damping of additional modes can also easily be included by adding these to the performance criteria, as was done in Section 4.4.

5.2 Future Work

We conclude this thesis by providing some interesting research directions.

Incorporating Additional Dynamics

In Chapter 3 we studied limitations when proving POD with a single HVDC link under the simplifying assumption that we only considered active power control.

Reactive power was not considered since it, for POD control, is complementary to active power control [46]. Additionally, reactive power can be controlled individually at each terminal. The resulting control method would therefore be similar to having a FACTS device at each dc terminal. However, this is not completely true since both active and reactive power compete for the allowed converter current. Incorporating reactive power would relax the constraints and give a more accurate picture of the actual performance limitations. Additionally dc voltage control is assumed to be controlled sufficiently fast so that active power injections at the two terminals can be considered directly coupled. The natural extension of this work is to incorporate dc dynamics and allow for variations in the dc voltage.

Transient Stability

Throughout this thesis we have only considered small-signal stability. The main focus has been damping of oscillatory modes that can be analyzed using a linearized model. However, one of the main problems with power transmission over large geographical areas, and a reduction in system inertia, is that of transient stability. Due to the nonlinear behavior of power flow, initial control action need to be fast and strong enough to maintain system synchrony following faults. Active (and reactive) power modulation of HVDC can be used to improve this. In [12] it was shown that a controller based on local measurements may improve POD but simultaneously reduce transient stability, causing the system to go first swing unstable following certain faults. This can be attributed to the performance variable not being used as measurement [82, 83]. With external measurements these limitations can be avoided. However, the delay and reliability of wide area measurements systems (WAMS) may make a controller relying on external measurements infeasible for transient stability enhancement. Using a signal-based approach these limitations can be incorporated when designing a feedback controller based on available measurements.

Selection of External Measurements

In this theses we have considered that all machine speeds are available for feedback control. This simplifies POD control since the modes of interest can be represented as a linear combination of the speed measurements. Damping is then achievable using a proportional controller, making this control method simple and transparent. Similar results can also be achieved with feedback from a subset of the machines. However, in reducing the number of measurements, one must make sure to not destabilize previously unconsidered or unknown modes.

Consider the HVDC-interconnected system shown in Figure 5.1a. HVDC POD control is implemented to target the interarea mode, Ω_1, in each network. Based on the chosen measurements however, local mode, Ω_2, might be either stabilized or destabilized as seen in Figures 5.1b and 5.1c respectively.

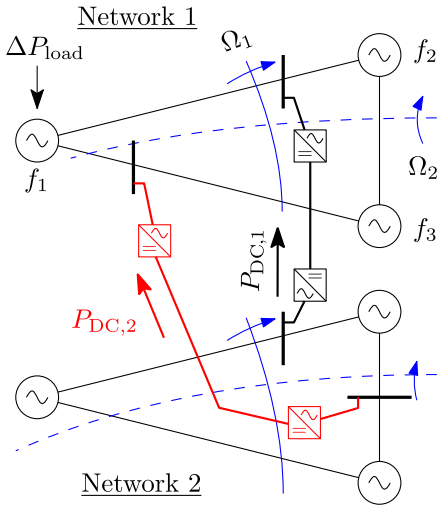

(a) Two HVDC-interconnected three-machine networks.

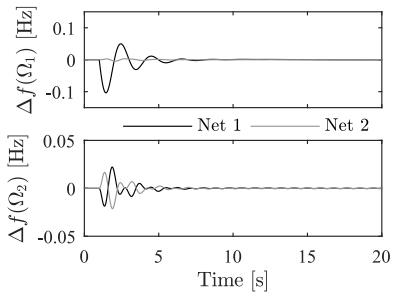

(b) Feedback signal: $y = f_1 - f_2$

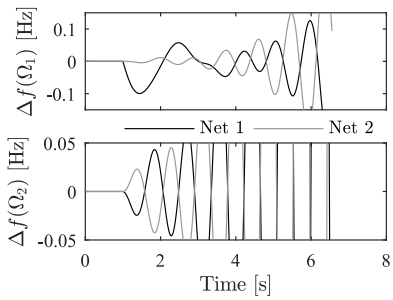

(c) Feedback signal: $y = f_1 - f_3$

Figure 5.1: System response to a 0.4 p.u. load step in Network 1 using a decoupling feedback controller as designed in Section 4.7.

As the size and complexity of the networks grow, choice of measurement signals and communication structure becomes increasingly difficult. This is a common problem process control. One method to simultaneously select measurements and optimize closed-loop performance is the sparsity promoting optimal wide area control proposed in [8, 62]. The method synthesizes a proportional multiple-input multiple-output controller to optimize a given cost function while trying to preserve sparsity in the controller. Thus, the method simultaneously design a distributed controller, measurement locations, and communication network.

If we allow for a dynamical controller, we can also use the $\mathcal{H}_2$ control design used in this thesis, or a modal linear quadratic Gaussian [18, 59], that targets modes of interest while avoiding interaction with other modes. However, with bad measurement placements this controller may be sensitive to model uncertainty, other controllers, load flow changes etc. The design method could be combined with the sparsity promoting controller using a fixed-structure control design [84, 85].

Appendix A

Appendix to Chapter 3

A.1 Eigenvalue Decomposition of a Matrix

Consider a diagonalizable matrix A (with complete basis of eigenvectors). Let

$$\Lambda = \text{diag}\{\lambda_1, \ldots, \lambda_N\}$$

where λ_n, $n \in \{1, \ldots, N\}$ are the n^{th} eigenvalue of A. Then

$$\begin{aligned} AV_R &= V_R\Lambda \\ V_L A &= \Lambda V_L \\ V_L &= V_R^{-1} \end{aligned}$$

where V_L (V_R) is the left (right) modal matrix with rows (columns) consisting of the left (right) eigenvectors V_n^L (V_n^R) of A. The factorization

$$A = V_R \Lambda V_L.$$

is useful for calculating matrix exponentials as

$$e^A = V_R\, e^{\Lambda}\, V_L = V_R\, \text{diag}\{e^{\lambda_1}, \ldots, e^{\lambda_N}\}\, V_L. \tag{A.1}$$

A.2 Solution to the State-Space Equation

Consider a N-dimensional LTI system given on state-space form

$$\dot{x}(t) = Ax(t) + Bu(t) \tag{A.2}$$

It is commonly known that the solution to (A.2) is given by

$$x(t) = e^{A(t-t_0)}x(t_0) + \int_{t_0}^{t} e^{A(t-\tau)}Bu(\tau)d\tau$$

where $x(t_0)$ is the system state at time $t = t_0$ and $u(t)$ is some external input.

A.3 State-Space Equation on Modal Form

Let ξ be a vector given by the linear transformation

$$\xi = V_L x. \tag{A.3}$$

The new variables ξ_n, $n \in \{1, \ldots, N\}$ are complex variables describing the modes of the original system. Using the transformation (A.3) on (A.2) the dynamic of the system modes are described by the state equation

$$\dot{\xi}(t) = V_L A V_R \xi(t) + V_L B u(t) = \Lambda \xi(t) + V_L B u(t). \tag{A.4}$$

Since the state matrix Λ is diagonal, system dynamics are decoupled. The solution to (A.4) are thus given by

$$\xi_n(t) = e^{\lambda_n} \xi(t_0) + \int_{t_0}^{t} e^{\lambda_n (t-\tau)} V_n^L B u(\tau) d\tau.$$

Remark A.1 The diagonal state matrix Λ makes this a practical system to analyze. However, for oscillatory modes (which appear as complex conjugated eigenvalue pairs) the resulting state variables and system matrices become complex.

A.4 Real Jordan Form

Let $\mathcal{V}_L$ be a transformation matrix with rows

- $\mathcal{V}_m^L = V_m^L$ if λ_m is real;
- $\begin{bmatrix} \mathcal{V}_n^L \\ \mathcal{V}_{n+1}^L \end{bmatrix} = 0.5 \begin{bmatrix} 1 & 1 \\ -j & j \end{bmatrix} \begin{bmatrix} V_n^L \\ \bar{V}_n^L \end{bmatrix} = \begin{bmatrix} \mathrm{Re}(V_n^L) \\ \mathrm{Im}(V_n^L) \end{bmatrix}$ if $\lambda_n, \bar{\lambda}_n$ is a complex conjugated eigenvalue pair.

With the linear transformation, $z = \mathcal{V}_L x$ the state-space representation of the system becomes

$$G_v \stackrel{s}{=} \left[\begin{array}{c|c} J & \mathcal{V}_L B \\ \hline C_v & 0 \end{array}\right] \tag{A.5}$$

where v is a set of outputs given by output matrix C_v, $J = \mathcal{V}_L A \mathcal{V}_L^{-1}$ is the block diagonal matrix[1]

$$J = \begin{bmatrix} \lambda_m & 0 & \cdots & 0 \\ 0 & \ddots & & \vdots \\ \vdots & & \begin{bmatrix} a_n & b_n \\ -b_n & a_n \end{bmatrix} & 0 \\ 0 & \cdots & 0 & \ddots \end{bmatrix} \tag{A.6}$$

[1] The modal form (4.10) is on complex Jordan form. Here we have assumed that A is diagonalizable, i.e. that all eigenvectors are linearly independent. If this is not the case, both Λ and J will have ones on the super-diagonal at positions corresponding to linearly dependent eigenvectors [73].

where complex eigenvalues $\lambda_n = -a_n \pm jb_n$.

Model Reduction in Section 3.2

Let z_i be the reduced state vector representing the observable subspace $z_i = P^\dagger x$. If the transformation matrix $P^\dagger$ is chosen as a linear combination of left eigenvectors as

$$P^\dagger = S \begin{bmatrix} \mathrm{Re}(V_n^L) \\ \mathrm{Im}(V_n^L) \end{bmatrix}$$

where S is an invertible square matrix of appropriate dimension. Then the model reduction $A_i = P^\dagger \mathcal{A}_i P$, $B_i = P^\dagger \mathcal{B}_i$ and $C_i = \mathcal{C}_i P$ results in a minimal (observable and controllable) realization of the oscillatory mode n in the original system. The new 2×2 state matrix A_i is similar (same characteristic polynomial, i.e., same eigenvalues, counting multiplicity [73]) to the corresponding 2×2 block in (A.6).

A.5 Solving the Controllability Gramian

Consider the LTI system (3.9) describing the electromechanical mode of an ac network with system state matrix and input matrix

$$A = \begin{bmatrix} 0 & 1 \\ \frac{-2V^2}{MX_\Sigma} & \frac{-D}{2M} \end{bmatrix}, \; B = \begin{bmatrix} 0 \\ \frac{X_B}{M} \end{bmatrix}. \tag{A.7}$$

For ease of notation we rewrite (A.7) as

$$A = \begin{bmatrix} 0 & 1 \\ -\Omega^2 & -2\gamma \end{bmatrix}, \; B = \begin{bmatrix} 0 \\ b \end{bmatrix}.$$

Finite-Time Controllability Gramian

The finite time controllability Gramian (Theorem 3.1) is given by

$$W_C = \int_0^T e^{At} B B^T e^{A^T t} dt \tag{3.17}$$

$\infty > T > 0$.

Calculating the Gramian for the Undamped 2×2 System

Using (A.1), W_C can be calculated as

$$W_C = \int_0^T V_L e^{\Lambda t} V_R B B^T V_R^H e^{\Lambda^H t} V_L^H dt. \tag{A.8}$$

For the 2×2 system A.5 we have

$$\begin{aligned}
\Lambda &= \begin{bmatrix} -j\Omega & 0 \\ 0 & j\Omega \end{bmatrix} \\
e^{\Lambda t} &= \begin{bmatrix} \cos(\Omega t) - j\sin(\Omega t) & 0 \\ 0 & \cos(\Omega t) + j\sin(\Omega t) \end{bmatrix} \\
V_L &= \begin{bmatrix} -j\frac{\Omega}{2} & \frac{1}{2} \\ j\frac{\Omega}{2} & \frac{1}{2} \end{bmatrix} \\
V_R &= \begin{bmatrix} j\frac{1}{\Omega} & -j\frac{1}{\Omega} \\ 1 & 1 \end{bmatrix} \\
V_R e^{\Lambda t} V_L &= \begin{bmatrix} \cos(\Omega t) & \frac{\sin(\Omega t)}{\Omega^2} \\ \frac{\sin(\Omega t)}{\Omega^2} & \cos(\Omega t) \end{bmatrix}.
\end{aligned}$$

thus the integral (A.8) becomes

$$\begin{aligned}
W_C &= b^2 \int_0^T \begin{bmatrix} \frac{\sin^2(\Omega t)}{\Omega^2} & \frac{\cos(\Omega t)\sin(\Omega t)}{\Omega} \\ \frac{\cos(\Omega t)\sin(\Omega t)}{\Omega} & \cos^2(\Omega t) \end{bmatrix} dt \\
&= b^2 \begin{bmatrix} \frac{2\Omega T - \sin(2\Omega T)}{4\Omega^3} & \frac{\sin^2(\Omega T)}{2\Omega^2} \\ \frac{\sin^2(\Omega T)}{2\Omega^2} & \frac{2T - \sin(2\Omega T)}{4\Omega} \end{bmatrix}
\end{aligned}$$

Substituting in $\Omega = \sqrt{\frac{2V^2}{MX_\Sigma}}$ and $b = \frac{X_B}{M}$ gives

$$W_C = \begin{bmatrix} w_{11} & w_{12} \\ w_{21} & w_{22} \end{bmatrix}$$

where

$$\begin{aligned}
w_{11} &= \frac{X_B^2 T}{2M}\frac{X_\Sigma}{2V^2} - \sqrt{\frac{2X_\Sigma}{MV^2}}\frac{X_B^2}{8}\frac{X_\Sigma}{2V^2}\sin\sqrt{\frac{8T^2V^2}{MX_\Sigma^2}} \\
w_{12} = w_{21} &= \frac{X_B^2 X_\Sigma}{4MV^2}\sin\sqrt{\frac{2T^2V^2}{MX_\Sigma^2}} \\
w_{22} &= \frac{X_B^2 T}{2M}\frac{1}{M} + \sqrt{\frac{2X_\Sigma}{MV^2}}\frac{X_B^2}{8}\frac{1}{M}\sin\sqrt{\frac{8T^2V^2}{MX_\Sigma^2}}.
\end{aligned}$$

For large T, this simplifies to

$$W_C \approx X_B^2 \frac{T}{2M}\begin{bmatrix} \frac{X_\Sigma}{2V^2} & 0 \\ 0 & \frac{1}{M} \end{bmatrix}$$

Calculating the Gramian for Higher Order Systems

As system dimension increases, solving the integral (3.17) analytically becomes harder. For low order systems ($N = 2$) or a numerical solution of higher order systems, the integral can conveniently be solved using matrix exponentials.

Theorem A.1 *Consider the system* (A.2). *Let*

$$\exp\left(\begin{bmatrix} -A & BB^T \\ 0 & A^T \end{bmatrix} T\right) = \begin{bmatrix} F_1(T) & G(T) \\ 0 & F_2(T) \end{bmatrix}$$

then

$$F_1(T) = e^{-AT},\ F_2(T) = e^{A^T T}$$

and

$$G(T) = \int_0^T e^{-A(T-t)} BB^T e^{A^T t} dt = e^{-AT} \int_0^T e^{At} BB^T e^{A^T t} dt.$$

Thus the finite time controllability Gramian is given by [86]

$$W_C(T) = F_2^T(T) G(T).$$

Proof: See [86, Theorem 1]

■

Infinite-Time Controllability Gramian

If A is strictly Hurwitz, then the controllability Gramian (Theorem 3.2) is given by the unique solution to the Lyapunov equation

$$AW_C + W_C A^T + BB^T = 0. \tag{3.18}$$

Calculating the Gramian for the 2×2 System

For the 2×2 system A.5 we have

$$\begin{bmatrix} 0 & 1 \\ -\Omega^2 & -2\gamma \end{bmatrix} W_C + W_C \begin{bmatrix} 0 & -\Omega_2 \\ 1 & -2\gamma \end{bmatrix} + \begin{bmatrix} 0 & 0 \\ 0 & b^2 \end{bmatrix} = 0$$

with

$$W_C = W_C^T = \begin{bmatrix} w_{11} & w_{12} \\ w_{12} & w_{22} \end{bmatrix}$$

the controllability Gramian obtained by solving the equations

$$\begin{aligned} w_{12} + w_{12} &= 0 \\ w_{22} - \Omega^2 w_{11} &= 0 \\ w_{11} &= \frac{w_{22}}{\Omega^2} \\ -2\gamma w_{22} - 2\gamma w_{22} + b^2 &= 0 \\ w_{22} &= \frac{b_2^2}{4\gamma} \end{aligned}$$

Substituting in $\Omega = \sqrt{\frac{2V^2}{MX_\Sigma}}$, $\gamma = \frac{D}{4M}$, and $b = \frac{X_B}{M}$ gives

$$W_C = \frac{X_B}{D} \begin{bmatrix} \frac{X_\Sigma}{2V^2} & 0 \\ 0 & \frac{1}{M} \end{bmatrix}.$$

Calculating the Gramian for Higher Order Systems

The Lyapunov equation (3.18) can be solved using Kroneckers products [75]

$$(A \otimes I + I \otimes A^T)\boldsymbol{w}_c = -\boldsymbol{b}$$

where

- I is a identity matrix with the same dimensions as A;
- $\boldsymbol{b}$ is a column vector with the rows of BB^T stacked on top of each other;
- $\boldsymbol{w}_c$ is a column vector to be solved with the columns of W_C stacked on top of each other.

A.6 Damping Constant in Examples 3.1 and 3.2

The complex conjugated eigenvalue pair of A_1 in (3.11) is given by

$$\lambda = \gamma \pm \omega_e = -\frac{D}{4M} \pm \sqrt{\left(\frac{D}{4M}\right)^2 - \frac{2}{M}}. \tag{A.9}$$

The damping ratio is defined as

$$\zeta_1 := \frac{-\mathrm{Re}(\lambda)}{|\lambda|} = \frac{-\gamma}{\sqrt{\gamma^2 + \omega_e^2}}$$

and thus

$$|\gamma| = \omega_e \sqrt{\frac{\zeta_1^2}{1-\zeta_1^2}} \approx \Omega_1 \sqrt{\frac{\zeta_1^2}{1-\zeta_1^2}}.$$

where we have assumed that the mode is poorly damped. Using (A.9) the damping constant is then given by

$$D \approx 4M\Omega_1 \sqrt{\frac{\zeta_1^2}{1-\zeta_1^2}} = \frac{8}{\Omega_1} \sqrt{\frac{\zeta_1^2}{1-\zeta_1^2}} \approx 8\frac{\zeta_1}{\Omega_1}$$

A.7 Maclaurin Series Expansion for Small $|\epsilon|$

The Maclaurin series expansion of (3.23) becomes

$$\begin{aligned}
a &= \frac{X_B^2}{D}\frac{X_\Sigma}{2V^2} \\
\alpha &= a\left(1 - \frac{c}{M}\epsilon^2\right) + \mathcal{O}(\epsilon^3) \\
b &= \frac{X_B^2}{D}\frac{1}{M} \\
b_2 &= b\left(1 - \frac{\epsilon}{M} + \frac{\epsilon^2}{M^2}\right) + \mathcal{O}(\epsilon^3) \\
\beta &= b\frac{1}{4M^2}\left(4M^2 - 2M\epsilon + (1-4cM)\epsilon^2\right) + \mathcal{O}(\epsilon^3) \\
\gamma &= \frac{X_B^2}{D^2}\left(\frac{\epsilon}{M} - \frac{\epsilon^2}{2M^2}\right) + \mathcal{O}(\epsilon^3).
\end{aligned}$$

Taking derivatives with respect to ϵ

$$\begin{aligned}
\frac{d\alpha(\epsilon)}{d\epsilon} &= 0 + \mathcal{O}(\epsilon^2) \\
\frac{db_2(\epsilon)}{d\epsilon} &= -\frac{b}{M}\epsilon + \mathcal{O}(\epsilon^2) \\
\frac{d\beta(\epsilon)}{d\epsilon} &= -\frac{b}{2M}\epsilon + \mathcal{O}(\epsilon^2) \\
\frac{d\gamma(\epsilon)}{d\epsilon} &= \frac{b}{D}\epsilon + \mathcal{O}(\epsilon^2).
\end{aligned}$$

For the weakly damped system in Example 3.2, $M \gg D$, and therefore

$$\left|\frac{d\alpha(\epsilon)}{d\epsilon}\right| \leq \left|\frac{d\beta(\epsilon)}{d\epsilon}\right| \leq \left|\frac{db_2(\epsilon)}{d\epsilon}\right| \leq \left|\frac{d\gamma(\epsilon)}{d\epsilon}\right|.$$

A.8 Improved Control Effort Estimate

The control effort estimate (3.34) holds for any network parameterizations. Defining

$$\rho := 2\sqrt{\frac{V_1^2 M_1}{X_{\Sigma,1}} \frac{V_2^2 M_2}{X_{\Sigma,2}}}$$

$$\Psi_1 := 1 + D^2 \frac{1 + \Omega_1^2/\Omega_2^2}{\rho(1 - \Omega_1^2/\Omega_2^2)^2}$$

$$\Psi_2 := 1 + D^2 \frac{1 + \Omega_2^2/\Omega_1^2}{\rho(1 - \Omega_2^2/\Omega_1^2)^2}$$

gives the estimate

$$\|u\|_2^2 \approx E_\infty^2(D) := E_0 \frac{D}{X_B^2} \sqrt{\Psi_1 \Psi_2}$$

which is more accurate for parameter differences between the HVDC-interconnected networks.

Appendix B

Appendix to Chapter 4

B.1 Internal Stability

A system is internally stable if all the four closed-loop transfer functions in Figure B.1,

$$\begin{aligned} u &= (I - KG)^{-1}d_u + K(I - GK)^{-1}d_y \\ y &= G(I - KG)^{-1}d_u + (I - GK)^{-1}d_y, \end{aligned} \tag{B.1}$$

from external input disturbances d_u and output disturbances d_y, are stable. Since G and K ((4.2) and (4.8) respectively) contains no right-half-plane poles it is sufficient to show that one of the transfer functions in (B.1) are stable [87]. If we assume failure of HVDC link 2, then internal stability can be assessed by picking the single-input single-output internal sensitivity function from d_{u1} to u_1

$$S_{I1} = \frac{(s^2 + \Omega_1^2)(s^2 + \Omega_2^2)}{p(s)}.$$

Internal stability can then be assessed from the pole polynomial

$$p(s) \;=\; s^4 + s^3(b_1 + b_2) + s^2(\Omega_1^2 + \Omega_2^2) + s(b_1\Omega_2^2 + b_2\Omega_1^2) + \Omega_1^2\Omega_2^2. \tag{B.2}$$

where w_{11} and w_{12} are constant elements from the top row of the decoupling precompensator (4.7), and

$$b_1 := kb_{11}w_{11}, \quad b_2 := \mathrm{sgn}(b_{22})kb_{21}w_{12}. \tag{B.3}$$

Routh's algorithm provide a necessary and sufficient condition for stability of the system [88]. For the pole polynomial (B.2) to have negative-real-part roots its

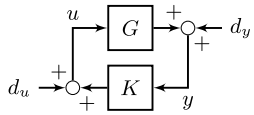

Figure B.1: Closed loop system used to study internal stability.

required that

$$\begin{aligned} 1 &> 0 \\ b_1 + b_2 &> 0 \qquad \text{(B.4)} \\ \frac{b_1\Omega_1^2 + b_2\Omega_2^2}{b_1 + b_2} &> 0 \qquad \text{(B.5)} \\ \frac{b_1 b_2(\Omega_1^2 - \Omega_2^2)^2}{b_1\Omega_1^2 + b_2\Omega_2^2} &> 0 \qquad \text{(B.6)} \\ \Omega_1^2\Omega_2^2 &> 0. \end{aligned}$$

With (4.7) and (B.3) stability condition (B.4) becomes

$$b_1 + b_2 = kb_{11} - \text{sgn}(b_{22})kb_{21}\frac{b_{12}}{b_{11}} > 0 \qquad \text{(B.7)}$$

thus the condition simplifies to $b_{11}^2 > \text{sgn}(b_{22})b_{21}b_{12}$. Similarly, condition (B.5) boils down to

$$b_{11}^2 > \text{sgn}(b_{22})\frac{\Omega_2^2}{\Omega_1^2}b_{21}b_{12}. \qquad \text{(B.8)}$$

If (B.7), and thus (B.8) holds then the pole polynomial (B.2) have negative-real-part roots if (from (B.6))

$$b_1 b_2 = k^2 b_{11}\left(-\text{sgn}(b_{22})b_{21}\frac{b_{12}}{b_{11}}\right) > 0.$$

This gives the $N-1$ stability criterion

$$-\text{sgn}(b_{22})b_{21}b_{12} > 0,\ \text{sgn}(b_{11}) \text{ and } \text{sgn}(k) := 1. \qquad \text{(4.9)}$$

If $\Omega_1 = \Omega_2$, b_{12}, or b_{21} the system is not controllable and thus cannot be stabilized nor destabilized by the remaining HVDC link.

B.2 Closed-Loop System on Real Jordan Form

Consider the system (A.5)–(A.6) given on real Jordan form. Assume that the measurement

$$y_n = \begin{bmatrix} z_n \\ \bar{z}_n \end{bmatrix} = \begin{bmatrix} \text{Re}(V_n^L) \\ \text{Im}(V_n^L) \end{bmatrix} x$$

is available for feedback. The closed loop system then becomes

$$\dot{z} = Jz + \mathcal{V}_L BK \begin{bmatrix} z_n \\ \bar{z}_n \end{bmatrix} = \begin{bmatrix} \lambda_m & 0 & & & \vdots & 0 \\ 0 & \ddots & & & \vdots & \vdots \\ \vdots & & \begin{bmatrix} a_n & b_n \\ -b_n & a_n \end{bmatrix} & & + \mathcal{V}_L BK & 0 \\ & & & & & \\ 0 & 0 & & & \vdots & \ddots \end{bmatrix} z$$

where K is some controller.

Complex eigenvalues are given by $\lambda_n = a_n \pm jb_n$. Since $b_n \neq 0$, λ_n (and its conjugate $\bar{\lambda}_n$) can be controlled with any of state variables in the pair $z_n, \bar{z}_n$ as long as either $\mathrm{Re}(V_n^L)B$ or $\mathrm{Im}(V_n^L)B \neq 0$.

Bibliography

[1] A. Nyman, K. Jaaskelainen, M. Vaitomaa, B. Jansson, and K. G. Danielsson, "The Fenno-Skan HVDC link commissioning," *IEEE Transactions on Power Delivery*, vol. 9, no. 1, pp. 1–9, Jan. 1994.

[2] K. Uhlen, L. Vanfretti, M. M. de Oliveira, A. B. Leirbukt, V. H. Aarstrand, and J. O. Gjerde, "Wide-area power oscillation damper implementation and testing in the Norwegian transmission network," in *IEEE Power and Energy Society General Meeting*, San Diego, CA, Jul. 2012, pp. 1–7.

[3] P. Kundur, J. Paserba, V. Ajjarapu, G. Andersson, A. Bose, C. Canizares, N. Hatziargyriou, D. Hill, A. Stankovic, C. Taylor, T. V. Cutsem, and V. Vittal, "Definition and classification of power system stability IEEE/CIGRE joint task force on stability terms and definitions," *IEEE Transactions on Power Systems*, vol. 19, no. 3, pp. 1387–1401, May 2004.

[4] M. A. Elizondo, R. Fan, H. Kirkham, M. Ghosal, F. Wilches-Bernal, D. A. Schoenwald, and J. Lian, "Interarea oscillation damping control using high voltage dc transmission: A survey," *IEEE Transactions on Power Systems*, vol. 33, no. 6, pp. 6915–6923, Nov. 2018.

[5] A. Mešanović, U. Münz, and C. Heyde, "Comparison of H∞, H2, and pole optimization for power system oscillation damping with remote renewable generation," *IFAC-PapersOnLine*, vol. 49, no. 27, pp. 103–108, Oct. 2016.

[6] Y. Pipelzadeh, B. Chaudhuri, and T. C. Green, "Control coordination within a VSC HVDC link for power oscillation damping: A robust decentralized approach using homotopy," *IEEE Transactions on Control Systems Technology*, vol. 21, no. 4, pp. 1270–1279, Jul. 2013.

[7] R. Preece, J. V. Milanović, A. M. Almutairi, and O. Marjanovic, "Damping of inter-area oscillations in mixed AC/DC networks using WAMS based supplementary controller," *IEEE Transactions on Power Systems*, vol. 28, no. 2, pp. 1160–1169, May 2013.

[8] F. Dörfler, M. R. Jovanović, M. Chertkov, and F. Bullo, "Sparsity-promoting optimal wide-area control of power networks," *IEEE Transactions on Power Systems*, vol. 29, no. 5, pp. 2281–2291, Sep. 2014.

[9] S. P. Azad, J. A. Taylor, and R. Iravani, "Decentralized supplementary control of multiple LCC-HVDC links," *IEEE Transactions on Power Systems*, vol. 31, no. 1, pp. 572–580, Jan. 2016.

[10] R. L. Cresap and W. A. Mittelstadt, "Small-signal modulation of the Pacific HVDC intertie," *IEEE Transactions on Power Apparatus and Systems*, vol. 95, no. 2, pp. 536–541, Mar. 1976.

[11] R. L. Cresap, W. A. Mittelstadt, D. N. Scott, and C. W. Taylor, "Operating experience with modulation of the Pacific HVDC Intertie," *IEEE Transactions on Power Apparatus and Systems*, vol. PAS-97, no. 4, pp. 1053–1059, Jul. 1978.

[12] D. Trudnowski, D. Kosterev, and J. Undrill, "PDCI damping control analysis for the western North American power system," in *IEEE Power Energy Society General Meeting*, Vancouver, Canada, Jul. 2013, pp. 1–5.

[13] P. Pourbeik, P. S. Kundur, and C. W. Taylor, "The anatomy of a power grid blackout - Root causes and dynamics of recent major blackouts," *IEEE Power and Energy Magazine*, vol. 4, no. 5, pp. 22–29, Sep. 2006.

[14] D. N. Kosterev, C. W. Taylor, and W. A. Mittelstadt, "Model validation for the August 10, 1996 WSCC system outage," *IEEE Transactions on Power Systems*, vol. 14, no. 3, pp. 967–979, Aug. 1999.

[15] P. Kundur, *Power System Stability and Control*. New York: McGraw-Hill, 1994.

[16] I. Kamwa, "Performance of three PSS for interarea oscillations - MATLAB & Simulink," 1999, [Online] Available: https://mathworks.com/help/physmod/sps/examples/performance-of-three-pss-for-interarea-oscillations.html, Accessed: 2019-03-05.

[17] R. Wachal, A. Jindal, S. Dennetière, H. Saad, O. Rui, S. Cole, M. Barnes, L. Zhang, Z. Song, J. Jardini, J. C. Garcia, F. Mosallat, H. Suriyaarachich, P. Le-Huy, A. Totterdell, L. Zeni, S. Kodsi, T. Deepak, P. Thepparat, T. Beddard, J. Velasquez, S. D'Arco, A. Morales, Y. Kono, T. K. Vrana, and Y. Yang, "Guide for the development of models for HVDC converters in a HVDC grid," CIGRE, Tech. Rep., Dec. 2014.

[18] R. Preece, "A probabilistic approach to improving the stability of meshed power networks with embedded HVDC lines," Ph.D. dissertation, University of Manchester, Manchester, U.K., 2013.

[19] E. Björk, "Load characteristic influence on power oscillation damping : Case study on HVDC-interconnected AC-grids," Master's Thesis, KTH Royal Institute of Technology, Stockholm, Sweden, 2018.

[20] L. Harnefors, N. Johansson, and L. Zhang, "Impact on interarea modes of fast HVDC primary frequency control," *IEEE Transactions on Power Systems*, vol. 32, no. 2, pp. 1350–1358, Mar. 2017.

[21] M. Stubbe, "Long term dynamics phase II final report," CIGRE, Tech. Rep. Task Force 38.08.08, Mar. 1995.

[22] J. Björk, K. H. Johansson, and L. Harnefors, "Fundamental performance limitations in utilizing HVDC to damp interarea modes," *IEEE Transactions on Power Systems*, vol. 34, no. 2, pp. 1095–1104, Mar. 2019.

[23] J. Björk, K. H. Johansson, L. Harnefors, and R. Eriksson, "Analysis of coordinated HVDC control for power oscillation damping," in *IEEE eGrid*, Charleston, SC, Nov. 2018, pp. 1–6, best paper award recieved for e-poster presentation.

[24] ENTSO-E, "Supporting document for the network code on electricity balancing," Tech. Rep., 2014.

[25] ——, "Frequency stability evaluation criteria for the synchronous zone of continental europe," Tech. Rep., 2016.

[26] A. T. Gullberg, D. Ohlhorst, and M. Schreurs, "Towards a low carbon energy future – Renewable energy cooperation between Germany and Norway," *Renewable Energy*, vol. 68, pp. 216–222, Aug. 2014.

[27] T. V. Cutsem and C. Vournas, *Voltage Stability of Electric Power Systems*. Boston, MA: Springer US, 1998.

[28] M. Pavella, D. Ernst, and D. Ruiz-Vega, *Transient Stability of Power Systems: A Unified Approach to Assessment and Control*. Kluwer Academic Publishers, 2000.

[29] D. Mondal, A. Chakrabarti, and A. Sengupta, *Power System Small Signal Stability Analysis and Control*. Elsevier Science, 2014.

[30] K. Uhlen, L. Warland, J. O. Gjerde, O. Breidablik, M. Uusitalo, A. B. Leirbukt, and P. Korba, "Monitoring amplitude, frequency and damping of power system oscillations with PMU measurements," in *IEEE Power and Energy Society General Meeting - Conversion and Delivery of Electrical Energy in the 21st Century*, Pittsburgh, PA, Jul. 2008, pp. 1–7.

[31] ENTSO-E, "Analysis of CE inter-area oscillations of 1st December 2016," SG SPD Report, Jul. 2017.

[32] ——, "Oscillation event 03.12.2017: System protection and dynamics WG," Tech. Rep., Mar. 2018.

[33] J. Arrillaga, *High Voltage Direct Current Transmission*, 2nd ed. London, United Kingdom: The Institution of Engineering and Technology, 2008.

[34] A. Ekström, *High Power Eelectronic HVDC and SVC*. Stockholm, Sweden: KTH Royal Institute of Technology, Jun. 1990.

[35] L. Zhang, L. Harnefors, and H. P. Nee, "Interconnection of two very weak AC Systems by VSC-HVDC Links Using Power-Synchronization Control," *IEEE Transactions on Power Systems*, vol. 26, no. 1, pp. 344–355, Feb. 2011.

[36] K. Sharifabadi, L. Harnefors, H.-P. Nee, S. Norrga, and R. Teodorescu, *Design, Control and Application of Modular Multilevel Converters for HVDC Transmission Systems*. Chichester, UK: John Wiley & Sons, Ltd, Oct. 2016.

[37] R. Eriksson, "A new control structure for multiterminal dc grids to damp interarea oscillations," *IEEE Transactions on Power Delivery*, vol. 31, no. 3, pp. 990–998, Jun. 2016.

[38] Y. Li, Z. Xu, J. Østergaard, and D. J. Hill, "Coordinated control strategies for offshore wind farm integration via VSC-HVDC for system frequency support," *IEEE Transactions on Energy Conversion*, vol. 32, no. 3, pp. 843–856, Sep. 2017.

[39] W. Du, Q. Fu, and H. Wang, "Strong dynamic interactions between multi-terminal dc network and ac power systems caused by open-loop modal coupling," *IET Generation, Transmission & Distribution*, vol. 11, no. 9, pp. 2362–2374, Jun. 2017.

[40] M. Andreasson, R. Wiget, D. V. Dimarogonas, K. H. Johansson, and G. Andersson, "Distributed frequency control through MTDC transmission systems," *IEEE Transactions on Power Systems*, vol. 32, no. 1, pp. 250–260, Jan. 2017.

[41] H. Rao, "Architecture of Nan'ao multi-terminal VSC-HVDC system and its multi-functional control," *CSEE Journal of Power and Energy Systems*, vol. 1, no. 1, pp. 9–18, Mar. 2015.

[42] G. Tang, Z. He, H. Pang, X. Huang, and X. p Zhang, "Basic topology and key devices of the five-terminal dc grid," *CSEE Journal of Power and Energy Systems*, vol. 1, no. 2, pp. 22–35, Jun. 2015.

[43] M. Callavik, M. Larsson, and S. Stoeter, "Powering the world," *ABB review special report: 60 years of HVDC*, pp. 6–11, Aug. 2014.

[44] M. Barnes, D. V. Hertem, S. P. Teeuwsen, and M. Callavik, "HVDC systems in smart grids," *Proceedings of the IEEE*, vol. 105, no. 11, pp. 2082–2098, Nov. 2017.

[45] "IEEE guide for control architecture for high power electronics (1 MW and greater) used in electric power transmission and distribution systems," pp. 1–47, Feb. 2011.

[46] T. Smed and G. Andersson, "Utilizing HVDC to damp power oscillations," *IEEE Transactions on Power Delivery*, vol. 8, no. 2, pp. 620–627, Apr. 1993.

[47] Y. Cao, W. Wang, Y. Li, Y. Tan, C. Chen, L. He, U. Häger, and C. Rehtanz, "A virtual synchronous generator control strategy for VSC-MTDC system," *IEEE Transactions on Energy Conversion*, vol. 33, no. 2, pp. 750–761, 2017.

[48] S. P. Teeuwsen, G. Love, and R. Sherry, "1400 MW New Zealand HVDC upgrade: Introducing power modulation controls and round power mode," in *IEEE Power Energy Society General Meeting*, Vancouver, Canada, Jul. 2013, pp. 1–5.

[49] C. W. Taylor and S. Lefebvre, "HVDC controls for system dynamic performance," *IEEE Transactions on Power Systems*, vol. 6, no. 2, pp. 743–752, May 1991.

[50] M. Guan, J. Cheng, C. Wang, Q. Hao, W. Pan, J. Zhang, and X. Zheng, "The frequency regulation scheme of interconnected grids with VSC-HVDC links," *IEEE Transactions on Power Systems*, vol. 32, no. 2, pp. 864–872, Mar. 2017.

[51] M. A. Elizondo, N. Mohan, J. O'Brien, Q. Huang, D. Orser, W. Hess, H. Brown, W. Zhu, D. Chandrashekhara, Y. V. Makarov, D. Osborn, J. Feltes, H. Kirkham, D. Duebner, and Z. Huang, "HVDC macrogrid modeling for power-flow and transient stability studies in north american continental-level interconnections," *CSEE Journal of Power and Energy Systems*, vol. 3, no. 4, pp. 390–398, Dec. 2017.

[52] ENTSO-E, "Transmission system map," 2017, [Online] Available: https://www.entsoe.eu/data/map/, Accessed: 2019-03-05.

[53] Statnett, Fingrid, Energinet.dk, and S. Kraftnät, "Challenges and opportunities for the Nordic power system," Tech. Rep., 2016.

[54] I. Graabak, S. Jaehnert, M. Korpås, and B. Mo, "Norway as a battery for the future european power system—Impacts on the hydropower system," *Energies*, vol. 10, no. 12, pp. 1–25, Dec. 2017.

[55] C. E. Grund, R. V. Pohl, and J. Reeve, "Control design of an active and reactive power HVDC modulation system with Kalman filtering," *IEEE Power Engineering Review*, vol. PER-2, no. 10, pp. 61–61, Oct. 1982.

[56] S. G. Johansson, G. Asplund, E. Jansson, and R. Rudervall, "Power system stability benefits with VSC dc transmission systems," in *CIGRE Session*, Paris, France, Aug. 2004, pp. 1–8.

[57] W. Li, "PMU-based state estimation for hybrid ac and dc grids," Ph.D. dissertation, KTH Royal Institute of Technology, Stockholm, Sweden, 2018.

[58] R. Preece, J. V. Milanovic, A. M. Almutairi, and O. Marjanovic, "Probabilistic evaluation of damping controller in networks with multiple VSC-HVDC lines," *IEEE Transactions on Power Systems*, vol. 28, no. 1, pp. 367–376, Feb. 2013.

[59] A. Almutairi, "Enhancement of power system stability using wide area measurement system based damping controller," Ph.D. dissertation, University of Manchester, Manchester, U.K., 2010.

[60] M. Hadjikypris, O. Marjanovic, and V. Terzija, "Damping of inter-area power oscillations in hybrid AC-DC power systems based on supervisory control scheme utilizing FACTS and HVDC," in *Power Systems Computation Conference*. Genoa, Italy: IEEE, Jun. 2016, pp. 1–7.

[61] W. Juanjuan, F. Chuang, and Z. Yao, "Design of WAMS-based multiple HVDC damping control system," *IEEE Transactions on Smart Grid*, vol. 2, no. 2, pp. 363–374, Jun. 2011.

[62] X. Wu and M. R. Jovanović, "Sparsity-promoting optimal control of consensus and synchronization networks," in *IEEE American Control Conference*, Portland, OR, Jun. 2014, pp. 2936–2941.

[63] A. Fuchs and M. Morari, "Placement of HVDC links for power grid stabilization during transients," in *IEEE PowerTech*, Grenoble, France, 2013, pp. 1–6.

[64] M. Ndreko, A. vad der Meer, M. Gibescu, B. G. Rawn, and M. A. M. M. vad der Meijden, "Damping power system oscillations by VSC-based HVDC networks: A North Sea grid case study," in *12th Wind Integration Workshop*, London, U.K., 2013, pp. 1–6.

[65] W. Wang, Y. Li, Y. Cao, U. Häger, and C. Rehtanz, "Adaptive droop control of VSC-MTDC system for frequency support and power sharing," *IEEE Transactions on Power Systems*, vol. 33, no. 2, pp. 1264–1274, Mar. 2018.

[66] D. Van Hertem, R. Eriksson, L. Söder, and M. Ghandhari, "Coordination of multiple power flow controlling devices in transmission systems," in *9th IET International Conference on AC and DC Power Transmission*, London, UK, Oct. 2010, pp. 1–6.

[67] L. Harnefors, N. Johansson, L. Zhang, and B. Berggren, "Interarea oscillation damping using active-power modulation of multiterminal HVDC transmissions," *IEEE Transactions on Power Systems*, vol. 29, no. 5, pp. 2529–2538, Sep. 2014.

[68] A. C. Antoulas, *Approximation of Large-Scale Dynamical Systems*. Siam, 2005.

[69] W. J. Rugh, *Linear System Theory*, 2nd ed. Upper Saddle River, N.J: Pearson, 1995.

[70] C.-T. Chen, *Linear System Theory and Design*, 3rd ed., ser. Oxford Series in Electrical and Computer Engineering. New York: Oxford University Press, 1999.

[71] C. Nordling, *Physics Handbook for Science and Engineering*, 8th ed. Lund, Sweden: Studentlitteratur, 2006.

[72] A. Monticelli, *Power System Oscillations*. Boston: Kluwer Academic Publishers, 1999.

[73] R. A. Horn and C. R. Johnsson, *Matrix Analysis*. Cambridge, UK: Cambridge University Press, 1985.

[74] V. Klema and A. Laub, "The singular value decomposition: Its computation and some applications," *IEEE Transactions on Automatic Control*, vol. 25, no. 2, pp. 164–176, Apr. 1980.

[75] D. Xue and Y. Chen, *Solving Applied Mathematical Problems with MATLAB*, 1st ed. Boca Raton: Chapman and Hall/CRC, 2008.

[76] S. Skogestad and I. Postlethwaite, *Multivariable Feedback Control: Analysis and Design*, 2nd ed. Chichester, England: Wiley, 2005.

[77] N. Chaudhuri, A. Domahidi, R. Majumder, B. Chaudhuri, P. Korba, S. Ray, and K. Uhlen, "Wide-area power oscillation damping control in Nordic equivalent system," *IET Generation, Transmission & Distribution*, vol. 4, no. 10, pp. 1139–1150, 2010.

[78] D. Ruiz-Vega and M. Pavella, "A comprehensive approach to transient stability control. I-II," *IEEE Transactions on Power Systems*, vol. 18, no. 4, pp. 1446–1460, Nov. 2003.

[79] F. Dörfler and F. Bullo, "Kron reduction of graphs with applications to electrical networks," *IEEE Transactions on Circuits and Systems I: Regular Papers*, vol. 60, no. 1, pp. 150–163, Jan. 2013.

[80] F. Milano and A. Ortega, "Frequency divider," *IEEE Transactions on Power Systems*, vol. 32, no. 2, pp. 1493–1501, Mar. 2017.

[81] J. Zhang, C. Y. Chung, and Y. Han, "A novel modal decomposition control and its application to PSS design for damping interarea oscillations in power systems," *IEEE Transactions on Power Systems*, vol. 27, no. 4, pp. 2015–2025, Nov. 2012.

[82] J. S. Freudenberg, C. V. Hollot, R. H. Middleton, and V. Toochinda, "Fundamental design limitations of the general control configuration," *IEEE Transactions on Automatic Control*, vol. 48, no. 8, pp. 1355–1370, Aug. 2003.

[83] J. L. Domínguez-García, F. D. Bianchi, and O. Gomis-Bellmunt, "Control signal selection for damping oscillations with wind power plants based on fundamental limitations," *IEEE Transactions on Power Systems*, vol. 28, no. 4, pp. 4274–4281, Nov. 2013.

[84] P. Apkarian, "Tuning controllers against multiple design requirements," in *IEEE 16th International Conference on System Theory, Control and Computing*, Sinaia, Romania, Oct. 2012, pp. 1–6.

[85] P. Gahinet and P. Apkarian, "Structured H∞ Synthesis in MATLAB," *IFAC Proceedings Volumes*, vol. 44, no. 1, pp. 1435–1440, Jan. 2011.

[86] C. V. Loan, "Computing integrals involving the matrix exponential," *IEEE Transactions on Automatic Control*, vol. 23, no. 3, pp. 395–404, Jun. 1978.

[87] K. Zhou, *Robust and Optimal Control*. Englewood Cliffs, NJ: Prentice Hall, 1996.

[88] T. Glad and L. Ljung, *Reglerteknik: Grundläggande teori*, 4th ed. Lund, Sweden: Studentlitteratur, 2006.